Boiling turbulent Rayleigh-Bénard convection

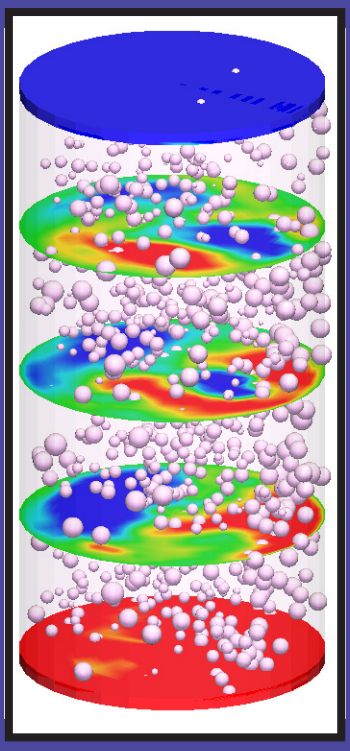

Rajaram Lakkaraju

Boiling Turbulent Rayleigh-Bénard Convection

Rajaram Lakkaraju

Samenstelling promotiecommissie:

Prof. dr. G. van der Steenhoven (voorzitter)	University of Twente
Prof. dr. D. Lohse (promotor)	University of Twente
Prof. dr. A. Prosperetti (promotor)	University of Twente & Johns Hopkins University
Dr. C. Sun	University of Twente
Prof. dr. M. Alam	Jawaharlal Nehru Centre for Advanced Scientific Research
Dr. R. Hagmeijer	University of Twente
Prof. dr. J. A. M. Kuipers	Eindhoven University of Technology
Prof. dr. R. Verzicco	University of Twente & University of Rome "Tor Vergata"

This work was carried out at the Physics of Fluids group, TNW, Mesa$^+$ Institutes of the University of Twente. It is part of the research program on Fundamentals of Heterogeneous Bubbly Flows funded by Foundation for Fundamental Research on Matter (FOM), AkzoNobel, DSM, Shell and Tata Steel. FOM is autonomous division and part of Netherlands Organization for Scientific Research (NWO).

Nederlandse titel:
Kokende turbulent Rayleigh-Bénard convectie

Publisher:
Rajaram Lakkaraju, Physics of Fluids, University of Twente,
P.O. Box 217, 7500 AE Enschede, The Netherlands.

Cover Illustration: Boiling of water at 100 ^{o}C at 1 atm. pressure in a cylinder heated at bottom and cooled at top with a 0.25 K temperature difference. Instantaneous position of bubbles, and vertical velocity contours (red for up and blue for down moving liquid) are shown.

ISBN: 978-90-365-3488-8

BOILING TURBULENT RAYLEIGH-BÉNARD CONVECTION

PROEFSCHRIFT

ter verkrijging van
de graad van doctor aan de Universiteit Twente,
op gezag van de rector magnificus,
Prof. dr. H. Brinksma,
volgens besluit van het College voor Promoties
in het openbaar te verdedigen
op vrijdag 11 januari 2013 om 16.45 uur

door

Rajaram Lakkaraju
geboren op 07 august 1983
Hyderabad, India

Dit proefschrift is goedgekeurd door de promotors:

Prof. dr. Detlef Lohse & Prof. dr. Andrea Prosperetti

'Endaroo Mahaanubhaavulu Andariki Vandanamulu ...'

My humble salute to those countless stalwarts who showed the way and brought the supreme bliss to me

- Tyagaraja Swamy, Carnatic musician and a composer from Tiruvarur, India.

CONTENTS

1

General introduction

Liquid-vapor phase transitions are omnipresent in nature. Boiling phenomenon can be widely seen in the kitchen to make coffee, in process industries to do distillations, and in thermal power-plants to generate vapor that drives turbines. Though numerous applications are involved, the understanding of the fluid dynamics of the process is only at a very basic level. The present work is an attempt to understand boiling phenomena at a fundamental level by combining fluid mechanics with heat transfer. First, a brief review of key words such as boiling, turbulence, and Rayleigh-Bénard convection is given. Later, they are combined to form a single subject of interest as *Boiling turbulent Rayleigh-Bénard convection* and understand them in detail.

1.1 Boiling

In a boiling process, liquid vaporizes by absorbing latent heat from its surroundings. For this to happen, the temperature in the liquid has to exceed a certain temperature called 'boiling temperature', at which the vapor pressure of the liquid just exceeds the ambient pressure from the surroundings. If we decrease the local ambient pressure, the temperature at which boiling occurs also decreases. The formed vapor and the surrounding heated liquid is carried away from its initial location due to buoyancy and transports large amounts of heat and mass.

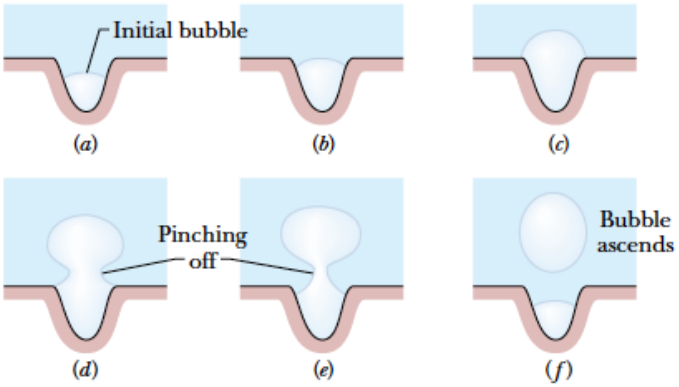

Figure 1.1: Boiling- bubble nucleation from the fissure of a hot pan of liquid. Taken from Jearl Walker's 'Boling and the Leidenfrost effect' [1]

To better explain this, let us heat a vessel with water or dip an electric heater in a pool of liquid. As time progresses quiescent cold water in the vessel becomes warmer by absorbing heat from the hot surface. As a consequence, convective motions will be observed. After a while, for sufficiently strong heating very tiny vapor bubbles in small numbers begin to appear (nucleate) at isolated places on the surface due to local temperature exceeding the boiling temperature of 100 ^{o} C at normal pressures. Most of the water in the vessel away from the hot surface is still at a temperature below the boiling temperature. With time, the local temperature of the bottom surface fluctuates around the boiling temperature and many more vapor bubbles eventually cover the entire bottom surface. Bubbles are observed at random locations on the surface and their number highly depends on the surface roughness. These bubbles start growing in size while still sticking to the bottom surface, see Figure 1.1(a-c). This stage of boiling is known as 'nucleate boiling'. Usually the observed nucleated bubbles are around tens of microns in size and can grow to a size of few hundred microns (fraction of a milli-meter) without detaching from the bottom surface. Some of the bubbles grow large, become buoyant, and pinch off from the surface (Figure 1.1e), while most of them still stick to the surface. Bubbles which come out of the hot surface condense and disappear if they encounter a cold current. Acoustic waves are generated because of bubble collapse and a kind of 'humming' noise can be heard. At this preliminary stage of boiling, a very few bubbles reach the top surface without condensation and escape to the environment. In Figure 1.2, a schematic sketch on surface heat flux q vs. wall superheat $(T_{wall} - T_{sat})$ in excess to the saturation temperature is shown. As mentioned, nucleated bubbles store thermal energy in the form of latent heat and hence the heat transfer rate in the 'nucleate

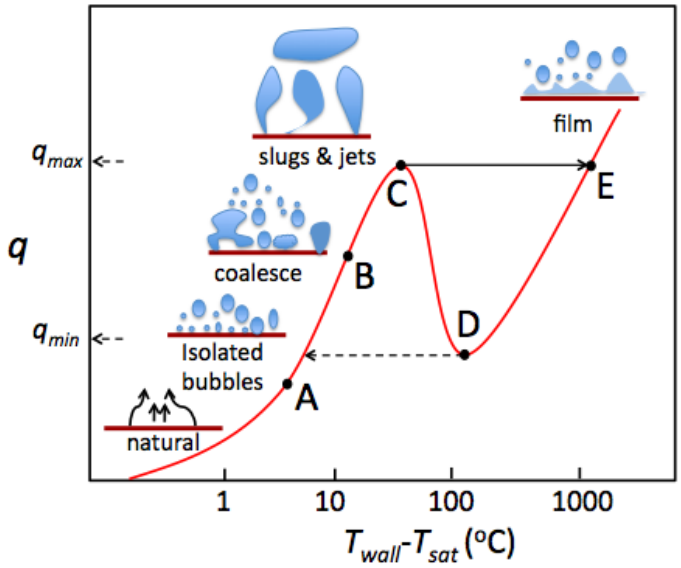

Figure 1.2: A typical sketch showing qualitative heat transport vs. superheating of the surface observed in boiling [6]. As super heating increases the observed changes from liquid to vapor phase are shown on the top of the curve.

boiling' stage is larger than the 'natural convection' stage, see line between points A and B in the same figure. As we increase the surface temperature many more bubbles appear and detach from the surface and coalesce forming slugs and jets of vapor. The heat transfer increases to a maximum value q_{max} where the surface is completely covered with a layer of vapor (point C).

From point C onwards, any further increase in the surface temperature decreases the heat transfer rate because of the poor thermal conducting behavior of the vapor layer * covering the surface, see region between C and D. This stage of boiling is known as 'transition boiling' because the formed vapor layer is unstable in most of the situations and is intermittently replaced with the nucleated vapor bubbles. In industrial equipment, a stable vapor layer in 'transition boiling' stage is not preferred due to excessive overheat of the component with a bad heat transport character. From the point D to E, radiation heat transport from the surface to the liquid becomes important and the heat transfer rate increases monotonically. This stage is known as 'film boiling'. Beyond point 'E', the surface temperature usually reaches the melting point and either the surface or the heater gets burned out. Generally, the transition and the film stages of boiling are difficult to see in a kitchen room experiment, but

*Liquid water is a better thermal conductor than water vapor at least by an order of magnitude

under carefully controlled conditions in a laboratory these stages can be seen. For historical and other details on boiling see Refs. [2–8].

1.2 Turbulence

The characteristic features of a turbulent flow are that it is unsteady, random, disorganized and highly dissipative, e.g., plumes from chimneys, water in a river, stirred coffee in a cup etc. Mathematically, the Navier-Stokes equations describe turbulent phenomena. Any deductive theory based on these equations is yet beyond the present knowledge of the scientific community. Many phenomenological approaches have been proposed and the most remarkable one is based on the energy cascade [9, 10], known as K41. In K41, energy at the large scales is cascading down to the small scales without any dissipation at the intermediate scales once it has arrived there, the injected energy is finally dissipated at the small scales by viscosity. Under homogeneous and isotropic conditions K41 predicts that in the inertial range the spectral energy is proportional to $k^{-5/3}$, where k is the wavenumber [11]. Most of the turbulent flows are inhomogeneous and anisotropic and the assumptions made in K41 are not applicable. For recent advances and approaches on turbulence see Refs. [12–14].

1.3 Rayleigh-Bénard convection

A liquid filled container heated from below and cooled from above is known as the Rayleigh-Bénard (RB) system and it has been of central importance in fluid dynamics for the past hundred years or so [15–20]. It is because of the complex dynamics observed in the system due to the interplay between buoyancy, inertial, and viscosity. The heat transferred from bottom to top significantly depends on the applied temperature difference, fluid properties, and the geometry of the system. The typical flow structures in RB convection are boundary layers, plumes, and a large scale circulation, see Ref. [19, 20]. Thermal boundary layers are present very near to the hot bottom and cold top plates where sharp variation in the temperature profile can be observed. A few unstable buoyant fluid elements, known as thermal plumes, detach from the boundary layers, rise (or falls) in the flow, and thus drive the large scale circulation (LSC). Once the LSC is present, the dynamics of the plume detachment depends on the LSC dynamics. This kind of mutual dependences of the dynamics make the problem non-trivial. Many other details such as the dependence of the heat transport on the applied temperature difference, and the large scale and small scale dynamics can be found in Refs. [20, 21].

1.4 Boiling turbulent Rayleigh-Bénard convection

As we have seen boiling convection is such a complex phenomena, which requires some specialization skills on different aspects of science such as material science, nucleation physics, heat transfer and fluid dynamics. In actual industrial problems on boiling the fundamental physical processes are tangled and impossible to isolate from each other. The observed heat transfer rate from the surface strongly depends on physical and chemical properties of the fluid and the surface. The complexity of the boiling process and its practical use attracted many engineers and scientists to propose several quantitative empirical relations with many fitting parameters. These empirical relations highly depend on the problem under consideration and a common theoretical model is completely absent even for a simplest case. Physicists are also attracted by this phenomena and tried constructing elementary models based on kinetic theory. Their models try to explain the key process for one or two bubbles getting nucleated in a quiescent fluid, but an overall effect, when many of them are present, any theory is still missing. Even if they existed, it were questionable whether they would work in a 'turbulent convection'? How to understand this complex problem from the fluid dynamicist viewpoint?

The focus of the present thesis is on understanding buoyant motion of vapor bubbles, which are modelled as point particles, in a turbulent Rayleigh-Bénard convection. As with many other multiphase disperse flows, given the present state of the art, this restriction is necessary to deal with a large number of bubbles. For this reason, finite volume effects, such as transport of vapor inside individual bubbles during their growth on the heated surface or the replenishment by cooler liquid of the volume vacated by departing bubble are unaccounted. However, the present work does indicate a very significant effect of the bubbles on the RB convection, which is strongly enhanced by the increased buoyancy provided by the bubbles and their motion relative to the liquid. Therefore, this work does not address the actual boiling phenomena, but it gives us a glimpse on understanding the role of nucleated vapor bubbles when present in turbulent convection.

1.5 A guide through the chapters

In Chapter 2, the effect of vapor bubbles on velocity fluctuations and energy dissipation rates in convective turbulence are addressed. The purpose of this chapter is two-fold. First, we present the mathematical model and the details on numerical simulations of a boiling turbulent Rayleigh-Bénard convection. Second, the difference brought by vapor bubbles on convection are discussed.

In Chapter 3, heat transport in boiling convection is studied for different strengths of thermal driving, number of bubbles, and degree of superheat. The reasons for the observed enhancement in heat transport is explained on the basis of enhanced buoyancy by bubbles and strengthened circulatory motion in the system. Further the changes observed in classical scaling laws on convection in case of boiling are discussed.

In Chapter 4, the structure functions and the intermittency of the temperature field are discussed. Vapor bubbles smoothen local thermal gradients by absorbing or releasing latent heat locally in the system. Thus, intermittency in the field is decreased.

In Chapter 5, the spatial distribution of heat flux and fluctuations and their dependency on large scale circulation in classical RB convection are discussed. The numerically found scaling laws on heat transport are in agreement with the Grossmann-Lohse (GL) model on convection and show a power-law behavior on the strength of buoyancy.

Finally, in Chapter 6 we summarize our complete work on boiling convection.

References

[1] J. Walker's essay about 'Boiling and the Leidenfrost effect' in *Fundamentals of Physics*, 8th edition, John Wiley & Sons (2008)

[2] S. Nukiyama, *The maximum and minimum values of the heat Q transmitted from metal to boiling heat water under atmospheric pressure*, J. Jap. Soc. Mech. Eng., **37**, 367-374 (1934): English translation in Int. J. Heat Mass Transfer, **9** 1419-1433 (1966).

[3] T. B. Drew and C. Mueller, *Boiling*, Trans. AIChE, **33**, 449-473 (1937).

[4] W. M. Rohsenow and J. P. Hartnet (Eds.), *Boiling*, Section 13 in Handbook of Heat Transfer, McGraw-Hill, Newyork (1973).

[5] W. M. Rohsenow, *What we don't know and do know about nucleate pool boiling heat transfer* , ASME HTD **104, 2**, 169-172 (1988).

[6] V. K. Dhir, *Boiling heat transfer*, Ann. Rev. Fluid Mech. **30**, 365 (1998).

[7] J. Kim, *Review of nucleate pool boiling bubble heat transfer mechanisms*, Int. J. Multiphase Flow, **35**, 1067-1076 (2009).

[8] L. P. Yarin, A. Mosyak, and G. Hetsroni, *Fluid Flow, Heat transfer and boiling in micro-channels*, Springer-Verlag, Berlin (2009).

[9] L. F. Richardson, *Atmospheric diffusion shown on a distance-neighbour graph* Proc. R. Soc. London Ser. A **110**, 709 (1926).

[10] A. N. Kolmogorov, *The local structure of turbulence in incompressible viscous fluid for very large Reynolds number* Dokl. Akad. Nauk. SSSR **30**, 9 (1941); **32**, 16 (1941), reproduced in Proc. R. Soc. London, Ser. A **434**, 9 (1991).

[11] U. Frisch, *Turbulence, the legacy of A. N. Kolmogorov*, (Cambridge Univ. Press, 1995).

[12] M. Oberlack, F. H. Busse, *Theories of Turbulence*, Springer Wien New York, (2002)

[13] J. Peinke, A. Kittel, S. Barth, M. Oberlack (Eds.) *Progress in turbulence*, Springer Berlin Heidelberg New York (2005)

[14] G. Falkovich, and K. R. Sreenivasan *Lessons from hydrodynamic turbulence*, Phys. Today, April, 43-49 (2006).

[15] Lord Rayleigh, *On convection currents in a horizontal layer of fluid, when the higher temperature in on the under side*, Philos. Mag., Ser. 6 **32**, 529 (1916).

[16] S. Chandrasekhar, *Hydrodynamic and hydromagnetic stability*, Oxford University Press, Oxford (1961).

[17] B. Saltzman (ed.), *Selected Papers on the Theory of Thermal Convection, with special application to the earth's planetary atmosphere*, Dover (1962).

[18] F.H. Busse, *Non-linear properties of thermal convection*, Rep. Prog. Phys., **41**: 1929-1967 (1978).

[19] L. P. Kadanoff, *Turbulent heat flow: Structures and scaling*, Phys. Today, **54**, 34 (2001).

[20] G. Ahlers, S. Grossmann, and D. Lohse, *Heat transfer and large scale dynamics in turbulent Rayleigh-Bénard convection*, Rev. Mod. Phys. **81**, 503 (2009).

[21] D. Lohse and K. Q. Xia, *Small-scale properties of turbulent Rayleigh-Bénard convection*, Ann. Rev. Fluid Mech. **42**, 335 (2010).

2

Effect of vapor bubbles on velocity fluctuations and dissipation rates in bubbly Rayleigh-Bénard convection *

Numerical results for kinetic and thermal energy dissipation rates in bubbly Rayleigh-Bénard convection are reported. Bubbles have a twofold effect on the flow: on the one hand they absorb or release heat to the surrounding liquid phase, thus tending to decrease the temperature differences responsible for the convective motion but, on the other, the absorbed heat causes the bubbles to grow, thus increasing their buoyancy and enhancing turbulence (or, more properly, pseudo-turbulence) by generating velocity fluctuations. This enhancement depends on the ratio of the sensible heat to the latent heat of the phase change, given by the Jakob number, which determines the dynamics of the bubble growth.

*Published as: R. Lakkaraju, L. E. Schmidt, P. Oresta, F. Toschi, R. Verzicco, D. Lohse, and A. Prosperetti, 'Effect of vapor bubbles on velocity fluctuations and dissipation rates in bubbly Rayleigh-Bénard convection', *Physical Review E*, **84**, 036312 (2011)

2.1 Introduction

It is well known that boiling is a very efficient heat transfer process [1, 2]. Bubbles growing near the heated surface absorb latent heat and cool it. Furthermore, the buoyant rise of the bubbles induces a turbulent, or pseudo-turbulent, motion in the liquid which brings cooler liquid from the bulk closer to the heated wall and mixes it. The physics involved in this process is very rich and complex and still far from being completely understood. In this work, which is a continuation of earlier studies [3, 4], we focus on the second aspect, namely the fluctuating motion induced by the bubbles and their thermal interaction with the surrounding liquid. For this purpose we consider a standard Rayleigh-Bénard setting in which a liquid undergoes natural convection in a cell the base of which is warmer than the top. Vapor bubbles are introduced in this flow and their effect on it is studied numerically. Recent experimental results on a similar system also show an enhanced heat transport compared with single-phase natural convection [5].

Several works exist on the buoyant rise of gas bubbles and their effect on the liquid motion [6–11]. What distinguishes the present work is that the mechanical coupling between the bubbles and the liquid is augmented and influenced by the thermal coupling which causes the bubble volume to change.

In the following, we first discuss briefly the mathematical formulation and numerical method and then focus on how bubbles promote turbulence and liquid velocity and temperature fluctuations in the Rayleigh-Bénard convection inside a cylindrical cell.

2.2 Governing equations

Details about the model used in this work can be found in [3]. The governing equations for the incompressible fluid flow under the Boussinesq approximation, augmented by the momentum and energy effects of the two-way coupled, point-like bubbles are [3, 12]

$$\nabla \cdot \mathbf{u} = 0, \tag{2.1}$$

$$\frac{D\mathbf{u}}{Dt} = -\frac{1}{\rho}\nabla p + \nu\nabla^2\mathbf{u} + \beta(T - T_{sat})\mathbf{g} + \sum_{i=1}^{N} \mathbf{f}_i \delta(\mathbf{x} - \mathbf{x}_i), \tag{2.2}$$

$$\frac{DT}{Dt} = \frac{k}{\rho c_p}\nabla^2 T + \frac{1}{\rho c_p}\sum_{i=1}^{N} \mathbf{Q}_i \delta(\mathbf{x} - \mathbf{x}_i)\,. \tag{2.3}$$

Here $\mathbf{u}$, p and T are the liquid velocity, pressure and temperature fields, ρ, ν, k and c_p the (constant) liquid density, kinematic viscosity, thermal conductivity and specific

heat, β is the isobaric thermal expansion coefficient and N the total number of bubbles. The thermal diffusivity is defined as $\kappa = k/(\rho c_p)$. The mechanical and thermal forcings at the location $\mathbf{x}_i$ of the i-th bubble are given by $\mathbf{f}_i = \frac{4}{3}\pi r_{b_i}^3 ([D\mathbf{u}/Dt]_{\mathbf{x}_i} - \mathbf{g})$ and $\mathbf{Q}_i = 4\pi r_{b_i}^2 h_{b_i} (T_{sat} - T_i)$, respectively. Here r_{b_i} is the radius of the i-th bubble, T_i the liquid temperature at the bubble location and h_{b_i} the bubble convective heat transfer coefficient; T_{sat} is the saturation temperature at the system's pressure.

The bubbles are tracked by solving the following dynamical equation in which their mass is neglected (see e.g. [13]):

$$\begin{aligned} C_A\rho \left[\frac{4}{3}\pi r_{b_i}^3 \left(\frac{D\mathbf{u}}{Dt} - \frac{d\mathbf{V_b}}{dt}\right) + (\mathbf{u} - \mathbf{V_b}) \frac{d}{dt}\left(\frac{4}{3}\pi r_{b_i}^3\right)\right] \\ -\frac{1}{2}\pi C_D \rho r_{b_i}^2 \mid \mathbf{V_b} - \mathbf{u} \mid (\mathbf{V_b} - \mathbf{u}) + \frac{4}{3}\pi r_{b_i}^3 \rho \frac{D\mathbf{u}}{Dt} \\ +C_L \frac{4}{3}\pi r_{b_i}^3 \rho (\nabla \times \mathbf{u}) \times (\mathbf{V_b} - \mathbf{u}) - \frac{4}{3}\pi r_{b_i}^3 \rho \mathbf{g} = 0 \end{aligned} \tag{2.4}$$

in which $C_A = 1/2$, $C_L = 1/2$ are the added mass and lift coefficients [14, 15]. The drag coefficient is modelled as mentioned in [16, 17] as follows:

$$C_D = \frac{16}{Re_b}\left[1 + \frac{Re_b}{8 + \frac{1}{2}\left(Re_b + 3.315\sqrt{Re_b}\right)}\right] \tag{2.5}$$

in which $Re_b = 2r_b \mid \mathbf{V_b} - \mathbf{u} \mid /\nu$, with $\mathbf{V_b}$ the bubble velocity, is the bubble Reynolds number.

In view of the small temperature differences, the radial inertia of the bubbles can be neglected, which implies that the vapor pressure inside the bubble equals the local ambient value. This quasi-equilibrium relation should be corrected for the effect of surface tension, but we neglect this feature for simplicity and also so as not to obscure, by the introduction of a fairly minor effect, the impact of bubble growth on the dynamics of the system under consideration.

For example, for bubbles with a typical size of 50 μm (see e.g. figure 2.1) the surface tension overpressure amounts to about 2% of one atm.

The parameter values specified below show that, in the present simulations, flow-induced pressure changes are small and so are hydrostatic effects so that the vapor pressure can be assumed to remain essentially constant. As a consequence, since the vapor is at saturation, the bubble wall temperature can be taken to be the saturation temperature T_{sat} at the ambient pressure. The evolution of the bubble radius can therefore be directly linked to the thermal energy exchange with the liquid by

$$h_{fg}\frac{d}{dt}\left(\frac{4}{3}\pi r_{b_i}^3 \rho_v\right) = 4\pi r_{b_i}^2 h_{b_i} (T_i - T_{sat}) \tag{2.6}$$

in which h_{fg} is the latent heat of the liquid and ρ_v the vapor density.

The heat transfer coefficient of each bubble is expressed in terms of the Nusselt number

$$Nu_b = \frac{2r_b h_b}{k}. \tag{2.7}$$

by a semi-empirical formula which interpolates between the value $Nu_b = 2$ at very low Jakob numbers and small relative velocities and

$$Nu_b = 2\sqrt{\frac{2r_b|\mathbf{V_b} - \mathbf{u}|}{\pi\kappa}} \tag{2.8}$$

at large relative velocities; see [3] for details.

Our use of the point particle approximation is justified by the facts that the Kolmogorov length scale is always larger than the bubble mean radius and, secondly, that the volume fraction for the bubble phase is at most only 0.2% (see e.g. [18]).

The numerical treatment of the equations follows that described in [19, 20] and in [3]. Briefly, the field equations are discretized in space by a second-order finite difference scheme based on the projection method on a non-uniform staggered grid with $33 \times 25 \times 65$ points in the azimuthal, radial and axial directions respectively. Time is advanced by the third order Runge-Kutta scheme with a constant non-dimensional time step of 2×10^{-4} dimensionless time units. The adequacy of this spatial and temporal discretization was demonstrated in [3] and a further test is described later.

In each computational cell the forces exerted by the bubbles on the liquid are replaced by an equivalent system of forces at the grid nodes constructed in such a way as to produce the same net resultant and couple on the liquid as the original forces (see [3]). An analogous strategy is followed for the bubble-related sources in the right-hand side of the energy equation (2.3) so that the total amount of heat that each bubble exchanges with the liquid is preserved. The interpolations used in these steps are second-order accurate and therefore consistent with the overall spatial accuracy of the discretization

Bubbles are removed when they reach the top plate of the cell and re-injected with their lower surface tangent to the bottom plate with the local fluid velocity and an initial radius of 12.5 μm (see [3]). The results were found to be insensitive to the bubble injection size which was varied between 6.5 and 25 μm in a few cases. The initial injection location was chosen randomly from a uniform distribution.

The saturation temperature T_{sat} was taken as 100 °C, namely the saturation temperature of water at normal pressure, while the bottom hot (T_h) and top cold (T_c) temperatures were taken as $T_h = T_{sat} + \frac{1}{2}\Delta$ and $T_c = T_{sat} - \frac{1}{2}\Delta$ respectively, with $\Delta \equiv T_h - T_c = 0.25$ K. This temperature difference would not correspond to a realistic boiling situation, but it enables us to focus on the physics of the bubble-induced flow at an affordable computational cost. The fluid properties used are those of water at 100 °C.

The simulations were conducted in a cylindrical cell with an aspect ratio (diameter/height) $D/L = 1/2$; the height was 17.9 mm. The equations were solved for fixed Rayleigh $Ra = g\beta\Delta L^3/\nu\kappa$ and Prandtl $Pr = \nu/\kappa$ numbers. The thermal energy balance of the bubble with the surrounding fluid, equation (2.6), introduces a third parameter, the Jakob number

$$Ja = \frac{\rho c_p (T_h - T_{sat})}{\rho_v h_{fg}}, \tag{2.9}$$

which controls the bubble growth rate. For $Ja = 0$, the latent heat is infinite and bubbles cannot grow or shrink.

Velocities are non-dimensionalized by the so-called free fall velocity $U = \sqrt{g\beta\Delta L}$, lengths by the cylinder height L, and times by L/U.

2.3 Direct numerical simulations

With the data specified above, the Jakob number for a water-vapor system would equal 1.3 approximately. However, in the simulations, we vary the Jakob number for fixed $Ra = 2 \times 10^5$ and $Pr = 1.75$ (the value for water at 100 °C) to isolate the effect of bubble volume changes on the flow phenomena. The number of bubbles is kept fixed at 10,000. The vapor volume fraction calculated with the initial bubble radius is about 1.85×10^{-5}.

An additional check on the grid independence of the results was carried out for $Ja = 1.0$ by comparing the total heat transport for the standard grid, with $33 \times 25 \times 65$ cells, and a finer grid with $33 \times 40 \times 80$ cells. The statistical properties of the flow were within 0.6%, indicating that the resolution provided by the standard grid is sufficient and the flow scales are properly resolved.

The flow properties (Table 1) were calculated once the system had reached a statistical stationary state as revealed by monitoring the total heat transport and the liquid velocity fluctuations. Columns II, III and IV in the table show the time- and volume-averaged bubble mean radius $\bar{r}_b$, Kolmogorov length scale η, and Taylor length scale $\lambda = \langle u' \rangle_{t,V} / \langle |\nabla u'| \rangle_{t,V}$, respectively. Here and elsewhere in this chapter angle brackets denote averages over the variable(s) indicated by the subscripts V for volume, t for time and, later, A for the cross-sectional area; quantities averaged over all the bubbles and over time are indicated by an overline. The mean liquid velocity fluctuation $\langle u' \rangle_{t,V}$ is defined by

$$\langle u' \rangle = \left\langle \sqrt{\frac{1}{3} \mid \mathbf{u}(\mathbf{x},t) - \langle \mathbf{u} \rangle_t(\mathbf{x}) \mid^2} \right\rangle_{t,V} \tag{2.10}$$

Table 2.1: Summary of length and velocity scales for the present simulations for different Jakob numbers; L is the cell height, η the Kolmogorov length scale, λ the Taylor length scale, $\bar{r}_b$ the bubble radius averaged over time and over all the bubbles, $\langle u' \rangle_{t,V}$ the time- and volume-averaged r.m.s. liquid velocity fluctuation, $\overline{V_{br}}$ the mean bubble-liquid vertical relative velocity and Re_λ the Taylor Reynolds number.

Ja	$10^2\bar{r}_b/L$	$10^2\eta/L$	$10^2\lambda/L$	$\langle u' \rangle_{t,V}/\overline{V_{br}}$	Re_λ
0.00	0.071	6.16	–	0.004	–
0.10	0.22	0.77	3.31	0.20	4.79
0.15	0.24	0.68	3.43	0.21	6.49
0.20	0.26	0.64	3.82	0.22	9.28
0.25	0.27	0.60	3.89	0.23	10.76
0.30	0.28	0.58	4.17	0.24	13.42
0.40	0.31	0.54	4.39	0.24	17.15
0.60	0.34	0.49	4.90	0.26	25.97
0.80	0.37	0.46	5.34	0.27	35.57
1.00	0.39	0.45	5.62	0.28	40.03

and the mean liquid velocity gradient by

$$\langle |\nabla u'| \rangle = \left\langle \sqrt{\frac{1}{3} \mid \nabla \mathbf{u}(\mathbf{x},t) - \langle \nabla \mathbf{u} \rangle_t(\mathbf{x}) \mid^2} \right\rangle_{t,V} \tag{2.11}$$

With the present parameter values, the pattern of the single-phase flow in the cell is a roll with an approximately horizontal axis. For reasons explained below, the introduction of bubbles with $Ja = 0$, which forces them to maintain a fixed radius as noted before, modifies the flow pattern to a toroidal vortex with the descending stream near the axis and the ascending stream in the surrounding volume. As Ja increases and the bubble volume is allowed to change and, in particular, to grow in the warmer liquid regions, a flow pattern qualitatively similar to the single-phase one but with higher velocities is gradually established. As they are introduced at the hot plate, bubbles are swept up by the annular roll adding to its buoyancy and thereby increasing the intensity of the circulation. It is also found that in this regime the axis of the roll rotates in a horizontal plane, as in single-phase RB flow [21].

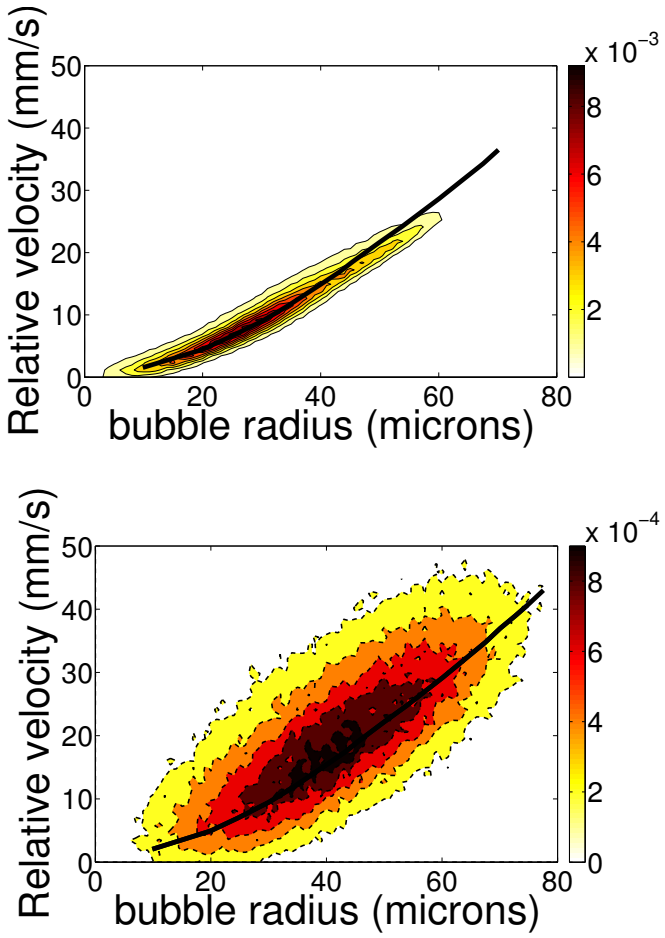

Figure 2.1: Isolines of the bubble probability density function in the radius-relative velocity plane for $Ja = 0.1$ (upper) and $Ja = 1$ (lower). The solid black line shows the terminal velocity in a quiescent fluid. The bubbles are injected with an initial radius of 12.5 μm.

2.4 Bubble relative velocity

For $Ja = 0$ the bubbles maintain the same radius with which they are injected and the vast majority of them rises relative to the liquid with a velocity very close to the terminal velocity of about 1.7 mm/s. To give an impression of the major effect of a non-zero Jakob number on the dynamics of the bubble-liquid interaction we show in figure 2.1 isolines of the bubble probability density function in the radius-

relative velocity plane for $Ja = 0.1$ (upper) and $Ja = 1$ (lower). The solid black line in these figures is the terminal velocity as given by a balance of buoyancy and drag as computed from (2.5). As bubble growth and, with it, increased buoyancy, is allowed, the spread of the bubbles' velocity relative to the liquid's increases considerably. This feature demonstrates the increasing importance of the additional forces present in the bubble equation of motion (2.4) with increasing bubble volume.

2.5 Liquid velocity fluctuations and anisotropy

A measure of the turbulence intensity is given by the ratio $\langle u' \rangle_{t,V} / \overline{V_{br}}$ where $\overline{V_{br}}$ is the mean bubble-liquid vertical relative velocity given by

$$\overline{V_{br}} = \langle \frac{1}{N} \sum_{i=1}^{N} \left| V_{bz,i}(t) - u_{z,i}(t) \right| \rangle_t . \tag{2.12}$$

Column V of the table 5.2 shows that, in the present simulations, this quantity is small for $Ja = 0$ which, as noted above, corresponds to non-growing bubbles, but becomes of the order of 20-30% as Ja increases to 1. Note that here the turbulence intensity is larger than that in the case of pseudoturbulence without heating and with periodic boundary conditions in all directions [9], where $\langle u' \rangle_{t,V} / \overline{V_{br}}$ was found to be of the order of 6%.

In that work [9], which was quantitatively confirmed by independent simulations by Calzavarini [22], the bubbles did not grow and the drag law was pure Stokes. We have repeated our simulations with $Ja = 0$ and the same drag law, still finding considerably larger velocity fluctuations than reported for the case of pseudoturbulence with periodic boundary conditions and no heating. Thus we conclude that the reason for this difference lies in the nature of the two flows investigated. The work of [9] concerns the rise of fixed-radius bubbles in a quiescent liquid in a cube with periodic boundary conditions not only on the sides, but also on the top and bottom. In that system the only liquid flow is induced by the bubbles and, in a frame of reference with zero mean flow, the bubbles rise while, by continuity, the liquid descends. The velocity of the two phases is therefore mostly parallel and the bubbles distribute statistically uniformly (but of course accumulate in vortices, which however are statistically uniformly distributed over the flow volume). In the present system, on the other hand, liquid flow is driven by buoyancy in addition to the bubbles and the presence of impervious top and bottom boundaries causes the appearance of regions where the tendency of the bubbles to rise encounters nearly horizontal mean liquid streamlines. As noted before, bubbles are also swept up by the ascending convection current as they are introduced at the bottom boundary. All of these factors

cause a much more complex situation and presumably marked non-uniformities in the vortex and thus also bubble distribution. We believe that this is the explanation for the difference between the present work and that of [9]. The velocity fluctuations of course increase substantially when the bubbles are allowed to grow.

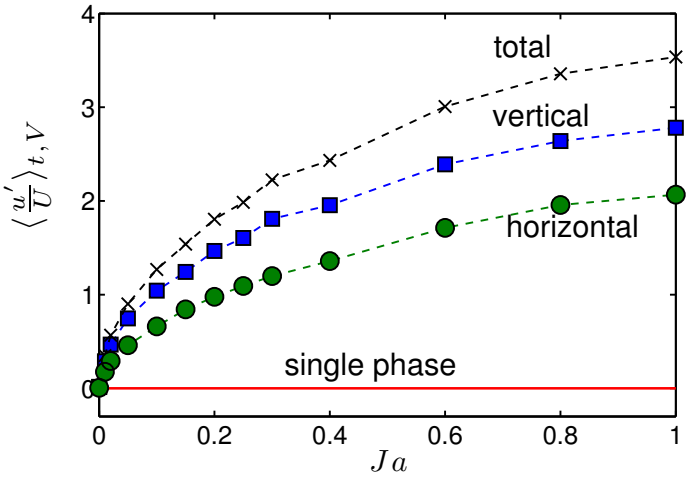

Figure 2.2: The volume- and time-averaged horizontal (-○-), vertical (-⊡-) and total (-×-) velocity fluctuations as functions of the Jakob number.

It is also interesting to note that the velocity fluctuations are far from isotropic. Figure 2.2 shows the volume- and time-averaged liquid velocity fluctuations in the vertical and horizontal directions. The fluctuations become more and more anisotropic with increasing Jakob number. Velocity fluctuations for the single-phase case are basically zero as the flow is essentially laminar for the Rayleigh number used here.

2.6 Kinetic and thermal energy dissipations

The normalized time- and volume-averaged kinetic energy dissipation rate $\langle \varepsilon_K \rangle_{t,V} = \nu \langle | \nabla \mathbf{u} |^2 \rangle_{t,V}$ is shown as a function of the Jakob number in figure 2.3. For comparison, the energy dissipation rate for single-phase convection is also shown by the continuous line. It can be observed that dissipation in the bubbly flow is generally higher than for the single-phase flow. However, for very small Jakob numbers, the opposite behavior is found as figure 2.3b shows: for these Jakob numbers energy dissipation is less which implies that turbulence is attenuated. The explanation is that, for $Ja = 0$, the bubbles have an effectively infinite heat capacity and therefore they can absorb or release heat to the surrounding fluid while remaining at T_{sat}, which

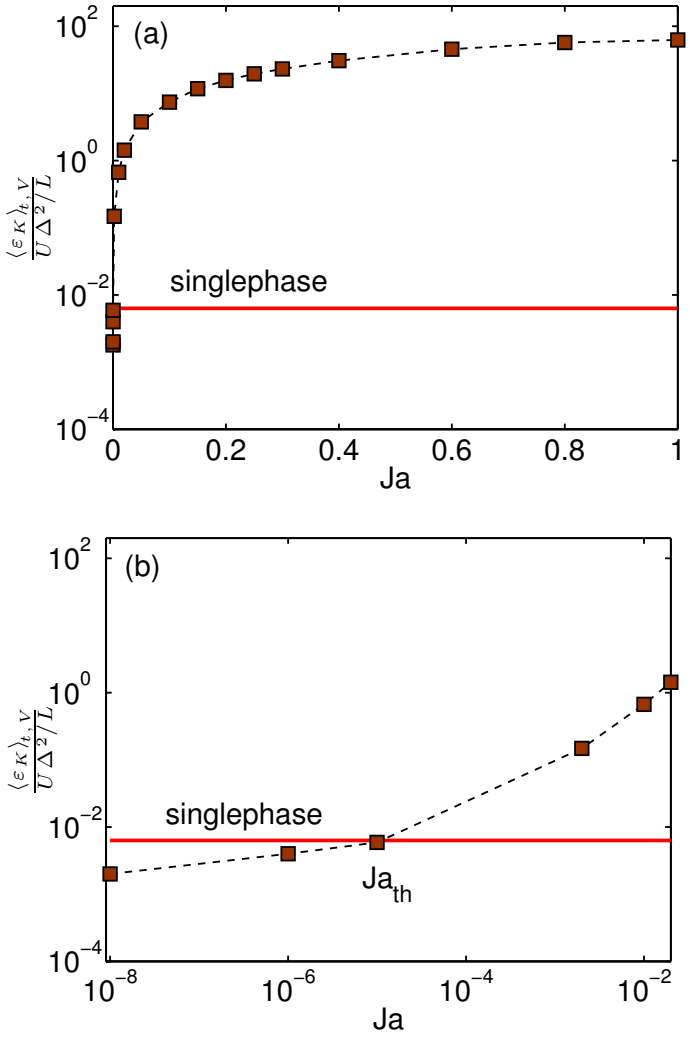

Figure 2.3: (a) Normalized kinetic energy dissipation rate as a function of the Jakob number Ja. In (b), the energy dissipation rate is shown for very low Ja, $10^{-8} \leq Ja \leq 10^{-2}$ on a log-log scale. In both figures the horizontal solid line shows the single-phase value for reference.

also equals the mean temperature of the hot and the cold plates. The net effect is a tendency to "short-circuit" the temperature difference and, therefore, a tendency to the quenching of the natural convection. The same effect was found in [3]. This process is responsible for the transition mentioned earlier from the annular roll of the single-phase case to the lower-energy toroidal roll prevailing for small Ja. The

tendency of the bubbles to reduce temperature differences is always present but, with increasing *Ja*, it is overshadowed by the increased buoyancy provided to the two-phase medium. The bubbles rise faster and, by mechanically stirring the liquid phase, increase the kinetic energy dissipation rate.

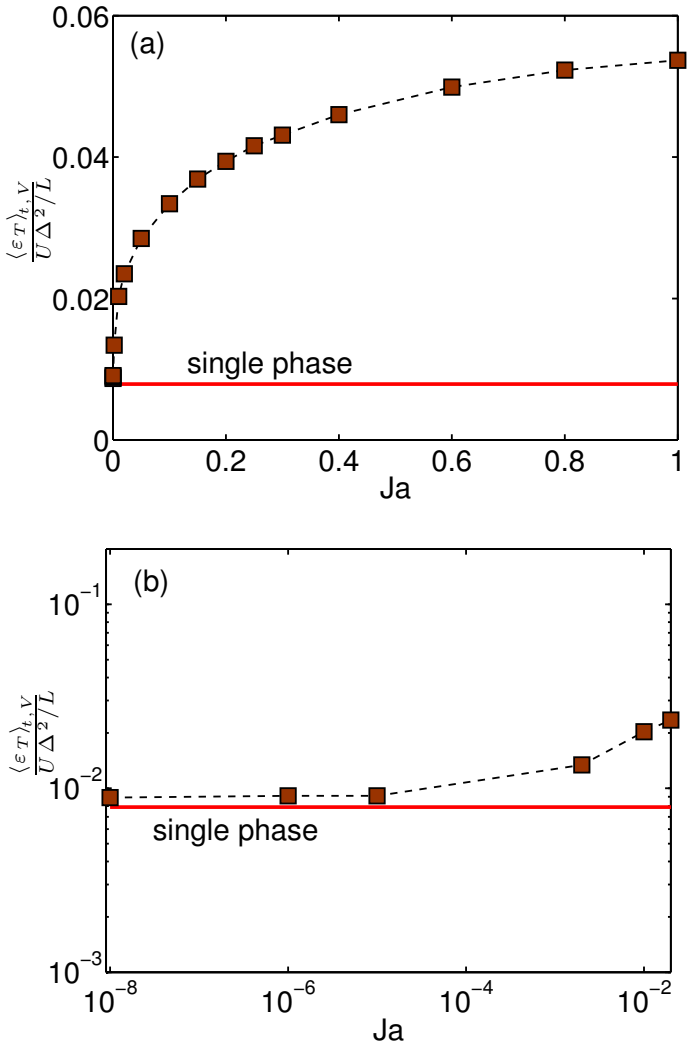

Figure 2.4: (a) Normalized thermal energy dissipation rate as a function of the Jakob number *Ja*. In (b), the energy dissipation rate is shown for very low *Ja*, $10^{-8} \leq Ja \leq 10^{-2}$ on a log-log scale. In both figures the horizontal solid line is the single-phase value for reference.

The normalized time- and volume-averaged thermal energy dissipation rate $\langle \varepsilon_T \rangle_{t,V} =$

$\kappa\langle|\nabla T|^2\rangle_{t,V}$ is shown as a function of the Jakob number in figure 2.4, where the horizontal solid line is the single-phase result. Unlike the kinetic energy dissipation, even non-growing bubbles with $Ja = 0$ slightly increase $\langle\varepsilon_T\rangle_{t,V}$. The reason lies in the fact that the bubble surface temperature is fixed which causes a local cooling or heating of the surrounding liquid.

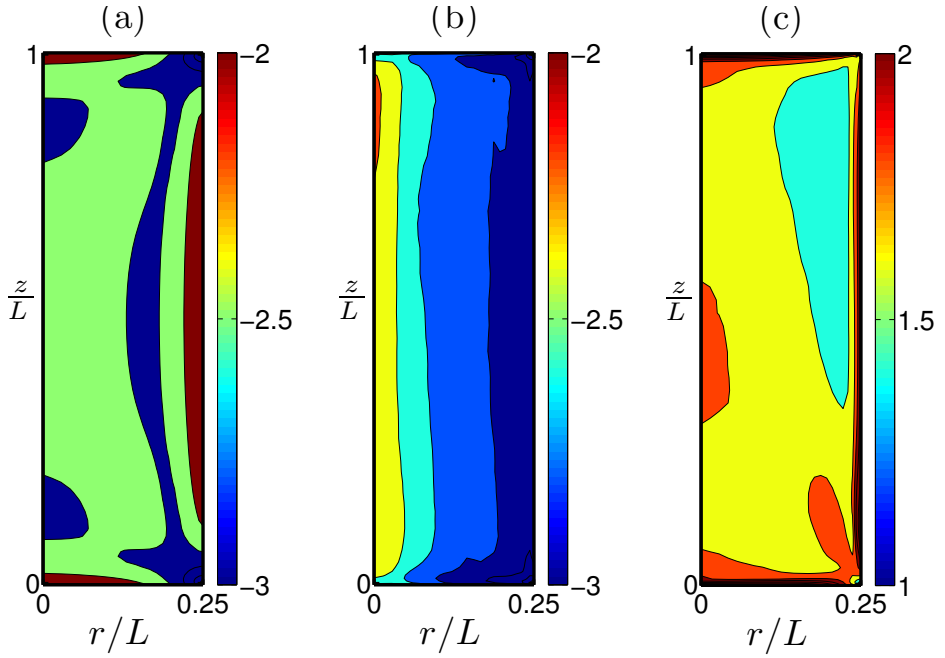

Figure 2.5: Angle-averaged kinetic energy dissipation $\langle\varepsilon_K\rangle_{t,\phi}$ normalized by U^3/L in the $r-z$ plane; (a) single phase; (b) $Ja = 0.0$ (non-growing 10^4 bubbles); (c) $Ja = 1.0$ (growing 10^4 bubbles). The color scale is logarithmic and it is different in (c) as compared to (a) and (b).

Figure 2.5 compares the normalized kinetic energy dissipation rate averaged over the azimuthal angle and time, $L\nu\langle|\nabla\mathbf{u}|^2\rangle_{t,\phi}/U^3$, in single-phase (figure 2.5a) and two-phase flow with $Ja = 0$ (figure 2.5b) and $Ja = 1$ (figure 2.5c); note the different (gray) color scales in these three figures. The single-phase annular roll is characterized by a relatively strong dissipation near the boundaries, as expected, and by small dissipation elsewhere. The change to a toroidal roll caused by the introduction of non-growing bubbles (figure 2.5b, $Ja = 0$), results in strong gradients in the relatively thin central region seat of descending flow, surrounded by a larger volume of smaller ascending velocities and smaller gradients. Bubbles with $Ja = 1$ restore a flow pattern with a horizontal roll qualitatively similar to the single-phase one but

with higher velocities. The resulting distribution of the dissipation resembles the single-phase one, but is considerably higher.

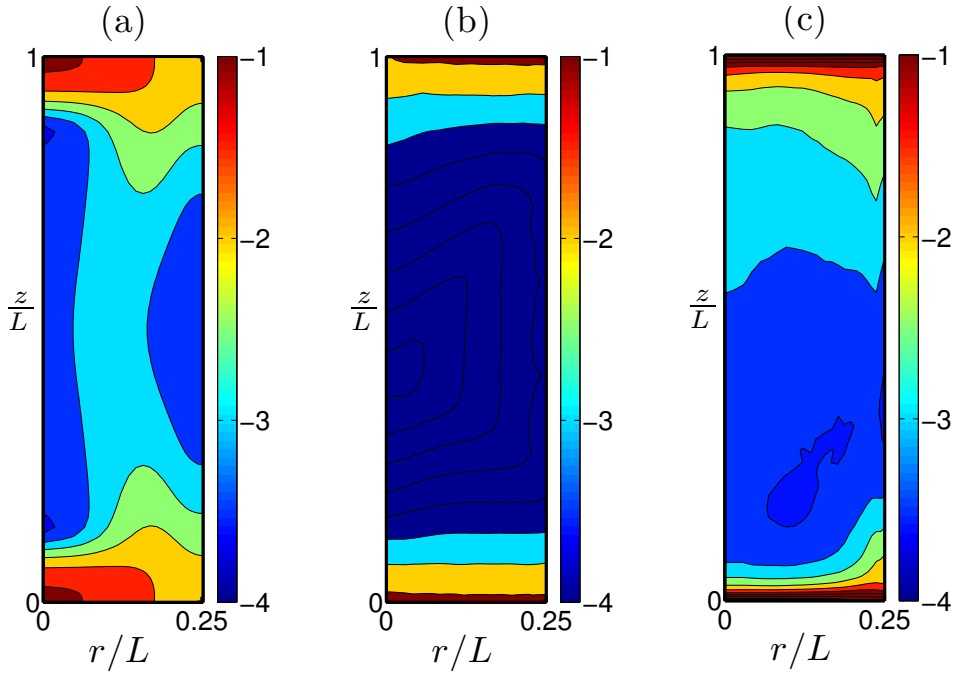

Figure 2.6: Angle-averaged thermal energy dissipation $\langle \varepsilon_T \rangle_{t,\phi}$ normalized by $U\Delta^2/L$ in the $r-z$ plane; (a) single phase; (b) $Ja = 0.0$ (non-growing 10^4 bubbles); (c) $Ja = 1.0$ (growing 10^4 bubbles). The (gray) color scale is logarithmic.

The normalized thermal energy dissipation rate $L\kappa\langle|\nabla T|^2\rangle_{t,\phi}/(U\Delta^2)$ averaged over time and the azimuthal direction is shown in figure 2.6. The effects of the large-scale circulation with strong thermal gradients on the hot and cold plates prevailing in the single-phase case can be observed in figure 2.6a. After introducing non-growing bubbles ($Ja = 0$), the temperature gradients are smoothed (figure 2.6b) and greatly reduced. For growing bubbles ($Ja = 1.0$, figure 2.6c) the temperature differences in the bulk region are still smoothed, but the enhanced convection raises the thermal dissipation with respect to the $Ja = 0$ case.

2.7 Liquid temperature

Figure 2.7a shows the vertical temperature profile averaged over the horizontal cross section as a function of z for different Jakob numbers. Figure 2.7b shows the normal-

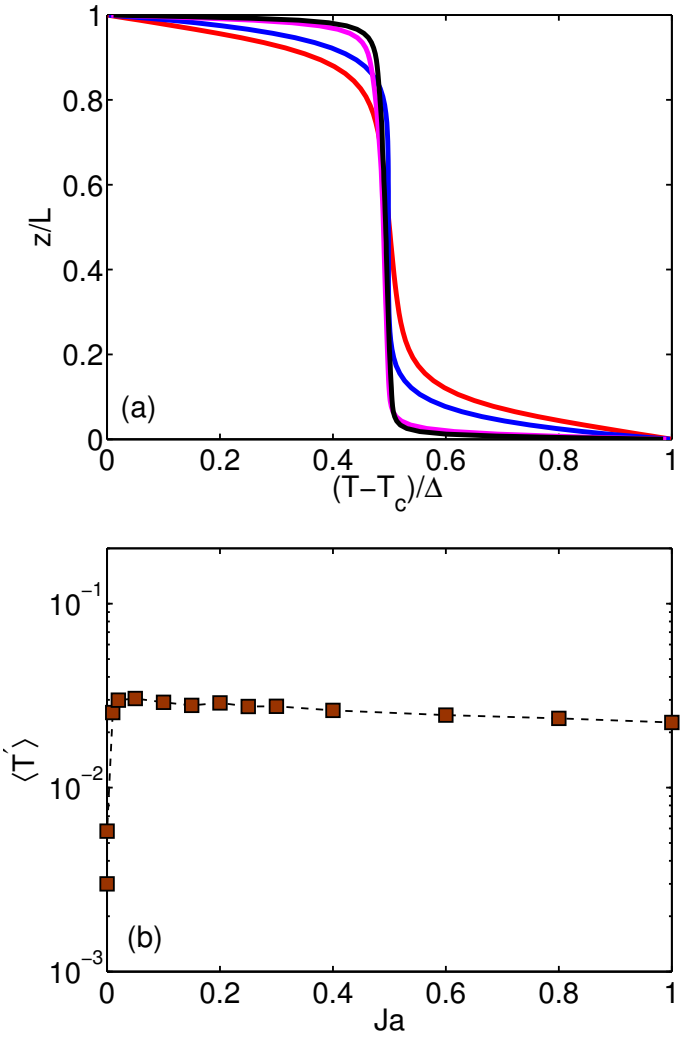

Figure 2.7: (a) Vertical temperature profile averaged over the horizontal cross section for the single-phase case (red), $Ja = 0$ (blue), $Ja = 0.1$ (magenta) and $Ja = 0.8$ (black). In (b), the volume averaged r.m.s. temperature fluctuation, $\langle T' \rangle$ is shown as a function of the Jakob number, on a linear-log scale.

ized volume- and time-averaged r.m.s. temperature fluctuations $< T' >= \sqrt{\langle (T - \langle T \rangle_t)^2 \rangle_{t,V}}/\Delta$. The presence of bubbles decreases the thermal boundary layer thickness near both plates even for $Ja = 0$. The origin of this reduction lies in the fact that, since the bubble temperature $T_{sat} = \frac{1}{2}(T_h + T_c)$ remains constant, the mere presence of the bubbles,

whether they be allowed to grow or not, has the effect of cooling the liquid near the hot plate and warming it up near the cold one. Of course, the effect increases with Ja and leads to a thinning of the thermal layer.

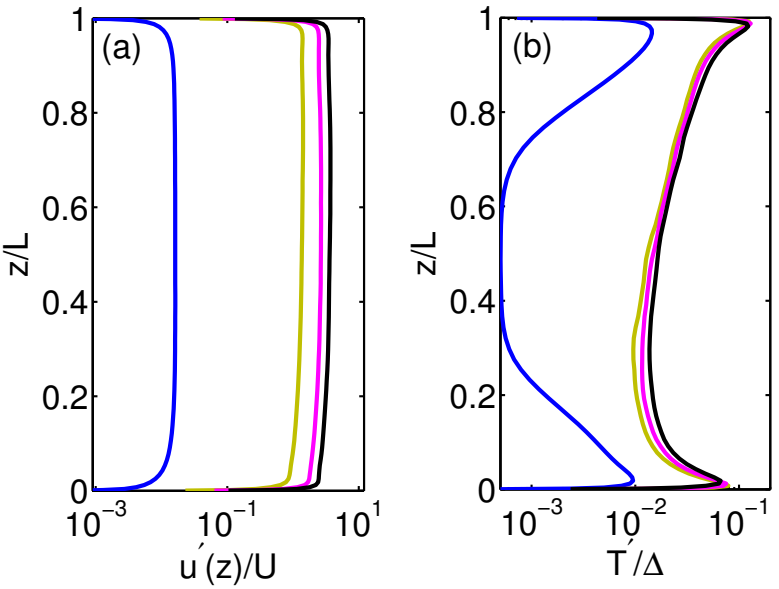

Figure 2.8: Normalized vertical velocity $u'(z)/U$ and temperature $T'(z)/\Delta$ fluctuations averaged over the horizontal cross section as functions of the vertical coordinate z; $Ja = 0$ (blue), $Ja = 0.01$ (olive), $Ja = 0.1$ (magenta) and $Ja = 0.8$ (black).

Figure 2.8 shows the normalized velocity and temperature fluctuations averaged over time and the horizontal cross section as functions of the vertical coordinate. As expected, the velocity fluctuations (figure 2.8a) decrease in the viscous boundary layers near the plate but are otherwise fairly constant and increase with Ja. The temperature fluctuations exhibit marked boundary layers near the plates due to the fact that, with their fixed interface temperature, bubbles behave as "cold spots" or "hot spots" near the bottom or top plates thus inducing relatively strong temperature differences with respect to the adjacent liquid.

2.8 Conclusions

The present numerical investigation considered the kinetic and thermal energy dissipation rates in a two-phase Rayleigh-Bénard convection in a cylindrical cell, where 10^4 saturated vapor bubbles are injected into the flow. Due to their fixed surface

temperature, bubbles tend to smooth the liquid temperature differences by absorbing and releasing heat and add vertical momentum to the flow with their buoyancy. The balance between these competing effects depends on the ratio of the sensible heat to the latent heat of the liquid, as quantified by the Jakob number *Ja* defined in (2.9). For very small *Ja*, the bubble volume change is small and the absorption or release of heat dominate over the buoyancy effect. The outcome is a reduction of the driving force of the circulation with a corresponding attenuation of the kinetic energy dissipation. The added buoyancy however starts becoming dominant already at small *Ja* with a strong enhancement of the kinetic and thermal energy dissipations.

References

[1] V. K. Dhir, *Boiling heat transfer*, Ann. Rev. Fluid Mech. **30**, 365 (1998).

[2] J. Kim, *Review of nucleate pool boiling bubble heat transfer mechanisms*, Int. J. Multiphase Flow**35**, 1067 (2009).

[3] P. Oresta, R. Verzicco, D. Lohse, and A. Prosperetti, *Heat transfer mechanisms in bubbly Rayleigh-Bénard convection*, Phys. Rev. E **80**, 026304 (2009).

[4] L. E. Schmidt, P. Oresta, F. Toschi, R. Verzicco, D. Lohse, and A. Prosperetti, *Modification of turbulence in Rayleigh-Bénard convection by phase change*, New J. Phys. **13**, 025002 (2011).

[5] J. Q. Zhong, D. Funfschilling, and G. Ahlers, *Enhanced heat-transport by turbulent two-phase Rayleigh-Bénard convection*, Phys. Rev. Lett. **102**, 124501 (2009).

[6] L. van Wijngaarden, *On Pseudo Turbulence*, Theor. Comp. Fluid Dyn. **10**, 449 (1998).

[7] E. Climent, and J. Magnaudet, *Large-scale simulations of bubble-Induced convection in a liquid layer*, Phys. Rev. Lett. **82**, 4827 (1999).

[8] O. Druzhinin, and S. Elgobashi, *Direct numerical simulation of a three-dimensional spatially-developing bubble-laden mixing layer with two-way coupling*, J. Fluid Mech. **429**, 23 (2001).

[9] I. Mazzitelli, and D. Lohse, *Evolution of energy in flow driven by rising bubbles*, Phys. Rev. E **79**, 066317 (2009).

[10] F. Toschi, and E. Bodenschatz, *Lagrangian properties of particles in turbulence*, Ann. Rev. Fluid Mech. **41**, 375 (2009).

[11] J. M. Mercado, D. C. Gomez, D. van Gils, C. Sun, and D. Lohse, *On bubble clustering and energy spectra in pseudo-turbulence*, J. Fluid Mech. **650**, 287 (2010).

[12] L. Wang, and M. R. Maxey, *The motion of microbubbles in a forced isotropic and homogeneous turbulence*, App. Sci. Res. **51**, 291 (1993).

[13] J. Magnaudet, and I. Eames, *The motion of high Reynolds number bubbles in inhomogeneous flows*, Ann. Rev. Fluid Mech. **32**, 659 (2000).

[14] T. R. Auton, *The lift force on a spherical body in a rotational flow*, J. Fluid Mech. **183**, 199 (1987).

[15] E. A. van Nierop, S. Luther, J. J. Blumink, J. Magnaudet, A. Prosperetti, and D. Lohse, *Drag and lift forces on bubbles in a rotating flow*, J. Fluid Mech. **571**, 439 (2007).

[16] R. Mei, and J. F. Kalusner, *Unsteady force on a spherical bubble at finite Reynolds number with small fluctuations in the free stream velocity*, Phys. Fluids A **4**, 63 (1992).

[17] R. Mei, J. F. Kalusner, and C. J. Lawrence, *A note on the history force on a spherical bubble at finite Reynolds number*, Phys. Fluids **6**, 418 (1994).

[18] F. Lucci, A. Ferrante, and S. Elghobashi, *Modulation of isotropic turbulence by particles of Taylor-length-scale size*, J. Fluid Mech. **650**, 5 (2010).

[19] R. Verzicco, and P. Orlandi, *A Finite-difference scheme for three-dimensional incompressible flows in cylindrical coordinates*, J. Comp. Phys. **123-2**, 402 (1996).

[20] R. Verzicco, and R. Camussi, *Numerical experiments on strongly turbulent thermal convection in a slender cylindrical cell*, J. Fluid Mech. **477**, 19 (2003).

[21] G. Ahlers, S. Grossmann, and D. Lohse, *Heat transfer and large scale dynamics in turbulent Rayleigh-Bénard convection*, Rev. Mod. Phys. **81**, 503 (2009).

[22] E. Calzavarini, private communication (2011).

3

Heat transport in boiling turbulent Rayleigh-Bénard convection *

Boiling is an extremely effective way to promote heat transfer from a hot surface to a liquid due to several mechanisms many of which are not understood in quantitative detail. An important component of the overall process is that the buoyancy of the bubbles compounds with that of the liquid to give rise to a much enhanced natural convection. In this chapter we present a numerical study of this two-phase Rayleigh-Bénard convection process. We consider a cylindrical cell with a diameter equal to its height. The cell base and top are held at temperatures above and below the boiling point of the liquid, respectively. By keeping the temperature difference constant and changing the liquid pressure we study the effect of the liquid superheat in a Rayleigh number range that, in the absence of boiling, would be between 2×10^6 *and* 5×10^9*. We find a considerable enhancement of the heat transfer and study its dependence on the bubble number, the degree of superheat of the hot cell bottom and the Rayleigh number. The increased buoyancy provided by the bubbles leads to more energetic hot plumes detaching from the hot cell bottom and, as a consequence, the strength*

*Submitted to *Proceedings of National Academy of Sciences, The USA* as : R. Lakkaraju, R. J. A. M. Stevens, P. Oresta, R. Verzicco, D. Lohse, and A. Prosperetti, 'Heat transport in boiling turbulent Rayleigh-Bénard convection'.

of the circulation in the cell is significantly increased. Our results are in general agreement with recent experimental results of Zhong et al., Phys. Rev. Lett. **102***, 124501 (2009) for boiling Rayleigh-Bénard convection.*

3.1 Introduction

The greatly enhanced heat transfer brought about by the boiling process is believed to be due to several interacting components, see, e.g., [1–3]. With their growth the bubbles cause a micro-convective motion on the heating surface and, as they detach by buoyancy, the volume they vacate tends to be replaced by cooler liquid. Especially in subcooled conditions, the liquid in the relatively stagnant microlayer under the bubbles can evaporate and condense on the cooler bubble top. This process provides for the direct transport of latent heat, which is thus able to bypass the low-velocity liquid region adjacent to the heated surface due by the no-slip condition. The bubble growth process itself requires latent heat and, therefore, also removes heat from the heated surface and the neighboring hot liquid. Finally, with their buoyancy, the bubbles enhance the convective motion in the liquid beyond the level caused by the well-known single-phase Rayleigh-Bénard convection mechanisms, see e.g., [1–3]. This is the aspect on which we focus in the present chapter.

In classical single-phase Rayleigh-Bénard (RB) convection, the dimensionless heat transport, Nu, the Nusselt number, is defined as the ratio of the total heat transported through the cell to the heat that would be transported by pure conduction with a quiescent fluid. This ratio increases well above 1 as the Rayleigh number $Ra = \frac{g\beta\Delta L^3}{\nu\kappa}$ is increased due to the onset of circulatory motion in the cell. Here g is the acceleration of gravity, β the isobaric thermal expansion coefficient, $\Delta = T_h - T_c$ the difference between the temperature T_h of the hot bottom plate and the temperature T_c of the cold top plate, L the height of the cell, ν the kinematic viscosity and κ the thermal diffusivity. Further, Nu depends on the shape of the cell, its aspect ratio (defined for a cylindrical cell of diameter D as $\Gamma = D/L$) and the Prandtl number $Pr = \nu/\kappa$ of the liquid. For Ra in the range $10^7 - 10^{10}$ and Pr in the range $0.7 - 7$, the heat transport satisfies an approximate scaling relation $Nu \propto Ra^{0.29-0.32}$ [4, 5].

How is this scaling modified if the hot plate temperature T_h is above the fluid saturation temperature T_{sat}, so that bubbles can be generated? In the present chapter, we address this question by carrying out numerical simulations in the range $2 \times 10^6 \leq Ra \leq 5 \times 10^9$ for a cylindrical cell with aspect ratio $\Gamma = 1$ for $Pr = 1.75$, which is appropriate for water at 100 ^{o}C under normal conditions.

The extensive literature on boiling leads to the expectation that the appearance of bubbles would cause a substantial increase in Nu with respect to single-phase con-

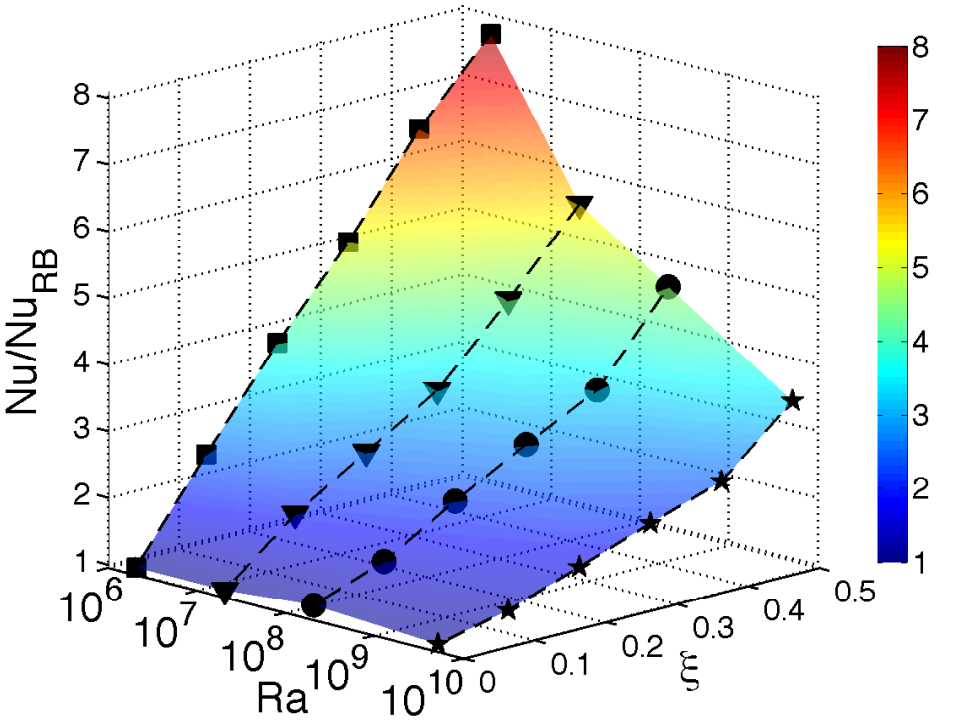

Figure 3.1: $Nu(Ra,\xi)$ for boiling convection normalized by the corresponding single-phase value Nu_{RB} for $N_b = 50000$ bubbles. Here ξ is the normalized superheat, $\xi \equiv (T_h - T_{sat})/\Delta$. The symbols correspond to $Ra = 2\times10^6$ (square), 2×10^7 (triangles), $Ra = 2\times10^8$ (circles) and 5×10^9 (stars).

vection, see e.g., Ref. [1]. For RB convection, the effect of phase change has recently been studied in Ref. [6] for the case of ethane near the critical point, and indeed major heat transport has been found.

3.2 Preliminaries

The present work builds on the previous work of Ref. [7] to which the reader is refereed for a detailed description of the mathematical model and numerical method. Briefly, the bubbles are considered point sources of momentum and heat for the liquid treated in the Boussinesq approximation and they are tracked in a Lagrangian way. In addition to buoyancy, their motion is influenced by drag, added mass, and lift. The heat exchanged with the liquid is modeled by means of a heat transfer coef-

ficient and their surface temperature is assumed to remain at the saturation value.

Bubbles are introduced at random positions on the bottom plate with an initial diameter of 38 μm and are removed upon reaching the top plate. As shown in Ref. [8], the initial bubble size is immaterial provided it is in the range of a few tens of microns. In view of their smallness, the latent heat necessary for their generation is very small and is neglected. When a bubble is removed, a new bubble is randomly generated at the bottom plate in such a way that the total number of bubbles N_b remains constant in the course of the simulation. We consider three values for this quantity, $N_b = 10000$, 50000, and 150000. Another parameter we vary is the degree of superheat, $T_h - T_{sat}$, which we express in the dimensionless form $\xi = (T_h - T_{sat})/\Delta$.

The Nusselt number shown in the following is defined as a $Nu = q_h^{''} L/(k\Delta)$, where k is the liquid thermal conductivity and $q_h^{''}$ is the heat flux into the bottom plate. This quantity differs from $q_c^{''}$, the heat flux at the upper plate, due to the removal of the bubbles that reach the top boundary[†].

An important new parameter introduced by the bubbles is the Jakob number $Ja = \frac{\rho c_p (T_h - T_{sat})}{\rho_v h_{fg}} = \xi \frac{\rho c_p \Delta}{\rho_v h_{fg}}$, where ρ and ρ_v are the densities of liquid and vapor, c_p is the liquid specific heat, and h_{fg} is the latent heat for vaporization. Physically, Ja expresses the balance between the available thermal energy and the energy required for vaporization. With $\Delta = 1\ ^o$C, Ja varies between 0 and 1.68 as ξ varies between 0 and 1/2. For $\xi = 0$, the bubbles introduced at the hot plate can only encounter liquid at saturation temperature or colder, and therefore they cannot grow but will mostly collapse. On the other hand, for $\xi = 1/2$, they have significant potential for growth.

To give an impression of the physical situation corresponding to our parameter choices, we may mention that 100 ^{o}C water in a 15 cm-high cylinder with an imposed temperature difference $\Delta = 1\ ^o$C would correspond to $Ra \simeq 5 \times 10^8$. The Kolmogorov length scale based on the volume- and time-averaged kinetic energy dissipation in single-phase RB convection is 3 mm for $Ra \sim 10^6$ and 0.5 mm for $Ra \sim 10^{10}$, see e.g., Ref. [5], and is therefore always much larger than the initial size of the injected bubbles (i.e., $0.5 \times 10^{-3}/(38 \times 10^{-6}) \approx 13$ times larger for the highest Rayleigh number).

Simulations are carried out on computational grids with the angular, radial, and axial directions discretized by means of $193 \times 49 \times 129$, $385 \times 129 \times 257$, $385 \times 129 \times 257$, and $769 \times 193 \times 385$ nodes for $Ra = 2 \times 10^6$, 2×10^7, 2×10^8, and 5×10^9. The simulations are therefore well resolved according to the requirements specified in Ref. [9]. We have also checked the global balances of appendix B in Ref. [7] finding that they were satisfied to within 0.1%.

[†]The Nusselt number shown in our previous works [7, 8, 11] are based on the average between $q_h^{''}$ and $q_c^{''}$.

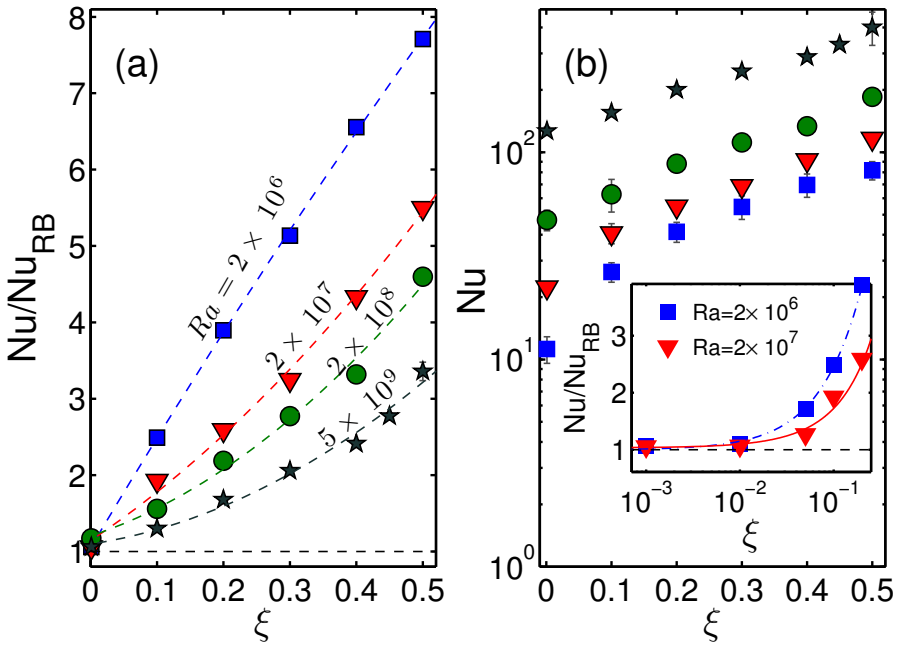

Figure 3.2: Nu/Nu_{RB} (left) and Nu (right) as functions of the normalized superheat ξ for 50000 bubbles. The symbols correspond to $Ra = 2 \times 10^6$ (squares), $Ra = 2 \times 10^7$ (triangles), $Ra = 2 \times 10^8$ (circles) and $Ra = 5 \times 10^9$ (stars). The inset shows a detail for small superheat ξ for $Ra = 2 \times 10^6$ (blue squares) and $Ra = 2 \times 10^7$ (red triangles) with quadratic fits to the data.

3.3 Observations on heat transport

In Figure 3.1, the dependence of Nu on the Rayleigh number Ra and the dimensionless superheat ξ is shown for $N_b = 50000$ bubbles. Here Nu is normalized by Nu_{RB}, the single-phase Nusselt number corresponding to the same value of Ra. Each symbol shows the result of a separate simulation carried out for the corresponding values of Ra and ξ. A colored surface is interpolated through the computed results with the color red corresponding to $Nu/Nu_{RB} = 8$ and the color blue $Nu/Nu_{RB} = 1$.

The same data are shown on a two-dimensional plot of Nu/Nu_{RB} vs. ξ in Figure 3.2a for four different Rayleigh numbers in descending order; here the dashed lines are drawn as guides to the eye. It is evident that the *relative* enhancement of the heat transport is a decreasing function Ra. This statement, however, does not apply to the *absolute* heat transport shown in Figure 3.2b, where Nu is not normalized by the single-phase value. Here Ra increases in ascending order, which shows that the

bubbles always have a beneficial effect on the heat transport. For very small superheat the heat transport approaches the single-phase value as shown in the inset of Figure 3.2b.

Figures 3.1 and 3.2 show results calculated keeping the bubble number fixed. This procedure, therefore, does not faithfully reflect physical reality as it is well known that the number of bubbles is an increasing function of superheat. The dependence is actually quite strong, with the number of bubbles proportional to $T_h - T_{sat}$ raised to a power between 3 and 4 [1]. However, varying independently N_b and ξ permits us to investigate separately the effect of these quantities.

The effect of changing the bubble number from 50000 to 150000 at the same ξ is shown in Figures 3.3a and 3.3b for $Ra = 2 \times 10^7$ and 5×10^9, respectively. In the latter case we also include results for $N_b = 10000$. For small ξ the heat transfer enhancement is small as the bubbles will mostly encounter colder liquid, condense and add very little to the system buoyancy. As the superheat ξ increases, however, the effect of the bubbles become stronger and stronger, and larger the larger their number.

In Figure 3.3b, the solid symbols are the data of Ref. [6] taken at a significantly higher Rayleigh number $Ra \approx 3 \times 10^{10}$ [‡]. The inset in the figure shows our computed results and the experimental data for $\xi \leq 0.3$. Quadratic interpolation using our results for the three values of N_b suggests that, in order to match the experimental values, we would need $N_b \simeq 63000$ for $\xi = 0.2$ and $N_b \simeq 250000$ for $\xi = 0.3$. If, as suggested by experiment, the actual physical process results in a relation of the form $N_b \propto \xi^m$, we find $m \simeq 3.4$ which falls in the experimental range $3 < m < 4$ mentioned before. With this value of m, we can estimate the number of bubbles necessary to account for the measured Nu at $\xi = 0.1$. Using $N_b(\xi = 0.1) = (0.1/\xi)^m N_b(\xi)$ we find $N_b(0.1) \approx 5968$ for $\xi = 0.2$ and $N_b(0.1) \approx 6000$ for $\xi = 0.3$. These values are in agreement and consistent with the fact that our computed result at $N_b = 10000$ is somewhat higher than the measured value for $\xi = 0.1$. The picture that emerges from these considerations is therefore in reasonable agreement with experiment. A similar exercise cannot be carried out for larger values of ξ as in the experiment bubbles then become so large that they coalesce and form slugs with non negligible dimensions. Our model is clearly inapplicable to deal with this situation.

The heat transport in single-phase RB convection can be approximated by an effective scaling law $Nu = A_0 Ra^{\gamma_0}$. In the present Ra range the experimental data are well represented with the choices $\gamma_0 = 0.31$ and $A_0 \simeq 0.120$. How does the effective scaling law change for boiling convection? Figure 3.4a shows the Nusselt number vs.

[‡]This work reports data for both increasing and decreasing superheat. We show here only the latter data because, for increasing superheat, there is a threshold for fully developed boiling conditions which pushes the onset of bubble appearance beyond $\xi = 0.35$. For decreasing ξ on the other hand fully developed boiling conditions prevail all the way to small values of ξ

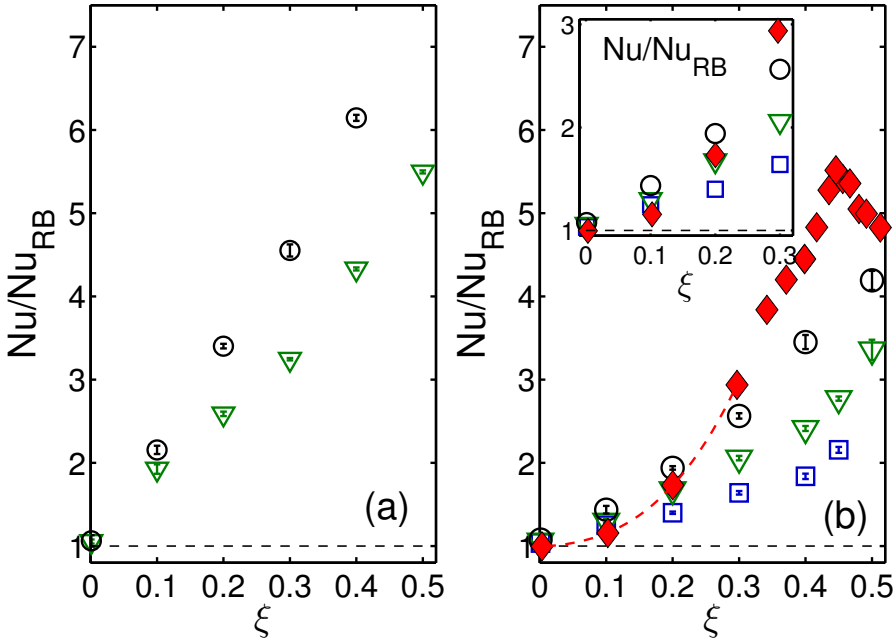

Figure 3.3: Nu/Nu_{RB} vs. ξ for three different bubble numbers, $N_b = 10000$ (squares), 50000 (triangles) and 150000 (circles); the left panel is for $Ra = 2 \times 10^7$ and the right panel for $Ra = 5 \times 10^9$. The red-dashed line is a fit to the experimental data of Zhong et al. [6] shown by the filled symbols. The inset is a blow-up for the range $0 \leq \xi \leq 0.30$.

Rayleigh number for different values of ξ for $N_b = 50000$ bubbles. The two solid lines have slopes $1/3$ and $1/5$, while the dashed line shows the single-phase values. If we fit Nu for the boiling case again with an effective scaling law $Nu = A(\xi)Ra^{\gamma(\xi)}$, we obtain the effective exponents $\gamma(\xi)$ shown in the inset of the figure (as blue squares). Of course, $\gamma(\xi = 0) = \gamma_0$ and, as ξ increases, $\gamma(\xi)$ decreases to a value close to 0.20. In the range $0 \leq \xi \leq 0.5$ the numerical results for $A(\xi)$ are well represented by $A(\xi)/A_0 = 1 + 66.31\,\xi$, which monotonically increases from 1 to 33.15 for $\xi = 0.5$. How strongly do the pre-factor $A(\xi)$ and the effective scaling exponent $\gamma(\xi)$ depend on N_b? In the inset of the same figure, we show $\gamma(\xi)$ for $N_b = 150000$ bubbles (see red-circles), in order to compare with the $N_b = 50000$ case. The functional dependence $\gamma(\xi)$ is very close for the two cases. Further, we find $A(\xi)/A_0 = 1 + 83.54\,\xi$ for 150000 bubbles, i.e., a stronger ξ dependence as compared to the $N_b = 50000$ case, reflecting the enhanced number of bubbles.

It is tempting to regard the increased heat transport as due to the additional buoy-

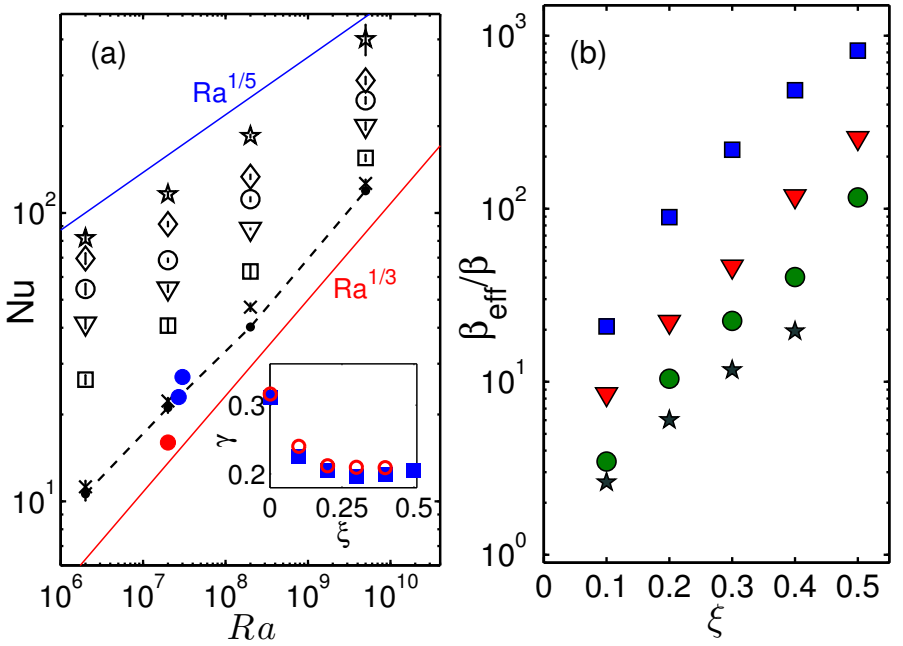

Figure 3.4: (a) Nu vs. Ra and (b) β_{eff}/β vs. ξ for 50000 bubbles. In (a), the numerical results are shown as crosses ($\xi = 10^{-3}$), squares ($\xi = 0.1$), triangles ($\xi = 0.2$), circles ($\xi = 0.3$), diamonds ($\xi = 0.4$) and stars ($\xi = 0.5$). Simulations without bubbles are also shown for comparison as a dashed line joining small dots and data from the LB simulations of Ref. [12] as filled circles, red for no-boiling and blue for boiling In the inset, the effective scaling exponent $\gamma(\xi)$ obtained from power-law fits of the form $Nu \propto Ra^{\gamma}$ is shown as a function of ξ for 50000 (blue squares) and 150000 (red circles) bubbles. In (b), the effective buoyancy has been computed from Eq. (1). The symbols are the same as in Figure 3.2a.

ancy provided by the bubbles. In this view, the Rayleigh number should be based on an effective buoyancy β_{eff} in place of the pure liquid buoyancy β. An expression for β_{eff} can then be found by equating $A(\xi)Ra^{\gamma(\xi)}$ to $A_0\left[(\beta_{eff}/\beta)Ra\right]^{\gamma_0}$ with the result

$$\frac{\beta_{eff}}{\beta} = \left[\frac{A(\xi)}{A_0}\right]^{\frac{1}{\gamma_0}} Ra^{\frac{\gamma(\xi)}{\gamma_0}-1}. \tag{3.1}$$

The quantity β_{eff}/β as given by this relation is shown in Figure 3.4b as function of ξ and Ra for $N_b = 50000$. For the same ξ, β_{eff} decreases as Ra increases as expected on the basis of Figures 3.1 and 3.2. For fixed Ra, β_{eff}/β increases with ξ, also as expected. It is quite striking that β_{eff} can exceed β by nearly 3 orders of magnitude

for $\xi = 0.5$ and small Rayleigh number. Note that one cannot directly compare the numerical values for β_{eff}/β shown in figure 3.4b with an experiment in which ξ is increased in a given cell, as in our plot $N_b = 50000$ is fixed, whereas in the experiment $N_b \sim \xi^m$ with $m \simeq 3.4$ as discussed above.

A recent Lattice-Boltzmann (LB) simulation of finite-size bubbles also found heat transport enhancement [12]. The results of this study for $Ra \sim 10^7$ are shown by filled circles in Figure 3.4a. The heat transfer enhancements achieved are much smaller than ours, most likely due to the significantly smaller number of bubbles (only a few hundreds), as well as other differences (the values of Ja, Pr etc.) of lesser importance.

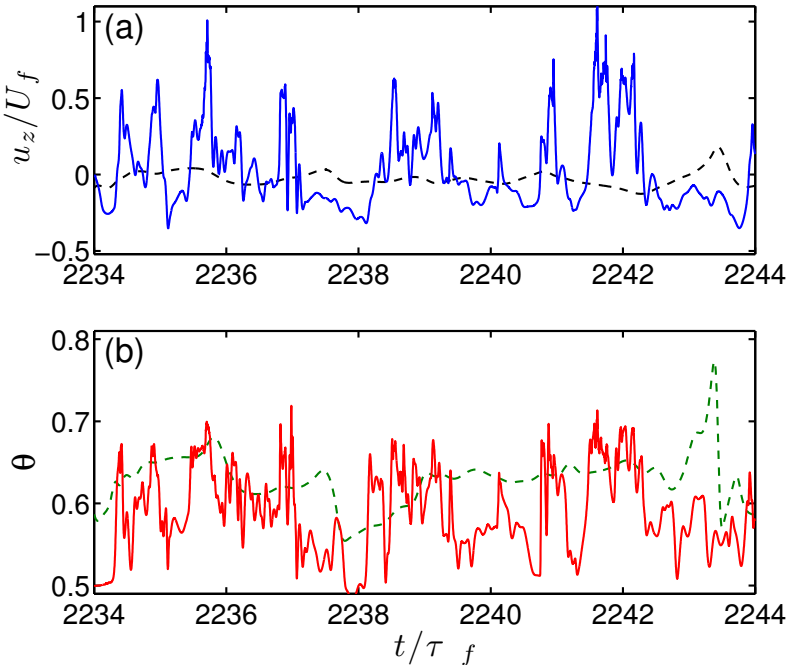

Figure 3.5: The solid lines show the dimensionless vertical velocity u_z/U_f (top panel) and temperature θ (bottom panel) as functions of dimensionless time in the hot liquid at a height $z/L = 0.02$ near the axis. The dashed lines show similar results for simulations without bubbles; here $Ra = 2 \times 10^8$, $N_b = 150000$ and $\xi = 0.3$.

3.4 Flow organization

We now come to the local flow organization. As well known the boundary layers formed on the bottom (and top) plate are marginally stable and occasional intermit-

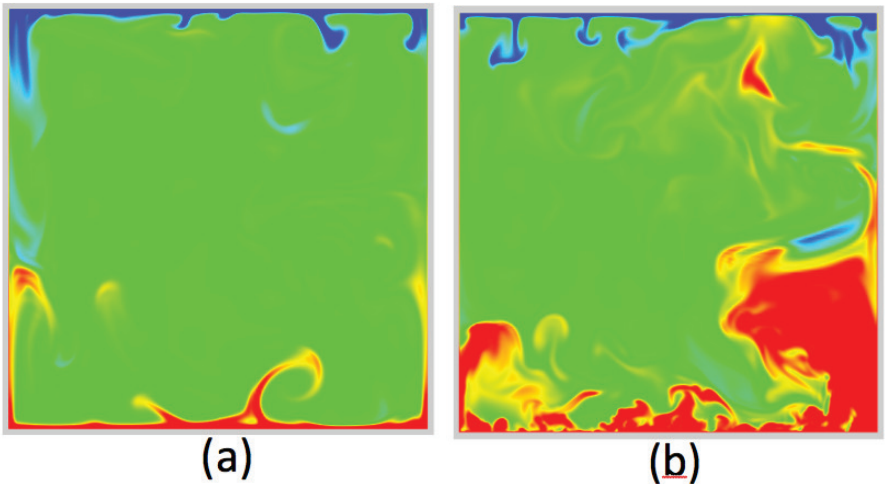

Figure 3.6: Instantaneous dimensionless temperature field in a vertical plane through the cell axis for convection without bubbles (left) and with bubbles (right). The color varies from red for $\theta = 0.7$ to blue for $\theta = 0.3$; here $Ra = 2 \times 10^8$, $N_b = 150000$ and $\xi = 0.3$.

tent eruptions of hot (or cold) liquid occur at their edges. Vapor bubbles subject these boundary layers to intense fluctuations which enhance the convective effects. As an example, Figure 3.5 shows sample time records of the dimensionless vertical velocity u_z/U_f (top panel), and temperature $\theta = (T - T_c)/\Delta$ (bottom panel) vs. normalized time t/τ_f near the axis at $z/L = 0.02$, i.e., just outside the hot thermal boundary layer. The velocity scale U_f is defined by $U_f = \sqrt{g\beta\Delta L}$ and $\tau_f = L/U_f$. The dashed lines are results for the single-phase case. The immediate observation is that the small-scale fluctuations are much stronger in the two-phase case. As expected, the positive and negative velocity fluctuations are correlated with warm and cold temperature fluctuations, respectively.

To give an impression of the difference brought about by the presence of bubbles on the convective motions in the cell, we show in Figure 3.6 snapshots of the dimensionless temperature in a vertical plane through the axis of the cell for $Ra = 2 \times 10^8$ in the single-phase (a) and two-phase (b) cases, the latter for $\xi = 0.3$ and $N_b = 150000$. We notice that bubbles considerably thicken the layer of hot fluid near the base and make it more energetic compared to the single-phase situation. Chunks of hot liquid can be seen all the way up near the cold plate, presumably caused by the latent heat deposited by condensing bubbles in the bulk liquid. The up-down symmetry of the single-phase case that can be seen in the left panel is markedly absent in the

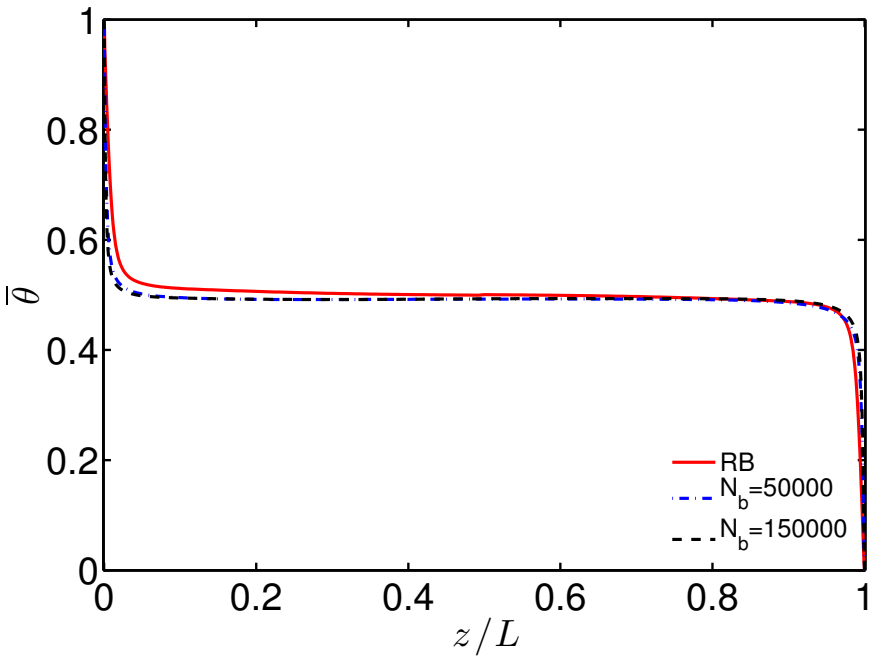

Figure 3.7: Normalized temperature $\overline{\theta}$ vs. z/L over the entire cell height. Here $\xi = 0.5$, $Ra = 2 \times 10^8$ and RB (continuous red), $N_b = 50000$ (dash-dot blue), and 150000 (dash black).

two-phase case because of the tendentially upward motion of the bubbles which condense on encountering liquid colder than T_{sat}. This mechanism is evidently quite different from the symmetry-breaking process observed in non-Boussinesq systems which is due to the temperature dependence of viscosity, see e.g., Ref. [13].

Figure 3.7 shows the time and area-averaged mean temperature in the cell as a function of height. The red line is the single-phase case, while the dashed line is for the two-phase cases with $\xi = 1/2$; the results for the different bubble numbers superpose within the resolution of this figure. For both cases the dimensionless bulk mean temperature is close to 0.5, i.e., $T \simeq T_m = (T_h + T_c)/2 = T_{sat}$. A close inspection of the figure shows that this tendency is enhanced in the two-phase case because the bubble surface temperature is fixed at the same value T_{sat}. It may be expected that, in this situation, not many bubbles will grow or condense in the bulk and only condense once they reach the neighborhood of the top plate. The figure also shows that, in the two-phase case, the boundary layers near the top and bottom plates are not symmetric. This feature can be seen more clearly in Figure 3.8 where details of the mean temperature near the upper and lower plates are shown. The lack of

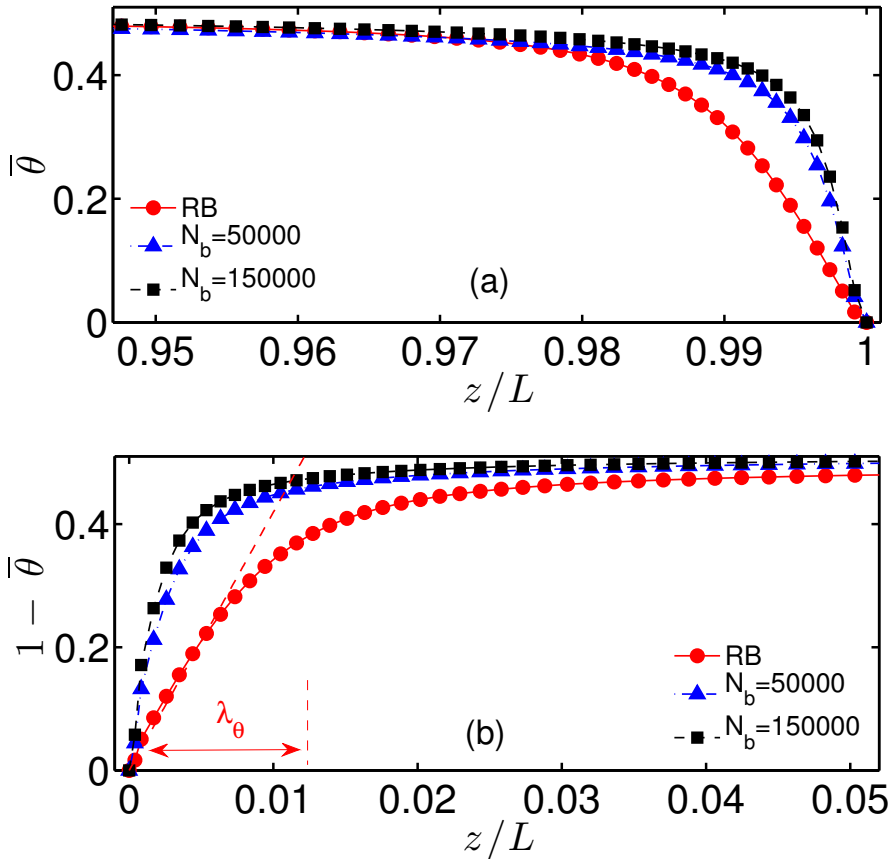

Figure 3.8: (a) $\overline{\theta}$ vs. z/L near cold plate, and (b) $1-\overline{\theta}$ vs. z/L near hot plate. Symbols are red circles (RB), blue triangles (N_b =50000) and black squares (N_b =150000). Boundary layer thickness λ_θ based on the wall gradient is also indicated in (b) for single-phase convection. Here $\xi = 0.5$ and $Ra = 2 \times 10^8$.

symmetry between the two is more evident here together with the thinning of the boundary layers with increasing numbers of bubbles. This latter result is a clear manifestation of the enhanced convective circulation inside the cell promoted by increasing the number of bubbles.

For the hot plate, one can define the thermal boundary layer thickness as $\lambda_\theta = (T_m - T_h)/[dT/dz]_{z=0}$ where $[dT/dz]_{z=0}$ is the mean temperature gradient at the hot plate. Replotting the data of the bottom panel in Figure 3.8 as functions of z/λ_θ, we find the results shown in Figure 3.9. The three sets of data now collapse on a single line in the range $0 \leq z/\lambda_\theta \leq 0.5$. The small differences farther away from the wall

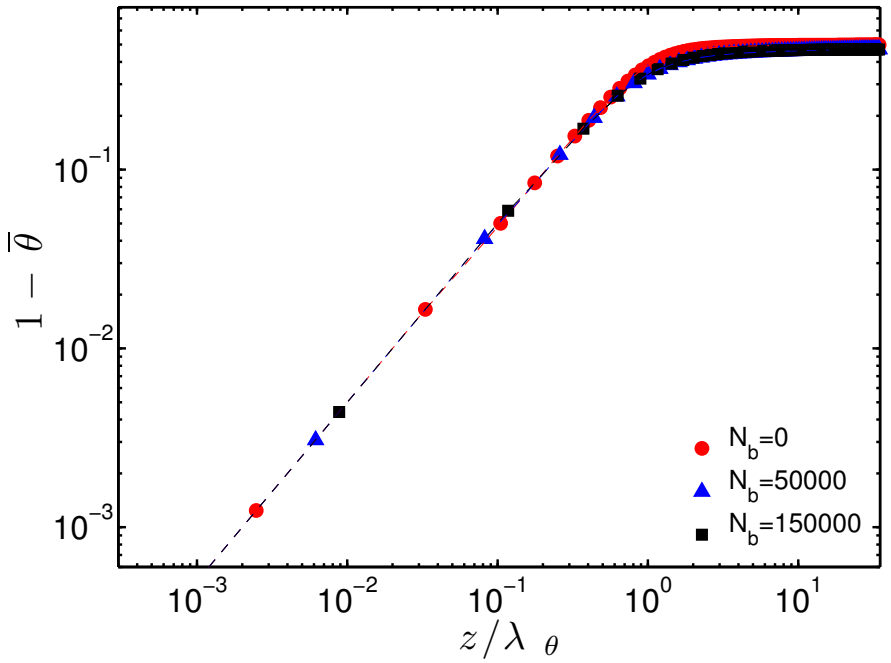

Figure 3.9: Normalized mean temperature $1-\overline{\theta}$ vs. z/λ_θ in the hot thermal boundary layer. Here $\xi = 0.5$, $Ra = 2 \times 10^8$ and $N_b = 0$ (red circles), 50000 (blue triangles) and 150000(black squares).

reflect differences in the shape factor of the boundary layers.

3.5 Summary and Conclusions

In summary, our investigation of a simple model of Rayleigh-Bénard convection with boiling has demonstrated the effect of the degree of superheat and of the bubble number on heat transport. Comparison with existing data suggests a basic conformity of our results with some physical features of a real systems. Vapor bubbles significantly enhance the heat transport primarily by increasing the strength of the circulatory motion in the cell. The velocity and thermal fluctuations of the boundary layers are increased and, by releasing their latent heat upon condensation in the bulk fluid, the bubbles also act as direct carriers of energy. We have shown that the heat transfer enhancement can be interpreted in terms of an enhanced buoyancy which is shown in Eq. (1) and Figure 3.4b. The relative effect of the bubbles diminishes as Ra increases.

References

[1] V. K. Dhir, *Boiling heat transfer*, Annu. Rev. Fluid Mech. **30**, 365 (1998).

[2] V. P. Carey (1992), *Liquid-vapor phase-change phenomena*, (Hemisphere, New York, United States).

[3] John H. Lienhard IV, and John H. Lienhard V *A Heat Transfer Textbook*, (Dover Publications, New York, United States).

[4] G. Ahlers, S. Grossmann, and D. Lohse, *Heat transfer and large scale dynamics in turbulent Rayleigh-Bénard convection*, Rev. Mod. Phys. **81**, 503 (2009).

[5] D. Lohse and K. Q. Xia, *Small-scale properties of turbulent Rayleigh-Bénard convection*, Ann. Rev. Fluid Mech. **42**, 335 (2010).

[6] J. Q. Zhong, D. Funfschilling, and G. Ahlers, *Enhanced heat transport by turbulent two-phase Rayleigh-Bénard convection*, Phys. Rev. Lett. **102**, 124501 (2009).

[7] P. Oresta, R. Verzicco, D. Lohse, and A. Prosperetti, *Heat transfer mechanisms in bubbly Rayleigh-Bénard convection*, Phys. Rev. E **80**, 026304 (2009).

[8] R. Lakkaraju, L. E. Schmidt, P. Oresta, F. Toschi, R. Verzicco, D. Lohse, and A. Prosperetti, *Effect of vapor bubbles on velocity fluctuations and dissipation rates in bubbly Rayleigh-Bénard convection*, Phys. Rev. E **84**, 036312 (2011).

[9] R. J. A. M. Stevens, R. Verzicco, and D. Lohse, *Radial boundary layer structure and Nusselt number in Rayleigh-Bénard convection*, J. Fluid Mech. **643**, 495 (2010).

[10] R. Verzicco and R. Camussi, *Numerical experiments on strongly turbulent thermal convection in a slender cylindrical cell*, J. Fluid Mech. **477**, 19 (2003).

[11] L. E. Schmidt, P. Oresta, F. Toschi, R. Verzicco, D. Lohse, and A. Prosperetti, *Modification of turbulence in Rayleigh-Bénard convection by phase change*, New Journal of Physics **13**, 025002 (2011).

[12] L. Biferale, P. Perlekar, M. Sbragaglia, and F. Toschi, *Convection in multiphase fluid flows using lattice boltzmann methods*, Phys. Rev. Lett. **108**, 104502 (2012).

[13] G. Ahlers, E. Brown, F. F. Araujo, D. Funfschilling, S. Grossmann, and D. Lohse, *Non-Oberbeck-Boussinesq effects in strongly turbulent Rayleigh-Bénard convection*, J. Fluid Mech. **569**, 409-445 (2006).

4

TEMPERATURE INTERMITTENCY IN BOILING CONVECTION *

Temperature fluctuations in two-phase boiling turbulent Rayleigh-Bénard (RB) convection are studied for water at 100 ^{o}C at normal pressures through direct numerical simulations. We find that the well-known front-like structures in the temperature field are smoothen by the vapor bubbles in the flow, leading to considerably less intermittency in the boiling case as compared to the standard RB case.

4.1 Introduction

In turbulence and in other non-equilibrium systems relatively calm periods can be interrupted by rare and sudden changes. The probability density functions (PDFs) of such intermittent quantities are correspondingly non-Gaussian [1, 2]. The scale information is typically studied with the help of n-th order structure functions, e.g., $S_n(\mathbf{r}) = \langle \mid \delta\mathbf{u}(\mathbf{r}) \mid^n \rangle$ for the velocity structure function, where $\delta\mathbf{u}(\mathbf{r})$ is the velocity increment measured between two points $\mathbf{x}$ and $\mathbf{x}+\mathbf{r}$.

For very large Reynolds number, scaling $S_n(r) \propto r^{\zeta_n^u}$ can be assumed, reflecting the

*Manuscript to be submitted as R. Lakkaraju, F. Toschi and D. Lohse, 'Temperature intermittency in boiling convection'.

self-similarity of the velocity field [3]. In the inertial range energy conservation implies $S_3(r) \propto r$, i.e., $\zeta_3^u = 1$. The deviations $\delta\zeta_n^u = \zeta_n^u - \frac{n}{3}$ from the K41 estimate $\zeta_n^u = n/3$ are called intermittency corrections [2, 4, 5]. Similarly, also the structure functions of a passive scalar $T(\mathbf{x},t)$, namely $R_n(r) = \langle \mid \delta T(r) \mid^n \rangle = \langle \mid T(\mathbf{x}+r) - T(\mathbf{x}) \mid^n \rangle \sim r^{\zeta_n^\theta}$, show intermittency corrections $\delta\zeta_n^\theta = \zeta_n^\theta - \frac{n}{3}$, i.e., deviations from the dimensional estimate $\zeta_n^\theta = n/3$. It is known that the intermittency corrections for the temperature field are in fact much larger than that for the velocity field, $\mid \delta\zeta_n^\theta \mid \geq \mid \delta\zeta_n^u \mid$ [6]. Usually, temperature fronts (or sudden eruptions) occur at the separatrix which demarcates the warm and cold fluid zones in the regions of the flow formed by the large-scale structures. These fronts become sharper with an increase in flow Reynolds number and so does the small-scale intermittency [7–12]. In addition to this small-scale intermittency, the presence of the mean gradients of the scalar field causes strong discontinuities at the large-scales.

In Rayleigh-Bénard (RB) convection [3, 13], the temperature is strictly speaking not a passive scalar as the flow is thermally driven. However, in the bulk of the flow where the Bolgiano length l_B is comparable to the system size, it basically behaves like a passive scalar [3]. The velocity and temperature structure functions correspondingly behave closer to the Obukhov-Corrsin estimate (see Refs. [14, 15]), but with intermittency corrections [18–21]. The aim of this work is to find out how these intermittency corrections change once the RB system is boiling, i.e., a significant number of vapor bubbles gets nucleated.

4.2 Simulation details

We perform numerical simulations in a unit aspect ratio cylindrical RB convection under Boussinesq approximations augmented with point-like two-way coupled vapor bubbles, see Refs. [22–26] for the detailed equations, methods, and initial conditions. Briefly, the bubbles are at the saturation condition with a temperature $T_{sat} = \frac{1}{2}(T_h + T_c) = T_m$, i.e, the mean fluid temperature, where T_h and T_c are the temperatures at the hot bottom and the cold top, respectively. In these simulations, the bubbles can grow or shrink by exchanging latent heat (h_{fg}) with the surrounding fluid. The change in size of a bubble directly affects the mechanical and the thermal forcings on the flow [†]. Generally, these bubbles are big in size in the hot boundary layers, and are relatively small in the cold layers. Near the mid-plane their size is almost constant. The bubble size dynamics are controlled by the ratio of the sensible heat to the latent heat known as the Jakob number $Ja = \rho c_p (T_h - T_{sat})/(\rho_v h_{fg})$ [22], where ρ

[†] If a bubble encounters a cold current in its journey then it immediately condenses by releasing heat at that location and thus affects the temperature field.

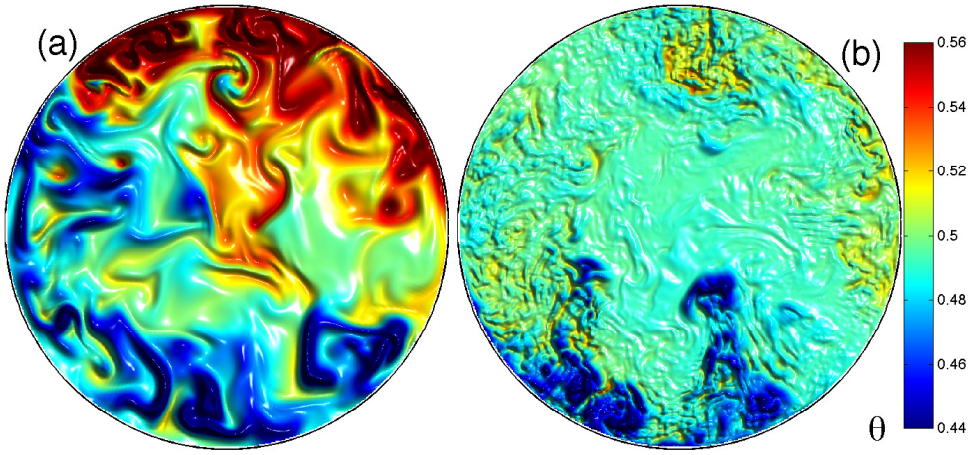

Figure 4.1: Snapshots of dimensionless temperature θ at mid-height plane for (a) RB convection, and (b) boiling convection. In boiling simulations, 50000 saturated vapor bubbles are used. The Rayleigh number $Ra = 2 \times 10^8$ is fixed in both simulations. The temperature scale ranges from 0.44 (blue) to 0.56 (red) with the mean temperature at $\theta = 0.5$.

is the liquid density, c_p the liquid specific heat, and ρ_v the vapor density. In our simulations, water at mean temperature T_m =100 ^{o}C at a normal pressure is considered with a temperature difference $\Delta \equiv T_h - T_c = 1$ K applied between the plates in a 11 cm high (equal to diameter) cylinder. At the hot bottom plate, bubbles of 38 microns diameter are injected, see Ref. [26] for other details. These conditions correspond to a Rayleigh number of Ra= $\frac{g\beta\Delta L^3}{\nu\kappa} \approx 2 \times 10^8$, the Prandtl number $Pr = \frac{\nu}{\kappa} = 1.75$, and $Ja = 1.5$. Here, g is the gravitational acceleration, β the isobaric thermal expansion coefficient, ν the kinematic viscosity, and κ the thermal diffusivity. As we mentioned in our earlier work [25] results are insensitive to the bubble injection size as the nuclei are small enough. We vary the number of bubbles N_b in the simulations, and determine their effect on the small scales.

In Table 4.1, we show simulation details of standard RB convection and of boiling convection. These simulations are performed on a computational grid which consists of $385 \times 129 \times 257$ points in the azimuthal, radial, and the axial directions, respectively. The simulations are well resolved on these grids. Other details can be found in Ref. [26]. The total bubble volume fractions involved in the simulations are smaller than 0.01% (see the column 2) and hence the point-particle approximation [27] for this very dilute flow is reasonable. In our simulations the dimensionless temperature $\theta = (T - T_c)/(T_h - T_c)$ is used such that the hot bottom is at '1', and the

Table 4.1: Simulations details: Fixed parameters are $Ra = 2 \times 10^8$, and $Pr = 1.75$. Column 1 for number of vapor bubbles (N_b) and column 2 for total void fraction (ϕ). Columns 3, 4, 5, and 6 are time and volume-averaged rms velocity $\overline{u}_{rms}$, rms temperature $\overline{\theta}_{rms}$, kinetic energy dissipation $\overline{\varepsilon}_u$, and the thermal energy dissipation $\overline{\varepsilon}_\theta$, respectively. Last column shows simulation time in free-fall times $\tau_f (= L/U_f)$ after discarding the initial transients of first 140 free-fall times in the case of single-phase, and 45 free-fall times in the case of boiling convection.

Simulation	$\phi \times 10^3$	$\frac{\overline{u}_{rms}}{U_f}$	$\overline{\theta}_{rms}$	$\frac{\overline{\varepsilon}_u}{U_f^3/L}$	$\frac{\overline{\varepsilon}_\theta}{U_f \Delta^2/L}$	τ_f
RBC	–	0.0925	0.0416	0.0020	0.0019	1700
N_b=10000	0.1330	0.3314	0.0326	0.0381	0.0027	250
N_b=50000	0.3365	0.7631	0.0269	0.2364	0.0037	230
N_b=150000	0.7231	0.9747	0.0222	0.5587	0.0043	180

cold top is at '0'. The velocities are expressed in free-fall velocities $U_f = \sqrt{g\beta\Delta L}$. In columns 3 and 4, the volume averaged rms velocity and rms temperature are shown. With the presence of vapor bubbles, more vigorous fluctuations in the velocity field and a more homogeneous temperature field can be observed. The key quantities in convective turbulence are the kinetic energy dissipation $\varepsilon_u = \nu \mid \nabla \mathbf{u} \mid^2$ and the thermal energy dissipation $\varepsilon_\theta = \kappa \mid \nabla \theta \mid^2$, see e.g., Ref. [13]. In columns 5 and 6, time and volume-averaged energy dissipations are shown. The dissipations in the cylinder increase drastically, and indicates that the total thermal energy transported increases in between the plates [‡]. It is remarkable that the very small void fraction of the vapor bubbles has a such big difference on the intensity of fluctuations in the system. Finally, in the last column we show the simulation time after discarding the initial transients.

4.3 Coherence in fields

In Figure 4.1, snapshots of the dimensionless temperature θ at the mid-height plane for the standard RB (a) and the boiling (b) convection are shown. The color coding is such that we can see the temperature field is close to the mean temperature of the fluid, i.e., $\theta = 1/2$. The presence of hot ($\theta > 0.5$) and cold ($\theta < 0.5$) temperature fronts

[‡]The total heat in the form of latent heat injected at the bottom plate is quite small due to the tiny volume fractions involved, but due to vigorous ejection of plumes heat transport in the system increases, see Ref. [26]

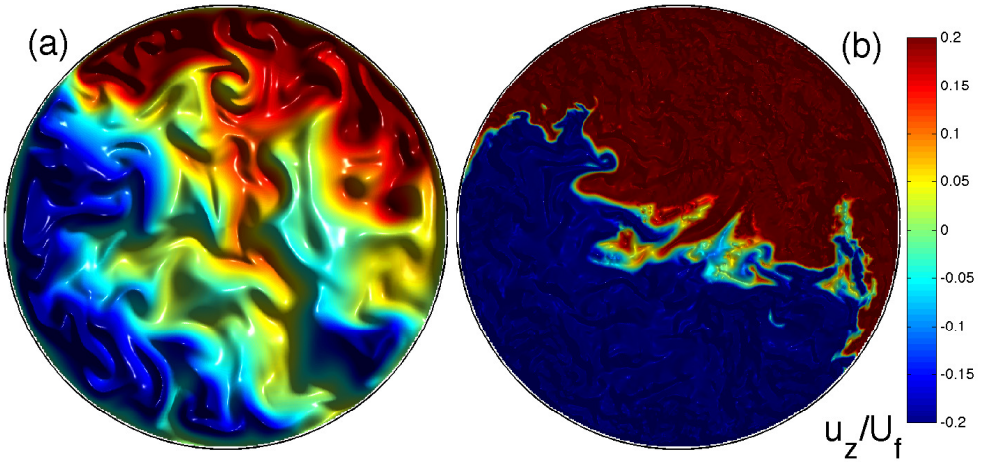

Figure 4.2: Snapshots of dimensionless vertical velocity u_z/U_f at the mid-height plane at the same times as 4.1, respectively. Left panel for RB convection and right panel boiling convection. Velocity scale ranges from -0.4 (blue) to 0.4 (red).

in RB convection and the vortex structures in the flow are clearly discernible near the sidewalls and also near the axis (see Panel a). Such sharp fronts are absent in case of boiling convection (see Panel b) and a relatively homogeneous field is observed. In Figure 4.2, the axial velocities on the mid-height plane are taken at the same time as of Figure 4.1. In general, the rising or falling motion of plumes in RB convection drives the large scale circulatory flow and hence the vertical velocity is maximum or minimum at the plume rise or fall locations, respectively, and are in coherence with the temperature field. In case of boiling convection, the circulatory motion is strengthened and can be observed as the increase in the vertical velocity of the flow, and the coherence is much less.

As mentioned earlier, the relevant length scales involved in the problem are the Kolmogorov length $\eta = (\nu^3/\overline{\varepsilon}_u)^{1/4}$ [§], the Bolgiano length $l_B = \left[\overline{\varepsilon}_u^5/\overline{\varepsilon}_\theta^3\right]^{1/4}(g\beta)^{-3/2}$, and the integral length l_{int}, see review [3]. In RB convection without bubbles for $Ra = 2\times10^8$, we find that the Kolmogorov length scale is $\eta \approx 0.004L$ and the Bolgiano length is $l_B \approx 0.046L$. These lengths are based on the time and volume-averaged energy dissipations in the cell and give us some estimate. Due to the random nature of the flow these lengths vary with space and time [3, 28, 29]. In our simulations, the integral scale is comparable to the system dimensions (approximately half diameter of the cylinder) and is nearly 7-8 times larger than l_B.

[§]For fluids with the Prandtl number near unity, the viscous and thermal lengths are nearly comparable with each other.

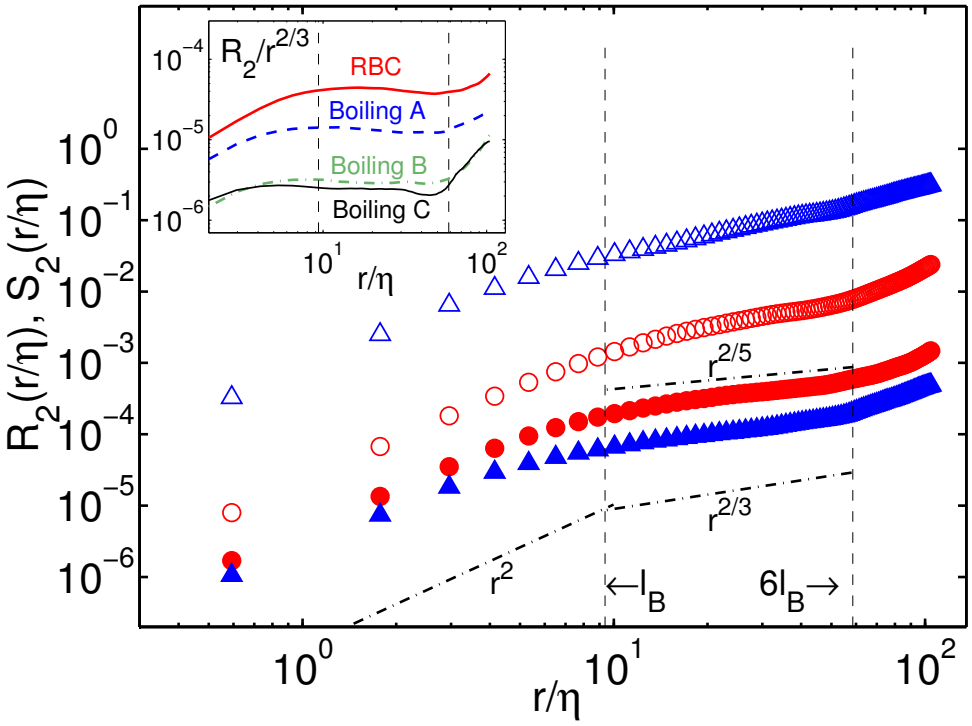

Figure 4.3: Second-order structure functions for temperature R_2 (solid symbols), and for vertical velocity S_2 (open symbols) at mid-height plane. Red circles for RB and blue triangles for boiling convection with 10000 bubbles. Dash-dot lines are to guide the eye. Inset, for compensated temperature structure functions $R_2/r^{2/3}$. Lines are for RB (red thick), and for boiling convection with 10000 (Boiling A - blue dash), 50000 (Boiling B - green dash-dot), and 150000 (Boiling C - black continuous) bubbles.

4.4 Structure functions

To understand the small scale statistics, we consider the transverse structure functions in the radial direction at the mid-height plane for the vertical velocity and the temperature. This is chosen such that the complicated boundary-layer dynamics are absent and there is hardly any mean vertical thermal gradient. Studies have shown that the anomalous nature of the structure functions are prominent in the transverse direction as compared to the longitudinal direction [30, 31] and hence only the transverse (radial) dynamics is studied.

Usually, the energy distribution on the different scales are expressed by second order structure functions R_2 (for temperature) and S_2 (for velocity). In Figure 4.3,

we show these structure functions for standard RB and for boiling convection. At very small scales, i.e., $r/\eta \leq 1$ in the dissipation range, the thermal energies (solid symbols) in the boiling and the RB convection are comparable. As we move away from the dissipation range towards the integral scale ($r/\eta \geq 60$), the thermal energy in case of boiling decreases. The rising vapor bubbles smoothen the temperature field by exchanging heat with the local fluid. To guide the eye, different theoretical scaling behaviors are shown in the same figure. In the inertial range $10 \leq r/\eta \leq 60$, a fit gives $R_2 \propto r^{0.60\pm0.010}$ for the standard RB and $R_2 \propto r^{0.65\pm0.005}$ for the boiling RB convection, i.e., very close to the Obukhov-Corrsin (OC) estimate where $R_2 \propto r^{2/3}$ for the passive scalars. The compensated structure functions, R_2/r^{α} with $\alpha = 2/3$ for OC are shown in the inset of the same figure. The plateau in the compensated plot is more visible for the boiling convection than in the standard RB convection.

Large scale *kinetic* energy is larger in case of boiling convection as compared to the standard RB case which means that there is an increase in the level of fluctuations, see open symbols in Figure 4.3, which shows the velocity structure functions. We interpret this as consequence of the extra mechanical driving provided by the rising vapor bubbles. In the viscous subrange both velocity structure functions of course follows $S_2 \propto r^2$. In the inertial range, we find that $S_2 \propto r^{0.72\pm0.040}$ for the standard RB and $S_2 \propto r^{0.68\pm0.010}$ for the boiling convection with the slight intermittency correction from the K41 scaling $S_2 \propto r^{2/3}$.

The local rms temperature $\sigma(r)$ on scale r is shown in inset of Figure 4.4. As the scale separation increases, $\sigma(r)$ increases, indicating that the larger scales have more thermal energy. For any scale r, the thermal fluctuations in boiling are smaller than those in the standard RB convection as already seen in Figure 4.3. PDFs of temperature increments in the inertial range are shown in the main panel of Figure 4.4. Rare events are observed at the tails of the PDFs which indicate the intermittency and they strongly deviate from the Gaussian curve (dash line). The PDF of the standard RB shows a stretched exponential like shape, see the red circles with a stretched exponential fit. The shape of the PDF depends on the spatial scale and is well studied [33–37]. The explanation for the exponential tails is due to the anomalous mixing of the fluid particles for which the mixing time is longer than the typical integral time, see Refs. [6, 36]. Our data from the boiling simulations are also shown on the same figure. We can see that the PDFs in boiling are sub-Gaussian, in contrast to the standard RB case. The statistical information is checked for convergence issues as in Ref. [38]. In Figure 4.5, we show X vs. $|X|^n P(X)$ for the moments n=4, 6 and 8. The areas under the curves are converged which indicates that the statistics in our simulations is sufficient and the moments are well converged.

In Figure 4.6, we show higher-order structure functions for $n = 2$ to 8 for stan-

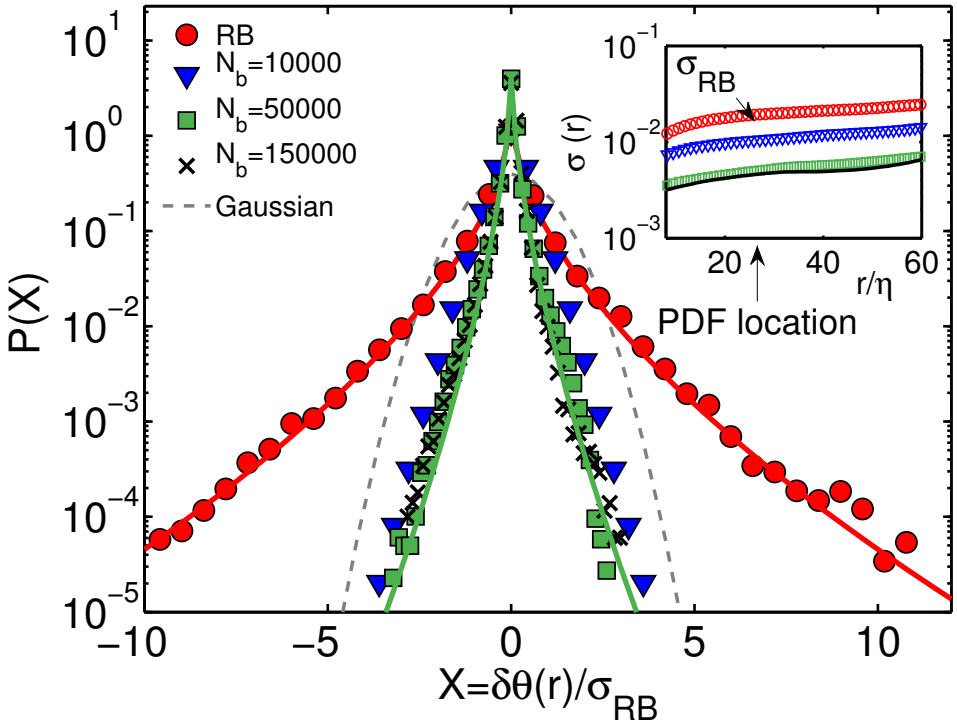

Figure 4.4: Probability density functions of normalized temperature increments in inertial range at $r/\eta = 25$. Data for RB (red circles), $N_b = 10000$ (blue triangles), $N_b = 50000$ (green squares), and $N_b = 150000$ (black crosses). Continuous lines are fits and dash line for normal Gaussian. In inset, rms of temperature increment $\sigma(r)$.

dard RB (see panel a), and boiling convection (see panel b). The structure functions are normalized with the corresponding n-th power of global rms temperatures mentioned in Table 4.1. Due to small Taylor-Reynolds numbers the flow scales are not widely separated and a clear scaling nature is absent. A better way of capturing the scaling exponent ζ_n is based on comparing different order structure functions, a method known as Extended Self Similarity (ESS) [39–42]. Such kind of ESS plots, say R_n vs. R_2, are shown in Figure 4.7. We can see that the scaling has improved [43]. We also extract the relative scaling exponent $\zeta_n/\zeta_2 = d[log_{10}(R_n)]/d[log_{10}(R_2)]$ [44].

In Figure 4.8 ζ_n/ζ_2 of the temperature field is shown for different moments. We can see that the relative scaling exponent of given moment n is almost constant and indicates that the computed scaling exponent is a reliable estimate. The obtained relative scaling exponents are higher, signaling lower intermittency in case of boiling convection as compared to the standard RB convection.

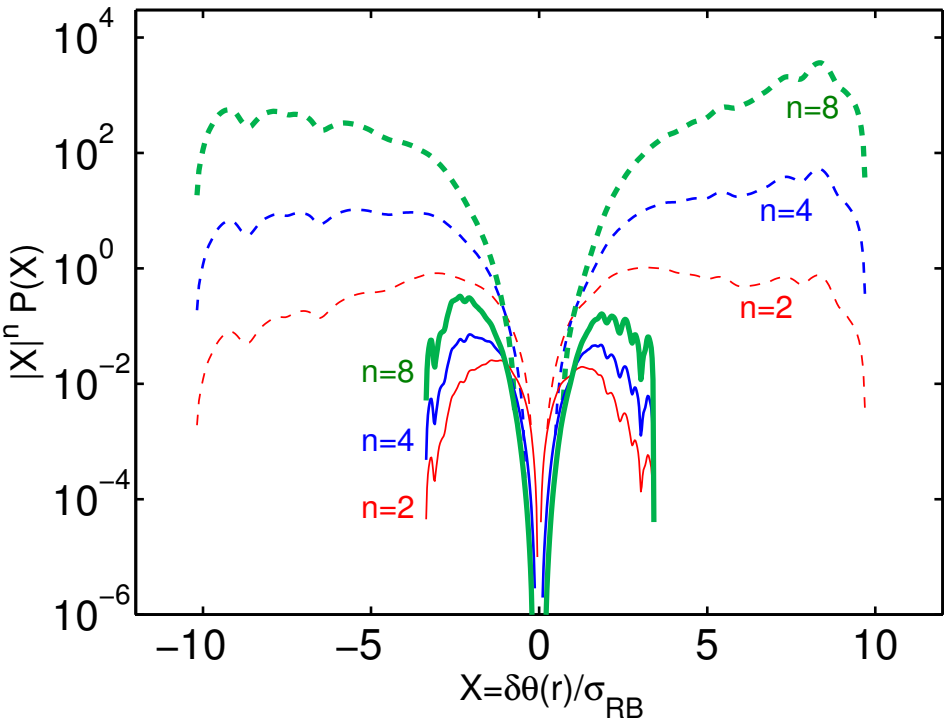

Figure 4.5: Convergence test for higher moments for $n = 4$ (very thin), $n = 6$ (thin), and $n = 8$ (thick). Dash lines for RB, and solid lines for boiling convection ($N_b = 10000$). Note the logarithm scale on vertical axis for a clear view on convergence.

4.5 Intermittency

In Figure 4.9, the absolute scaling exponent ζ_n [¶] is shown for various models, experimental studies, and numerical simulations on passive scalars including our results on standard RB and boiling convection. As we mentioned, any deviations from K41 theory ($n/3$ line) indicates intermittency. Various theoretical models such as the β model, the multifractal model, the Log-normal model, and the She-Leveque (SL94) model have been proposed in earlier literature on intermittency, see Ref. [2, 45]. The latter is given for comparison. It can be extended to passive scalar fluctuations, as proposed by Ruiz-Chavarria *et al.*, (RCBC96) see Ref. [46]. That model suggests that the most intermittent structures are the convoluted sheets or the 'fronts'. Numerical simulations on random velocity fields support the observed intermittent nature of the passive fields (CK98), see Ref. [47]. In experiments on grid turbulence (MW98)

[¶]Obtained by multiplying ζ_2 with the relative scaling exponent ζ_n/ζ_2 averaged in the inertial range.

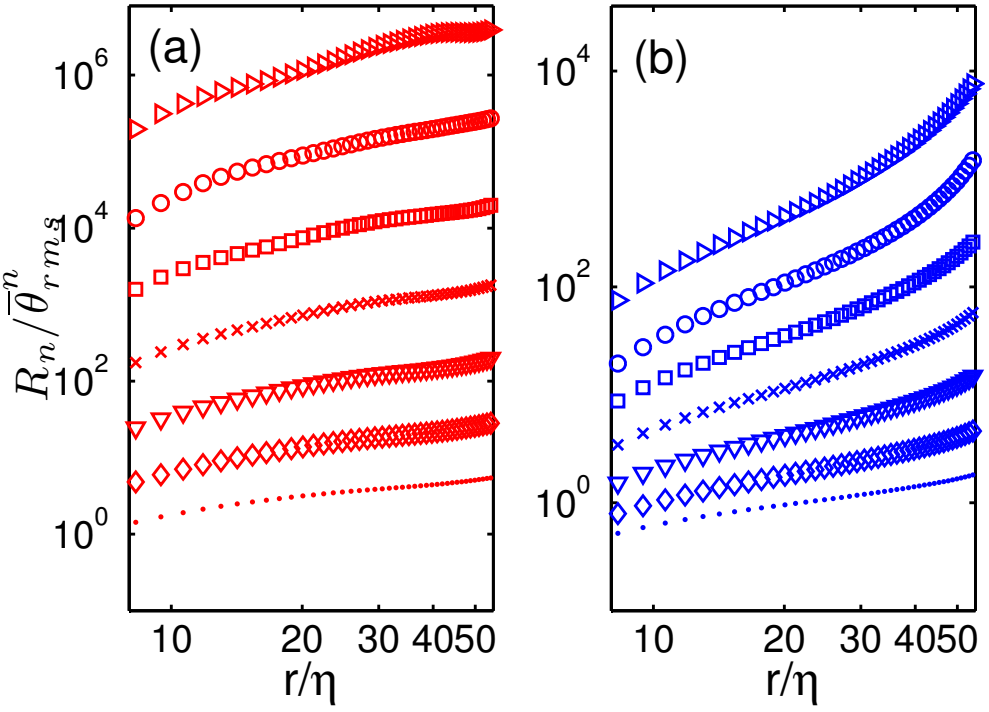

Figure 4.6: Normalized temperature structure functions $R_n/\overline{\theta}^n_{rms}$ in inertial range for (a) standard RB, and (b) boiling convection. The order n =2 to 8 increases from bottom to top. Axes are on logarithmic co-ordinates and scale limits are different.

the intermittency in the scalar fields have been observed to be similar to that in those simulations [48].

First, we reproduce the experimental results of Ruiz-Chavaria et al. [46] for the scaling of a *passive scalar* and also numerical results on passive scalar scaling [47], thus numerically confirming the earlier experimental findings of Sun *et al.* [3, 32] that the statistical properties of the temperature fluctuations in the bulk of the RB cell are similar to that of a passive scalar. Second, we find that the scaling exponents ζ_n in our RB simulations with vapor bubbles are significantly moved upwards, reflecting the decrease of intermittency through the smoothing bubbles, as we had already seen from the much less intermittent PDFs (see Figure 4.4). This trend is in clear contrast to the Lattice Boltzmann (LB) study of Ref. [49] which reports an enhanced intermittency for the boiling convection as compared to the standard RB case. In our boiling simulations vapor bubbles are always at the saturation condition with a fixed mean temperature, whereas in the LB simulations, bubbles could be at

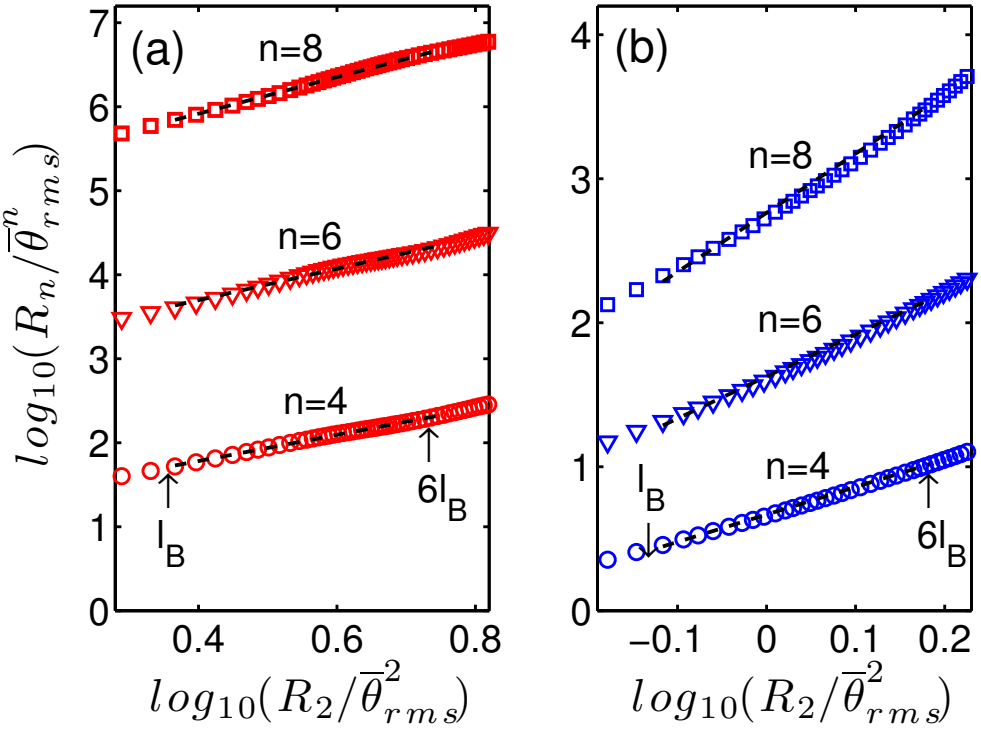

Figure 4.7: ESS scaling plots based on R_n vs. R_2 for (a) standard RB, and (b) boiling convection. Symbols are for moments $n = 4$ (circles), 6 (triangles), and 8 (squares). The structure functions are normalized with the corresponding n-th power of global rms temperature $\overline{\theta}_{rms}$. Dash lines indicate the scaling range for determining ζ_n.

different temperatures ranging in between the hot and cold plate temperatures. The other difference is that in our simulations nearly 10^5 bubbles are rising in a strongly driven large scale circulation (LSC). In case of the LB simulations, a few hundred of bubbles are swarming in a periodic box without LSC but with a complete flow resolution surrounding the bubble surface. These differences might lead to the different scaling exponents observed in the simulations. Interestingly, in our parameter regime with many bubbles the scaling exponents for the three analyzed cases with 10000 (A), 50000 (B) and 150000 (C) vapor bubbles have very similar scaling exponents, showing that the smoothening effect saturates and is robust.

To summarize, we have conducted a systematic study of the statistics of the scalar fields for classical Rayleigh-Bénard (RB) convection and boiling convection with point-like saturated vapor bubbles. Our numerical simulations show that the

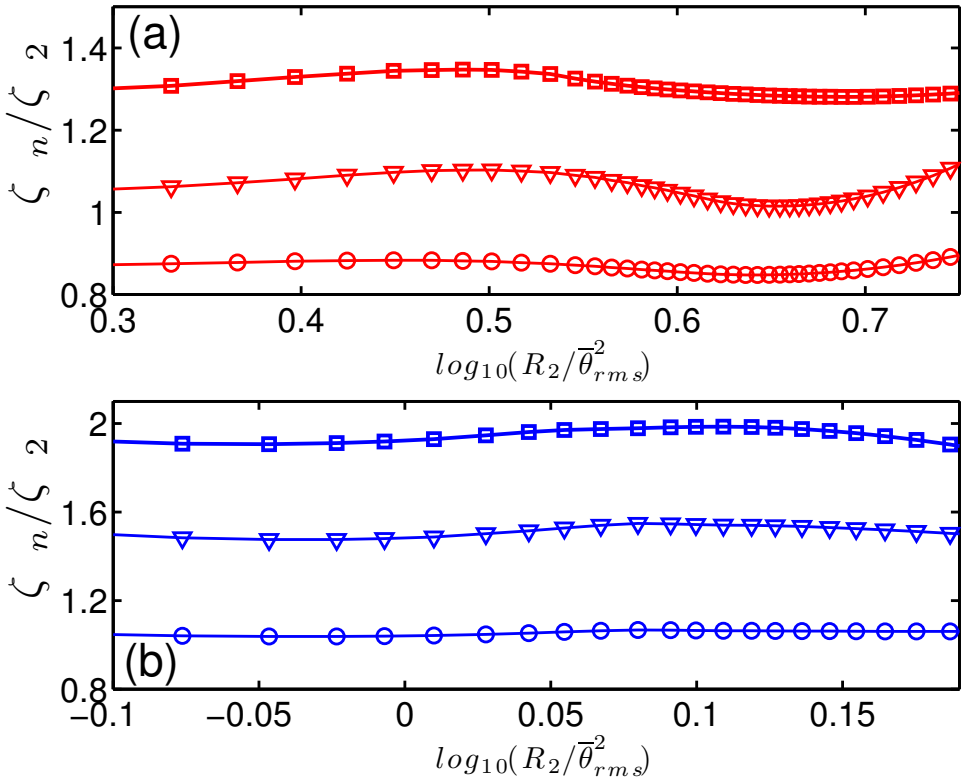

Figure 4.8: Relative scaling exponent ζ_n/ζ_2 : (a) RB, and (b) boiling convection. Order n increases from down to top. Symbols are for $n = 4$ (circles), 6 (triangles), and 8 (squares).

vapor bubbles have a strong influence on the temperature field and smoothens the temperature. Our results show a robust trend and are independent of the number of bubbles, provided that is is large enough.

References

[1] L.D. Landau and E.M. Lifshitz, *Fluid Mechanics*, (Pergamon Press, 1987).

[2] U. Frisch, *Turbulence, the legacy of A. N. Kolmogorov*, (Cambridge Univ. Press, 1995).

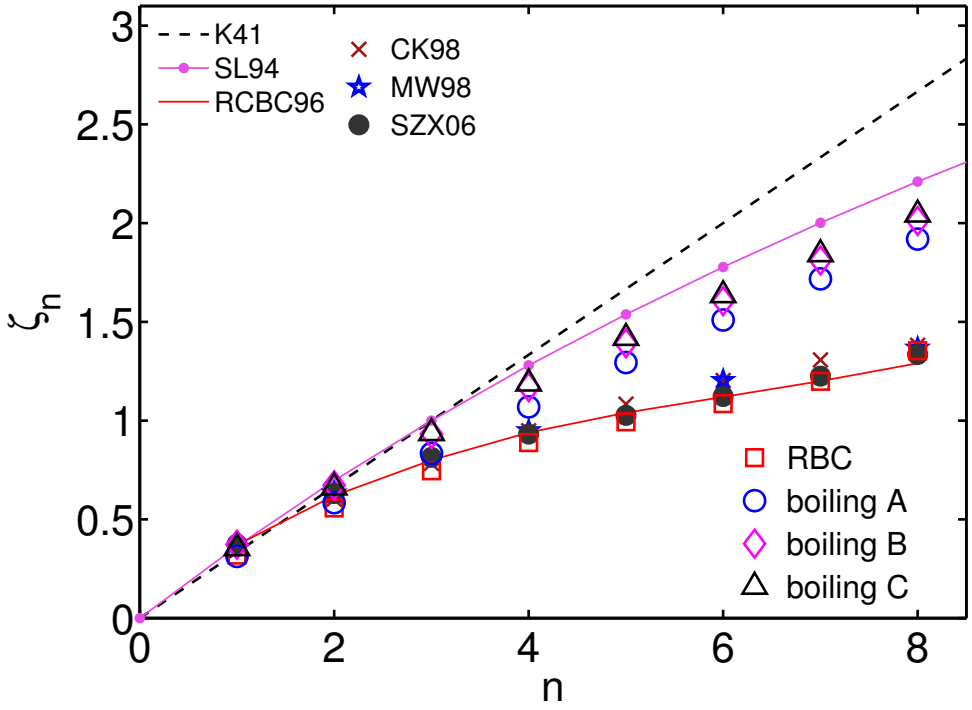

Figure 4.9: Scaling exponents of temperature structure function ζ_n. Data are K41 (dash), SL94 (line with dot) from Ref. [45], RCBC96 (continuous line) from Ref. [46], CK98 (diamonds) from Ref. [47], MW98 (stars) from Ref. [48], SZX06 (solid circles) from Ref. [32]. Our simulations on standard RB (squares), and boiling convection with $N_b = 10000$ (open circles), 50000 (diamonds), and 150000 (traingles) bubbles.

[3] D. Lohse and K. Q. Xia, *Small-Scale Properties of Turbulent Rayleigh-Bénard Convection*, Ann. Rev. Fluid Mech. **42**, 335 (2010).

[4] F. Anselmet, Y. Gagne, E. J. Hopfinger, and R. A. Antonia, *High-order velocity structure functions in turbulent shear flows*, J. Fluid Mech. **140**, 63-69 (1984).

[5] S. Grossmann, D. Lohse, and A. Reeh, *Developed turbulence: From full simulations to full mode reductions*, Phys. Rev. Lett., **77**, 5369-5372 (1996).

[6] B. I. Shraiman and E. D. Siggia, *Scalar turbulence*, Nature, **405**, 639-646 (2000).

[7] K. R. Sreenivasan, *On local isotropy of passive scalars in turbulent shear flows*, Proc. R. Soc. Lond. A **434**, 165-182 (1991).

[8] A. Pumir, *A numerical study of the mixing of a passive scalar in three dimensions in the presence of a mean gradient*, Phys. Fluids, **6**, 2118 (1994)

[9] A. Pumir, *Structure of the three-point correlation function of a passive scalar in the presence of a mean gradient*, Phys. Rev. E **57**, 2914 (1998)

[10] A. Celani, A. Lanotte, A. Mazzino, and M. Vergassola, *Universality and saturation of intermittency in passive scalar turbulence*, Phys. Rev. Lett., **84**, 2385-2388 (2000)

[11] Z. Warhaft, *Passive scalars in turbulent flows*, Annu. Rev. Fluid Mech. **32**, 203 (2000).

[12] F. Moisy, H. Willaime, J. Anderson, and P. Tabeling, *Passive scalar intermittency in low temperature helium flows*, Phys. Rev. Lett, **86**, 4827-30 (2001)

[13] G. Ahlers, S. Grossmann, and D. Lohse, *Heat transfer and large scale dynamics in turbulent Rayleigh-Bénard convection*, Rev. Mod. Phys. **81**, 503 (2009).

[14] A.M.Obukhov, *Structures of temperature field in a turbulent flow*, Izv.Akad. Nauk. SSSR Ser. Geog. Geofiz. **13**, 58-69 (1949).

[15] S. Corrsin, *On the spectrum of isotropic temperature fluctuations in anisotropic turbulence*, J. Appl. Phys. **22**, 469 (1951).

[16] R. Bolgiano, *Turbulent spectra in a stably stratified atmosphere*, J. Geophys. Res. 64 (12), 2226-2229 (1959).

[17] A. M. Obukhov, *Effect of Archimedean forces on the structure of the temperature field in a turbulent flow*, Dokl. Akad. Nauk. SSSR 125, 1246 (1959).

[18] E.S.C. Ching, *Intermittency of temperature field in turbulent convection*, Phys. Rev. E, **61**, R 33-36 (2000)

[19] E.S.C. Ching, Y. Cohen, T. Gilbert, and I. Procaccia, *Active and passive fields in turbulent transport: the role of statistically preserved structures*, Phys. Rev. E, **67**, 016304 (2003)

[20] E.S.C. Ching, and W.C.Cheng, *Anomalous scaling and refined similarity of an active scalar in a shell model of turbulent convection*, Phys. Rev. E, **77**, 015303 (2008)

[21] E.S.C. Ching, H. Guo, T. S. Lo, *Refined similarity hypotheses in shell models of homogeneous turbulence and turbulent thermal convection*, Phys. Rev. E, **78**, 026303 (2008)

[22] P. Oresta, R. Verzicco, D. Lohse, and A. Prosperetti, *Heat transfer mechanisms in bubbly Rayleigh-Bénard convection*, Phys. Rev. E **80**, 026304 (2009).

[23] R. Verzicco and R. Camussi, *Numerical experiments on strongly turbulent thermal convection in a slender cylindrical cell*, J. Fluid Mech. **477**, 19 (2003).

[24] L. E. Schmidt, P. Oresta, F. Toschi, R. Verzicco, D. Lohse, and A. Prosperetti, *Modification of turbulence in Rayleigh-Bénard convection by phase change*, New Journal of Physics **13**, 025002 (2011).

[25] R. Lakkaraju, L. E. Schmidt, P. Oresta, F. Toschi, R. Verzicco, D. Lohse, and A. Prosperetti, *Effect of vapor bubbles on velocity fluctuations and dissipation rates in bubbly Rayleigh-Bénard convection*, Phys. Rev. E **84**, 036312 (2011).

[26] R. Lakkaraju, R. J. A. M. Stevens, P. Oresta, R. Verzicco, D. Lohse, and A. Prosperetti, *Heat transport in boiling turbulent Rayleigh-Bénard convection*, Submitted to Proc. Natl. Acad. Sciences, The USA (2012).

[27] M.R. Maxey and J.J. Riley, *Equation of motion for a small rigid sphere in a nonuniform flow*, Phys. Fluids **26**, 883-889 (1983).

[28] B. I. Shraiman, and E. D. Siggia, *Transport in High Rayleigh Number Convection*, Phys. Rev. A **42**, 3650 (1990).

[29] E. D. Siggia, *High Rayleigh number convection*, Annu. Rev. Fluid. Mech.**26**, 137 (1994).

[30] S. Grossmann, D. Lohse, and A. Reeh, *Different intermittency for longitudinal and transversal turbulent fluctuations*, Phys. Fluids **9**, 3817-3825 (1997).

[31] A. Staicu, and W. van de Water, *Small Scale Velocity Jumps in Shear Turbulence*, Phys. Rev. Lett. **90**, 094501 (2003).

[32] C. Sun, Q. Zhou, and K,-Q. Xia, *Cascades of Velocity and Temperature Fluctuations in Buoyancy-Driven Thermal Turbulence*, Phys. Rev. Lett., **97**, 144504 (2006).

[33] B. Castaing, Gunaratne, G. Heslot, L. F. Kadanoff, A. Libchaber, A. S. Thomae, X. Z. Wu, S. Zaleski, and G. Zanetti, *Scaling of hard thermal turbulence in Rayleigh-Bénard convection*, J. Fluid Mech. **204**, 1 (1989).

[34] A. Pumir, B. Shraiman, and E. D. Siggia, *Exponential tails and random advection*, Phys. Rev. Lett., **3**, 2838-2840 (1991).

[35] J. P. Gollub, J. Clarke, M. Gharib, B. Lane, O. N. Mesquita, *Fluctuations and transport in a stirred fluid with a mean gradient*, Phys. Rev. Lett., **67**, 3507-3510 (1991).

[36] M. Holzer, and A. Pumir, *Simple models of non-Gaussian statistics for a turbulently advected passive scalar*, Phys. Rev. E, **47**, 202-219 (1993).

[37] M. Holzer, and E. D. Siggia, *Turbulent mixing of a passive scalar*, Phys. Fluids, **6**, 1820-1837 (1994).

[38] F. Belin, P. Tabeling, and H. Willaime, *Exponents of the structure functions in a low temperature helium experiment*, Physica D, Nonlinear Phenomena **93(1-2)**, 5263 (1996).

[39] R. Benzi, S. Ciliberto, R. Trippiccione, C. Baudet, F. Massaioli, and S. Succi, *Extended self-similarity in turbulent flows*, Phys. Rev. E **48**, R29 (1993).

[40] M. Briscolini, P. Santangelo, S. Succi, and R. Benzi, *Extended self-similarity in the numerical simulation of three-dimensional homogeneous flows*, Phys. Rev. E, **50**, R1745 (1994)

[41] S. Grossmann, D. Lohse, and A. Reeh, *Developed turbulence: From full simulations to full mode reductions*, Phys. Rev. E **77**, 5369 (1996).

[42] S. Grossmann, D. Lohse, and A. Reeh, *Application of extended self-similarity in turbulence*, Phys. Rev. E **56**, 5473 (1997).

[43] Babiano, A. and Dubrulle, B. and Frick, P., *Scaling properties of numerical two-dimensional turbulence*, Phys. Rev. E. **52**, 3719 (1995).

[44] R. Benzi, L. Biferale, R. T. Fischer, L. P. Kadanoff, D. Q. Lamb, and F. Toschi, *Intermittency and universality in fully developed inviscid and weakly compressible turbulent flows*, Phys. Rev. Lett. **100**, 234503 (2008).

[45] Z. S. She, and E. Leveque, *Universal scaling laws in fully developed turbulence*, Phys. Rev. Lett., **72**, 336-339 (1994)

[46] G. Ruiz-Chavarria, C. Baudet, and S. Ciliberto, *Scaling laws and dissipation scale of a passive scalar in fully developed turbulence*, Physica D Nonlinear Phenomena, **99**, 369-380 (1996)

[47] S. Chen, and R. H. Kraichnan, *Simulations of a randomly advected passive scalar field*, Physics of Fluids, **10**, 2867 (1998)

[48] L. Mydlarski, A. Pumir, B. I. Shraiman, E. D. Siggia, and Z. Warhaft, *Structures and Multipoint Correlators for Turbulent Advection: Predictions and Experiments*, Phys. Rev. Lett., **81**, 4373 (1998)

[49] L. Biferale, P. Perlekar, M. Sbragaglia, and F. Toschi, *Convection in multiphase fluid flows using lattice boltzmann methods*, Phys. Rev. Lett. **108**, 104502 (2012).

5

SPATIAL DISTRIBUTION OF HEAT FLUX AND FLUCTUATIONS IN TURBULENT RAYLEIGH-BÉNARD CONVECTION *

*We numerically investigate the radial dependence of the velocity and temperature fluctuations and of the time-averaged heat flux $\overline{j}(r)$ in a cylindrical Rayleigh-Bénard cell with aspect ratio $\Gamma = 1$ for Rayleigh numbers Ra between 2×10^6 and 2×10^9 at a fixed Prandtl number $Pr = 5.2$. The numerical results reveal that the heat flux close to the side wall is larger than in the center and that, just as the global heat transport, it has an effective power law dependence on the Rayleigh number, $\overline{j}(r) \propto Ra^{\gamma_j(r)}$. The scaling exponent $\gamma_j(r)$ decreases monotonically from 0.43 near the axis ($r \approx 0$) to 0.29 close to the side walls ($r \approx D/2$). The effective exponents near the axis and the side wall agree well with the measurements of Shang et al. (Phys. Rev. Lett. **100**, 244503, 2008) and the predictions of Grossmann and Lohse (Phys. Fluids **16**, 1070, 2004). Extrapolating our results to large Rayleigh number would imply a crossover at $Ra \approx 10^{15}$, where the heat flux near the axis would begin to dominate. In addition, we find that the local heat flux is more than twice as high at the location where warm or cold plumes go up or down, than in plume depleted regions.*

*Published as: R. Lakkaraju, R. J. A. M. Stevens, R. Verzicco, S. Grossmann, A. Prosperetti, C. Sun, and D. Lohse, 'Spatial distribution of heat flux and fluctuations in turbulent Rayleigh-Bénard convection', *Physical Review E*, **86**, 056315 (2012)

5.1 Introduction

In Rayleigh-Bénard (RB) convection a fluid is heated from below and cooled from above. This problem of thermal convection is of the utmost importance from an applied point of view. Examples are thermal convection in the atmosphere, in the oceans and in process technology. For recent reviews of RB convection we refer to Refs. [1, 2].

In a cylindrical container, the dynamics of a RB system depends on three control parameters, the Rayleigh number $Ra = g\beta\Delta L^3/\nu\kappa$, the Prandtl number $Pr = \nu/\kappa$, and the aspect ratio $\Gamma = D/L$. Here g is the gravitational acceleration, β the isobaric thermal expansion coefficient, Δ the temperature difference between the top and bottom plates, ν the kinematic viscosity, κ the thermal diffusivity, and L and D are the height and diameter of the cylinder. The response of the system is expressed by the Nusselt number Nu, the dimensionless heat flux [1].

Previous studies mainly focused on determining the global heat flux as a function of Ra and Pr. For water ($Pr = 4-6$), in the experimentally available range of $Ra = 10^8 - 10^{11}$, one finds that the global heat transport effectively scales as $Nu \sim Ra^{0.29-0.31}$ [1, 3–8]. The effective exponents for the global heat flux are well described by the unifying theory of Refs. [4, 9–11]. That theory also made predictions for the scaling exponents of the local heat flux in the center of the cell and at the side wall [11]. The reasoning is based on splitting the thermal energy dissipation field into its plume and background contributions; similarly the kinetic energy dissipation is decomposed into its boundary layer and bulk contributions. By doing this Grossmann and Lohse [11] accounted for the various scalings in the $Ra - Pr$ parameter space. They found that the local heat flux has an effective power law dependence on the Ra number, $\overline{j}(r) \propto Ra^{\gamma_j(r)}$, and obtained a prediction for the scaling exponent $\gamma_j = 0.45$ in the bulk (center) and $\gamma_j = 0.22$ at the plume (side wall) regions.

In order to understand the heat flux one has to either rely on Eulerian [12] or Lagrangian [13, 14] measurements where the complex interplay between velocity and temperature can be studied. Advancements in experimental techniques made it possible to measure the vertical local velocity $u_z(\mathbf{r},t)$ and the local temperature $T(\mathbf{r},t)$ at a given spatial location $\mathbf{r}$ as functions of time. This allowed Shang et al. [12, 15, 16] to determine the local convective heat flux [17]

$$j(\mathbf{r},t) = \frac{u_z(\mathbf{r},t)[T(\mathbf{r},t) - T_0]}{\kappa\Delta/L}, \tag{5.1}$$

where T_0 is the mean bulk temperature. They determined the probability density functions (PDF) of the local heat flux in the axis and side wall regions and showed that the vertical heat flux is highly non-Gaussian and intermittent due to thermal

Table 5.1: Summary of simulation parameters: The number of grid points used in angular (N_ϕ), radial (N_r), and axial directions (N_z), volume and time averaged Nusselt number (Nu), the number of grid points in the thermal boundary layer (n_{bl}), convergence of exact relations for ε_K and ε_T, comparing maximum of grid spacing in angular ($\delta\phi_m$) and axial (δz_m) directions with the Kolmogorov length scale based on global kinetic energy dissipation rate (η) and the averaging time considered for the simulations are shown. The reported times are always measured in the units of free-fall time and the lengths in terms of cylinder height. For statistical averages we discarded the initial 140 free-fall times, to prevent transient effects from contaminating in the results.

Ra	$N_\phi \times N_r \times N_z$	Nu	n_{bl}	$\frac{\varepsilon_K}{\frac{\nu^3}{L^4}\frac{Ra}{Pr^2}(Nu-1)}$	$\frac{\varepsilon_T}{\kappa\frac{\Delta^2}{L^2}Nu}$	$\delta\phi_m, \delta z_m, \eta$ $(\times 10^2)$	in L/U
2×10^6	$193 \times 49 \times 129$	10.93	19	1.008	0.968	2.26, 1.45, 3.41	4200
1×10^7	$257 \times 65 \times 193$	16.58	18	1.010	0.971	2.44, 0.73, 2.04	3700
2×10^7	$257 \times 65 \times 193$	20.71	18	1.007	0.843	2.44, 0.73, 1.62	3700
6×10^7	$321 \times 97 \times 239$	28.48	14	0.989	0.923	1.96, 0.97, 1.13	3000
1×10^8	$385 \times 129 \times 257$	33.25	15	0.997	0.955	1.62, 0.73, 0.95	2800
2×10^8	$385 \times 129 \times 257$	40.87	13	1.002	0.937	1.62, 0.73, 0.76	2700
5×10^8	$513 \times 161 \times 321$	52.80	13	1.005	0.947	1.22, 0.51, 0.56	1900
2×10^9	$769 \times 193 \times 385$	80.34	11	0.992	0.959	0.82, 0.34, 0.26	2040

plumes. This work stimulated Ching et al. [18] to theoretically study the problem. They decomposed the velocity field into a part associated with strong temperature fluctuations plus a background and found that, with the definitions they used, the local heat transport associated with the former velocity component near the axis of the cell scaled as $Ra^{1/7}$. Later experiments by Shang et al. [16] revealed that the effective scaling exponent for the local heat flux is about 0.49 near the cell axis and about 0.24 near the side wall, which confirms the main results obtained by Grossmann and Lohse [11], but is in disagreement with the model of Ching et al. [18].

In experiments it is quite difficult to measure the heat flux at each spatial point in the cell due to problems with measurement techniques and the presence of inherent noise levels. The measurements at just one or two points may not be enough to understand the complex dynamics involved in the convection process. The present work offers numerical results which complement the work initiated by Shang et al. [12, 16]. We provide information on the heat flux at one quarter, one half, and

three quarters of the cell height for several radial positions r, not only near the axis and the side wall. This information allows us to understand the two limits in the unifying theory [11] on the effective scaling exponents, one valid in the bulk (the central region of the cell) and the other valid in the plume region. As a result we clearly see persistence of the inhomogeneous nature of the flow in the radial direction which leads to different scaling exponents.

In experiments the local velocity is measured by LDV/PIV techniques at a spatial position which slightly differs from the location of the local temperature measurement. This spatial misalignment may possibly affect the results. In numerical simulations, in contrast, one has all the information on the flow field and thus the local heat flux can be calculated from the velocity and temperature measurements at exactly the same position. Finally we comment on the local heat flux distribution with respect to the large scale circulation and the ultimate regime mentioned in Refs. [9, 11, 19] and provide data to illuminate the differences between the measurements of Shang et al. [16] and the earlier Ching et al. [18] claims.

In simulations the Ra number range and the duration available for time-averaging are more limited than in experiments. In order to mitigate the latter shortcoming we have limited the Ra number of our simulations. In the next section we briefly describe the numerical procedure before discussing our results on the local heat flux and the velocity and temperature fluctuations.

5.2 Numerical method

We performed direct numerical simulations for a Boussinesq fluid in a unit aspect ratio ($\Gamma = 1$) cylinder with constant temperatures applied at the top and bottom plates and an adiabatic side wall. The fluid simulated in our calculations is water at 32 ^{o}C ($Pr = 5.2$) for $2 \times 10^6 \leq Ra \leq 2 \times 10^9$. The governing equations for momentum, energy and mass conservation in dimensionless form are given by [20]

$$\frac{D\mathbf{u}}{Dt} = -\nabla p + \theta \hat{\mathbf{z}} + \left(\frac{Pr}{Ra}\right)^{1/2} \nabla^2 \mathbf{u}, \tag{5.2}$$

$$\frac{D\theta}{Dt} = \frac{1}{(PrRa)^{1/2}} \nabla^2 \theta, \quad \nabla \cdot \mathbf{u} = 0. \tag{5.3}$$

Here the dimensionless variables are the velocity $\mathbf{u}$, scaled temperature θ and pressure p (minus the hydrostatic contribution). The material derivative is denoted by D/Dt. The unit vector $\hat{\mathbf{z}}$ is in the direction opposite to gravity. The physical variables length and velocity are made non-dimensional by the cylinder height (L), and the free-fall velocity $U = \sqrt{g\beta\Delta L}$. Constant dimensionless temperatures of 1 and 0 are applied at the bottom and top plate, respectively.

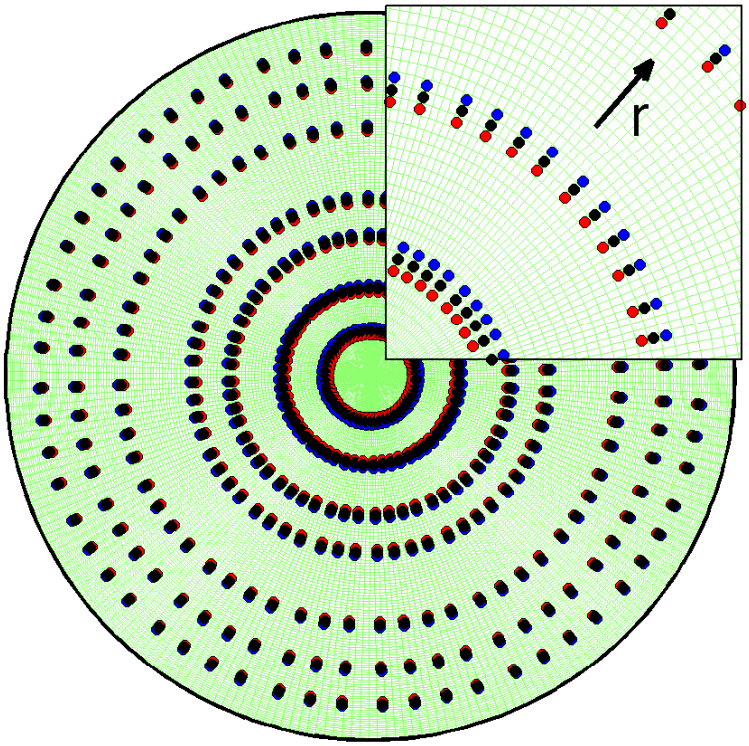

Figure 5.1: Computational grid used for $Ra = 2 \times 10^7$. We position numerical probes uniformly in the azimuthal direction in circles at seven radial locations $r/L = 0.06$, 0.12, 0.19, 0.24, 0.34, 0.40, 0.45 (shown in black). For better statistics, on the mid-plane, we use two more sets of probes (blue, red) with an offset of one grid point. Inset shows a close up view of the probe locations on the grid.

The governing equations are solved on a staggered grid with second-order accuracy in space and time. For the time advancement a third order Runge-Kutta scheme is used. This method is stable for a CFL number up to $\sqrt{3}$, and here we have limited it to 1.2 by adjusting the time step according to the maximum velocity before executing each time step [21]. The maximum time step of integration is further restricted to 0.01 free-fall times and the actual computed time step never exceeded this limit. More details about the numerical method can be found in Refs. [20, 22, 23]. For the spatial resolution we followed the criteria set by Stevens et al. [24].

The code has been validated by effecting many comparisons of the calculated Nusselt number with experimental data showing agreement within 1% [24]. Re-

cently we have shown that statistical quantities (relative strength and temperature amplitudes of the large-scale circulation, and sidewall temperature gradient) measured in experiments and simulations agree up to the statistical accuracy that can be obtained in simulations [25].

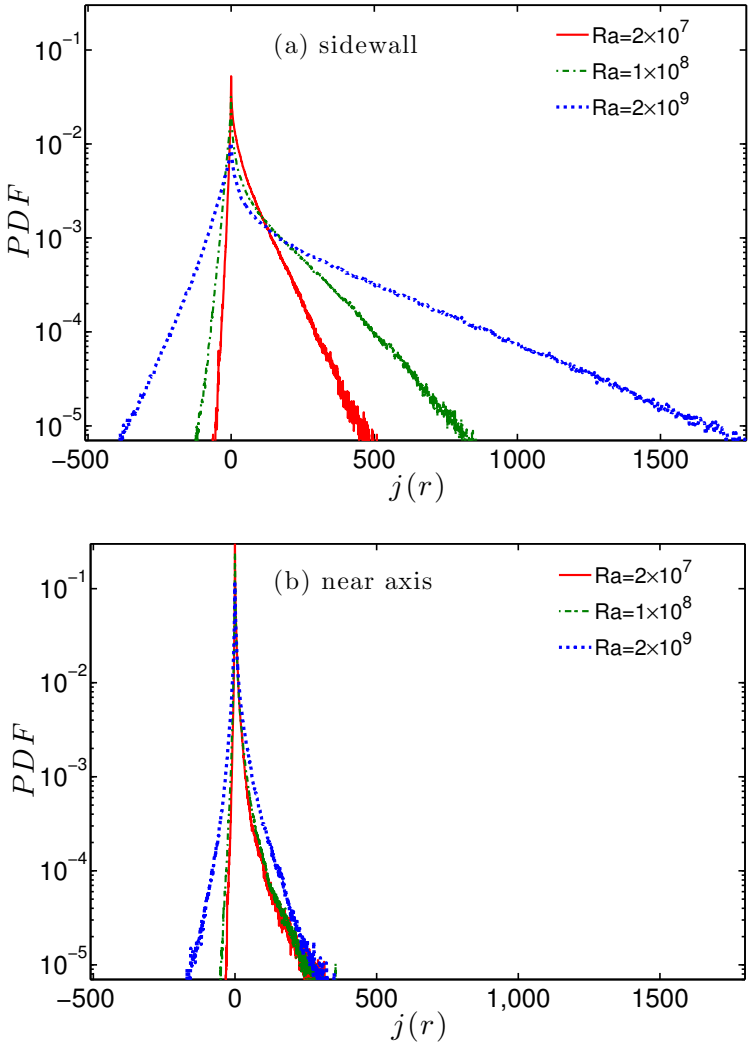

Figure 5.2: PDFs of the local instantaneous heat flux j (a) near the sidewall at $r/L = 0.45$ and (b) near the axis $r/L = 0.06$ at mid-height for $Ra = 2 \times 10^7$ (red), 1×10^8 (green), 2×10^9 (blue).

A summary of the simulation parameters is shown in Table 5.1. The first and

second columns are Ra and the number of grid nodes. The volume- and time-averaged global heat transport, i.e. the Nusselt number $Nu = 1 + \sqrt{RaPr}\left[\overline{\langle u_z\theta\rangle_V}\right]$, is shown in the third column; here the overline denotes time averages and the angular brackets $\langle\cdot\rangle_V$ volume averages. The number of grid points used to resolve the thermal boundary layers is shown in the fourth column. In a RB cell with no slip velocity condition at the walls the dimensional thermal energy dissipation rate, $\varepsilon_T = \kappa\Delta^2 L^{-2}\overline{\langle|\nabla\theta|^2\rangle_V}$, and kinetic energy dissipation rate $\varepsilon_K = \nu^3 L^{-4} Pr^{-1} Ra\overline{\langle|\nabla\mathbf{u}|^2\rangle_V}$ satisfy exact relationships with Nu (see Refs. [1, 26]), namely $\varepsilon_T = \kappa\Delta^2 L^{-2} Nu$ and $\varepsilon_K = \nu^3 L^{-4} Pr^{-2} Ra(Nu-1)$. In order to validate our simulations the obtained energy dissipation rates are compared with Nu in Table 5.1. These ratios are near one, which proves the adequacy of the grid resolution. In the seventh column the largest grid spacings in the azimuthal and axial directions are compared with the Kolmogorov length. In the last column the total time used for the statistical averages is shown in free-fall times (L/U). The total computational time was around 2.2×10^5 CPU hours on a Power6 computer consisting of $32(=2\times16)$ cores per node giving us 6875 Wall Clock Hours (units). This corresponds to $6875/24 = 287$ wall clock days spent on 8 simulations. This large amount of time was needed to resolve namely the small scale motions and heat flux events.

We placed 1880 "numerical probes" at different radial locations on three different horizontal planes (at z/L=0.25, z/L=0.50 and z/L=0.75), to obtain point-wise data on the temperature and vertical velocity in order to calculate the local heat flux according to equation (5.1). In each horizontal plane a number of azimuthally nearly equally spaced probes were placed on seven circles with radii $r/L = 0.06$, 0.12, 0.19, 0.24, 0.34, 0.40 and 0.45, see Figure 5.1. On each circle we distributed 60 probes at $z/L = 0.50$ and 20 probes at $z/L = 0.25$, 0.75. In addition, on the mid-plane, each circle was complemented by two other circles, one inside and one outside, spaced by one radial mesh length as shown in the upper right corner of Figure 5.1. In total, we have information from 60 (azimuthal) $\times$ 7 (radial) $\times$ 3 (sets)= 1260 probes at mid-height plane. For the planes at $z/L = 0.25$ and at $z/L = 0.75$ we have information from $20\times7 = 140$ probes.

5.3 Local heat flux

In Figure 5.2 we show PDFs for the local instantaneous heat flux j on the mid-plane, at two different radial positions, one near the cell axis ($r/L = 0.06$) and one near the side wall ($r/L = 0.45$). Note that the latter is outside the kinematic boundary layer (BL) which at this Prandtl number has a thickness of $\lambda_u/L \approx 3.6Ra^{-0.26\pm0.03}$ [28]. According to this scaling law we have $\lambda_u/L \approx 0.05$ for $Ra = 10^7$ and $\lambda_u/L \approx 0.016$ for

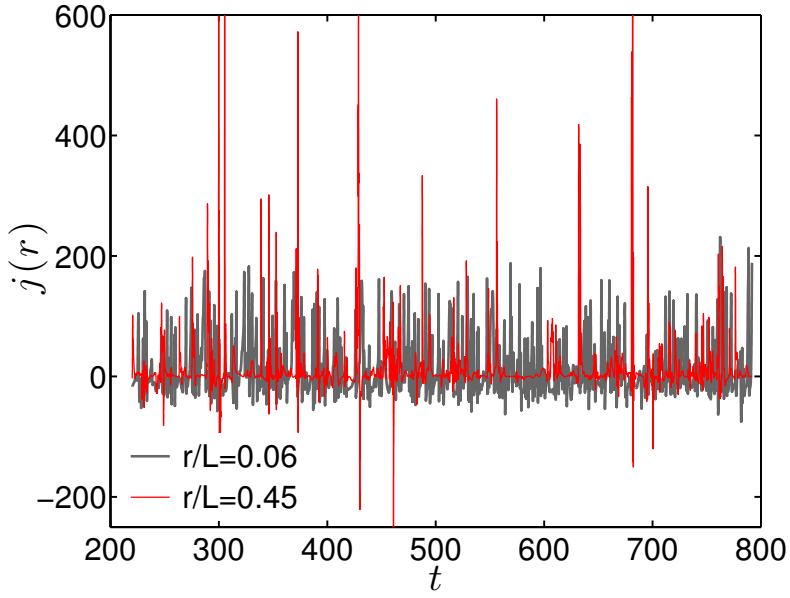

Figure 5.3: Time series for the heat flux near the side wall (thin, red) and in the center (thick, gray) for $Ra = 1 \times 10^8$.

$Ra = 10^9$. From our numerical calculations of the kinetic side wall BL thickness, as identified by the location of the maximal velocity fluctuations, we get even slightly smaller values. Obviously, there is no thermal BL at the side walls due to the adiabatic boundary conditions.

The first striking observation from Figure 5.2 is that the absolute value of the heat flux is much larger at the side walls (panel a) as compared to the center (panel b). This is consistent with the expectation that most of the heat is transported by the large-scale convection roll and of course it is well known [16]. Near the sidewall we observe some events with a heat flux as high as fifteen times the average. In this region, the PDF has a marked positive skewness due to rising and falling of the warm and cold plumes. The PDF of the local heat flux in the cell center also has a positive skewness, which indicates that plumes can travel through this region as well. Figure 5.3 shows examples of the time evolution of j as a function of the dimensionless time t close to the cell center (r/L=0.06, gray) and to the side wall (r/L=0.45, red) for $Ra = 10^8$ and again reflects the presence of much stronger heat transport events near the side wall than near the axis.

One of the main features of turbulence is the small scale intermittency that is measured as departure from a Gaussian character of the PDF, mainly the tails and

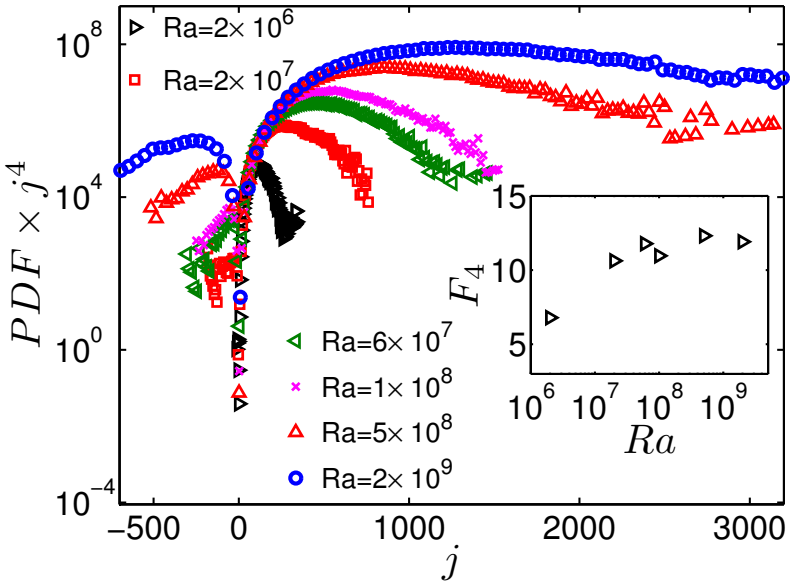

Figure 5.4: $j^4 \times PDF(j)$ vs. j is shown for different Ra near the side wall region showing convergence of the flatness at that location. Note that the vertical axis is given in log-scale, in contrast to the figures shown in the convergence test by Belin et al. [27], where $j^4 \times PDF(j)$ is given on a linear scale. The inset shows that the flatness F_4 increases as a function of Ra.

the peakedness. This can be quantified by calculating the flatness F_4 of the PDF. For strongly intermittent signals however the integral of $j^4 \times PDF(j)$ defining the flatness may not converge. To examine this issue we calculate the angular average of this quantity at $r/L = 0.06$ and at $r/L = 0.45$ on the mid-plane. While at the side wall this quantity decays for large $|\ j\ |$ sufficiently fast, see Figure 5.4 (this feature is more evident when data is plotted on a linear rather than log-scale), and thus permits the calculation of the flatness (showing strong intermittency, $F_4 \approx 11$, inset of Figure 5.4), in the center the intermittency is so strong that no convergence for the flatness can be achieved.

By rescaling the heat flux j with its standard deviation j_{rms}, the zero-mean PDF for the normalized heat flux $j^\star \equiv (j - \bar{j})/j_{rms}$ shows universality near the side wall (see Figure 5.5a). The tails for the rescaled PDFs are shorter at the side walls compared to those at the center. This indicates relatively fewer plumes carrying a large heat flux at the side walls in contrast to relatively more plumes carrying a smaller heat flux at the center, and again underlines the extremely strong intermittency of the heat flux on the axis (see Figure 5.5b).

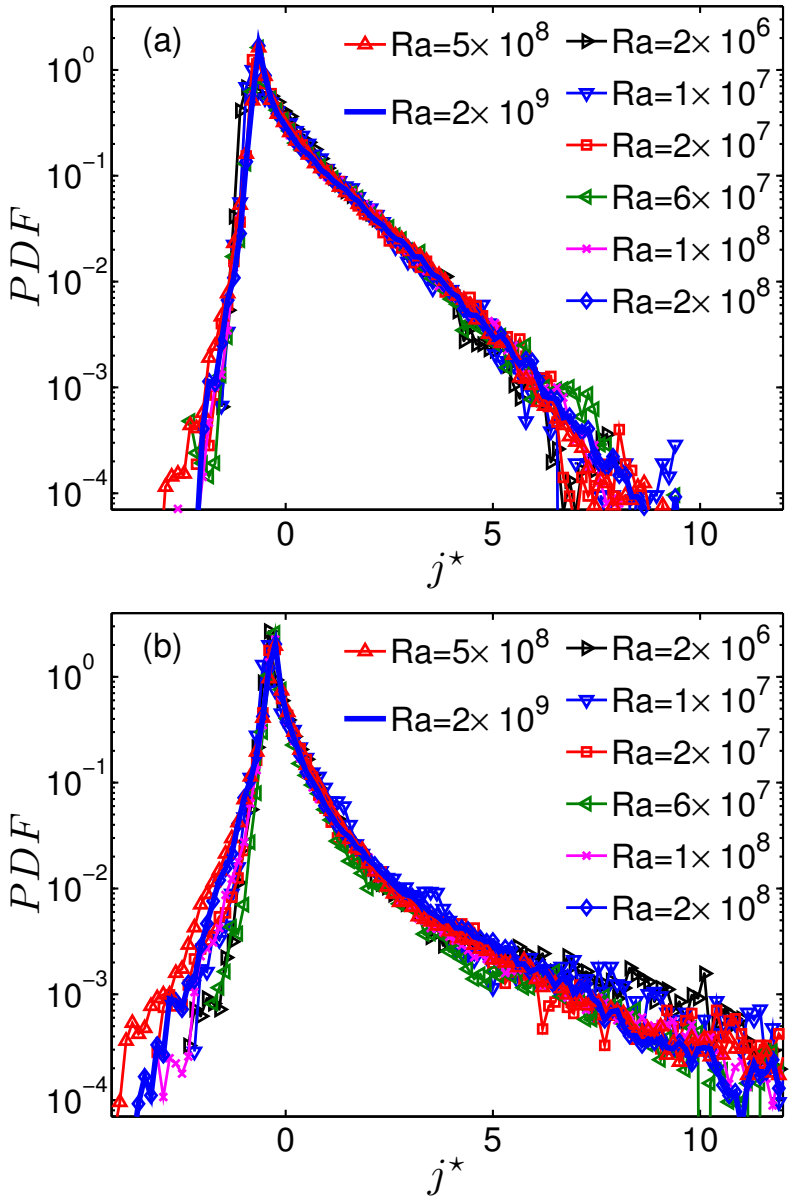

Figure 5.5: Centered PDFs of the normalized heat flux $j^\star(r) = (j(r) - \overline{j(r)})/j_{rms}(r)$ on the mid-plane (a) near the side wall $r/L = 0.45$, and (b) near the axis $r/L = 0.06$.

Figure 5.6a shows the time- and angularly-averaged heat flux as a function of Ra at different radial positions on the mid-plane. The solid lines are the measurements of Shang et al. [16] taken right on the axis and very near to the wall. Figure 5.6b

shows that the corresponding scaling exponent γ_j as a function of the radial position decreases monotonically from 0.43 near the axis to 0.29 close to the side wall. The measurements of Shang et al. [16] and the theoretical analysis of Grossmann and Lohse [11] only made statements on the values close to the side wall and to the axis; these are well confirmed by the present results. In the Ra range considered here the heat transport near the side wall is an order of magnitude larger than in the center. An extrapolation of the power law fits $\overline{j} = 0.0025 Ra^{0.43\pm0.01}$ obtained near the center and $\overline{j} = 0.3236 Ra^{0.29\pm0.01}$ valid near the wall, shows that these become equal for $Ra \approx 10^{15}$. This value is consistent with the prediction of the unifying theory [9]. Recent experiments [29] suggests the occurrence of this feature in the range $10^{13} \leq Ra \leq 5 \times 10^{14}$, whereas Shang et al. [16] suggested that it happens at $Ra \approx 10^{14}$, based on their extrapolation.

5.4 Local fluctuations

In this section, we determine the scaling with Ra of the velocity and temperature fluctuations with respect to their theoretical global mean at different radial locations.

Figure 5.7a shows $Re_{rms} \equiv \sqrt{(Ra/Pr)} u_{rms}$ (equivalent to $U_{dim} L/\nu$ with U_{dim} the dimensional rms velocity) as a function of Ra on the mid-plane. For the normalized temperature fluctuations we take the root mean square of $\theta' = \theta - 1/2$. Figure 5.7b shows the results for this quantity vs. Ra at different radial positions on the mid-plane.

At all radial positions, fluctuations of both velocity and temperature exhibit a power law dependence on Ra proportional to Ra^{γ_u} and $Ra^{\gamma_{\theta'}}$, respectively. In this Ra number regime the thermal fluctuations close to the side wall are an order of magnitude larger than at the cell center due to the plumes that travel along the wall.

Figure 5.8 shows that the corresponding velocity scaling exponents increase smoothly from $\gamma_u = 0.44$ in the cell center to $\gamma_u = 0.49$ near the side wall. Figure 5.8 shows that the corresponding temperature scaling exponent decreases from $\gamma_{\theta'} = -0.18$ in the cell center to $\gamma_{\theta'} = -0.20$ near the side wall.

Table 5.2 summarizes the data for the scaling exponents available in the literature and compares them with the present ones. There are some differences among the values reported. This is due in part to the spatial dependence of this quantity, shown in Figure 5.8, but also to the use of different experimental techniques which measure somewhat different quantities. Overall, there is a general consistency among the data shown. The origin of the residual differences cannot be ascertained on the basis of the presently available knowledge and must await further research.

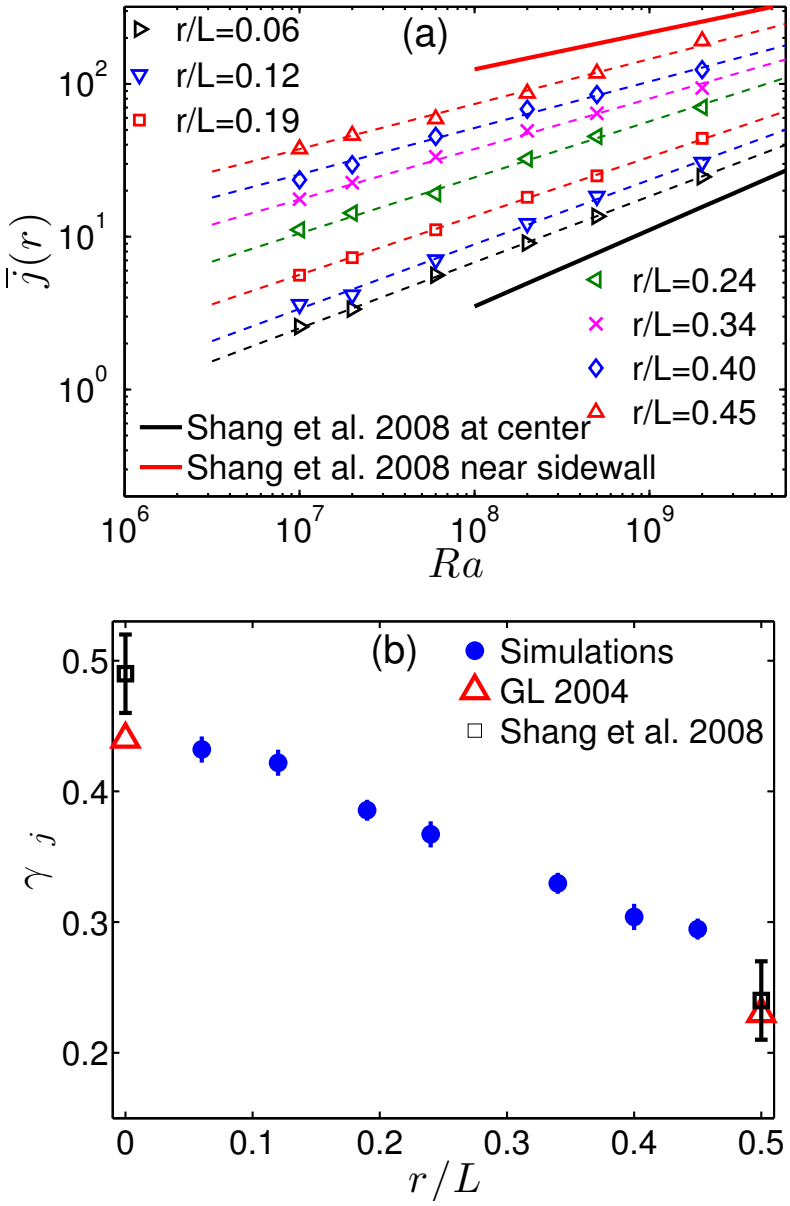

Figure 5.6: (a): Open symbols indicate the numerical results for the local heat flux averaged over time and angular position as function of Ra at different radial positions r/L. The solid lines show the experimental data of Shang et al. [16]. (b): The scaling exponent for the time- and angle-averaged heat flux as function of the radial position r/L for the simulations, experiment [16], and theory [11].

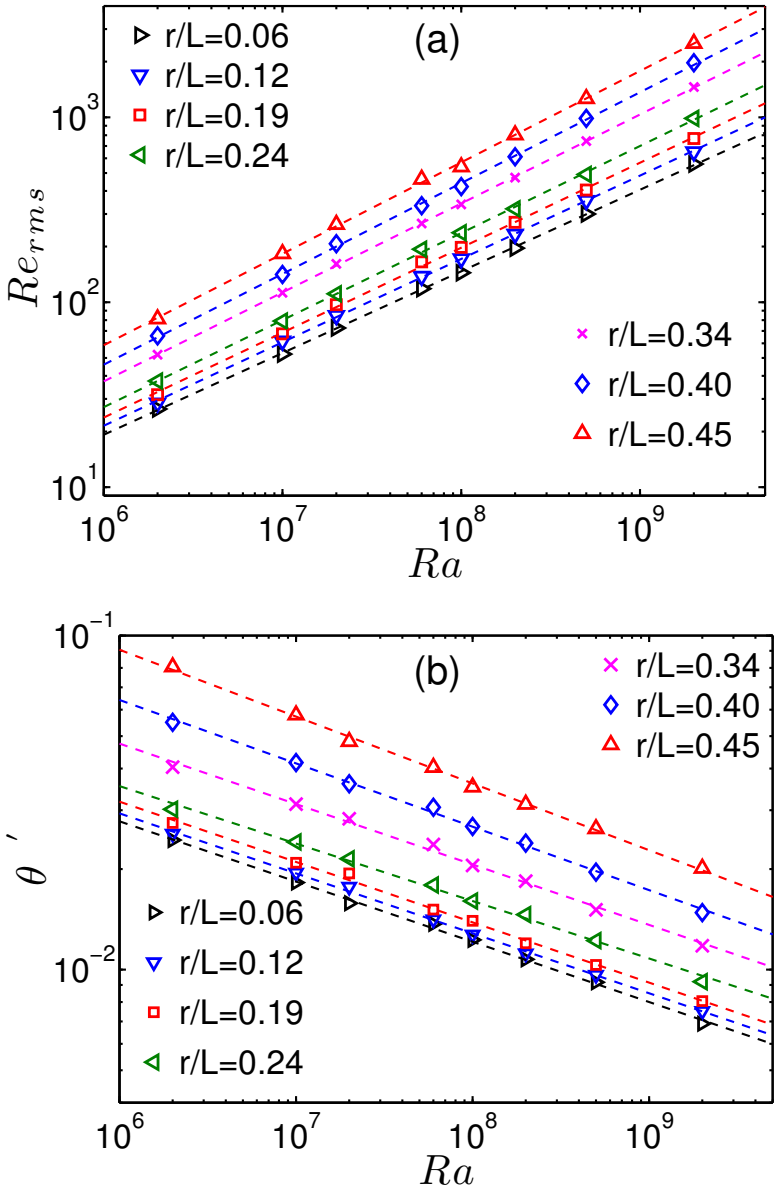

Figure 5.7: Panel (a) shows the Reynolds number based on the rms velocity Re_{rms}, and panel (b) the rms values of $\theta - 1/2$, with θ the normalized temperature, as functions of Ra, both for different radial positions.

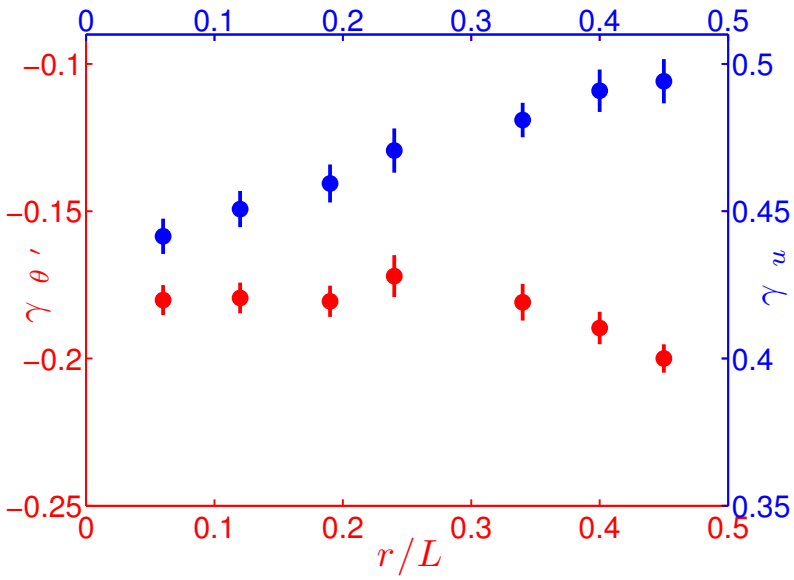

Figure 5.8: The variations in the velocity (blue) and temperature (red) scaling exponents with *Ra* are shown as functions of the radial position.

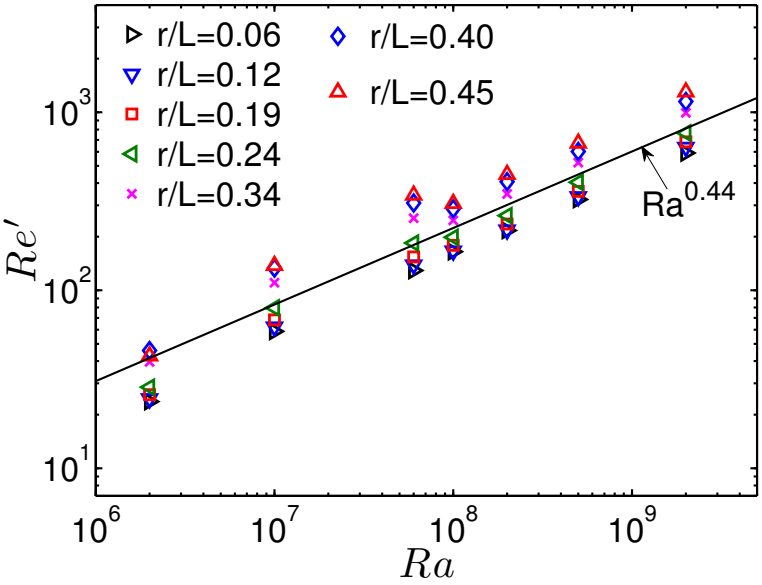

Figure 5.9: The Reynolds number Re' based on the rms velocity fluctuations vs. *Ra* at different radial positions; the solid line has the slope 0.44 suggested by value of γ_u at $r/L = 0.06$ from Figure 5.7a.

Table 5.2: Summary of the velocity and temperature scaling exponents γ_u and γ_θ reported in several experimental (E) and theoretical (T) studies. The experiments mentioned below have been carried out in cylindrical cells, unless stated otherwise.

	Ra	Pr	Γ	γ_u (center)	γ_θ (center)	γ_u (side wall)	γ_θ (side wall)
Castaing et al. [30] (E)	$4\times10^7-6\times10^{12}$	$0.65-1.5$	1	0.491 ± 0.002	-0.147 ± 0.005	–	–
Castaing et al. [30] (T)	$4\times10^7-6\times10^{12}$	$0.65-1.5$	1	$3/7$	$-1/7$	–	–
Sano et al. [31] (E)	10^8-10^{10}	$0.64-1.4$	1	–	–	0.485 ± 0.005	–
Takeshita et al. [32] (E)	10^6-10^8	0.024	1	–	–	0.46 ± 0.02	–
Ashkenazi et al. [33, 34] (E)	$10^{11}-5\times10^{14}$	$27-190$	1 (square)	–	–	0.43 ± 0.02	–
Chavanne et al. [35] (E)	$10^7-6\times10^{12}$	$0.7-4$	0.5	–	–	0.49	–
Daya and Ecke [36] (E)	$2\times10^8-4\times10^9$	5.46	0.79	0.5 ± 0.03	-0.10 ± 0.02	–	–
Niemela et al. [37] (E)	$15\times10^6-10^{13}$	0.7	1	–	–	0.5	–
Qiu et al. [38, 39] (E)	10^8-10^{10}	$5.4-5.5$	1	0.55	–	0.46	–
Lam et al. [40] (E)	10^6-10^{11}	$6-1027$	$0.5-4.4$	–	–	0.495 (bottom)	–
Grossman and Lohse [11] (T)	10^6-10^{14}	$\sim0.1-10$	1	0.39	-0.11 to -0.16	–	-0.09 to -0.11
Shang et al. [16] (E)	10^8-10^{10}	4.4	1	0.49 ± 0.03	-0.14 ± 0.03	0.46 ± 0.03	-0.24 ± 0.03
Present work	$2\times10^6-2\times10^9$	5.2	1	0.44 ± 0.01	-0.18 ± 0.01	0.49 ± 0.01	-0.20 ± 0.01

The quantity Re_{rms} shown in Figure 5.7a would equal the Reynolds number based on the mean velocity fluctuation, $Re' = \sqrt{(Ra/Pr)}u'$, with $u' = \sqrt{\overline{u_z^2} - (\overline{u_z})^2}$ only for a perfectly converged simulation without any fixed large scale convection roll, for which $\overline{u_z} = 0$. The simulation time necessary for this full convergence is completely outside the realm of practical computation as it would require averaging over a time sufficiently long with respect to slow processes such as the re-orientation of the large scale circulation [see e.g. Ref. 43, and section 5.5.1 below]. It is also interesting therefore to present in Figure 5.9 results for Re' similar to those of Figure 5.7a for Re_{rms}. The subtraction of $\overline{u_z}$ removes the effect of the slowly varying large scale circulation which dominates near the sidewall but is fairly inconsequential near the axis. Thus, the same scaling found near the axis in Figure 5.7a, $Re_{rms} \sim Ra^{0.44}$, becomes applicable over the entire cell as suggested by the solid line.

5.5 Orientation of the large scale circulation

For $\Gamma = 1$, the flow in the cell is characterized by a large scale circulation (LSC) [31, 41–43] as sketched in Figure 5.10. Most of the plumes travel in the LSC plane close to the side wall. In experiments the LSC orientation can be detected with thermistors embedded in the side wall [44] which measure relatively higher and lower temperatures in the regions of upflow and downflow [43]. Here we want to determine how the local heat flux depends on the location of measurement with respect to the LSC orientation plane.

5.5.1 Determination of LSC orientation

A well-tested method to determine the LSC orientation as a function of time is to fit a cosine to the azimuthal distribution of the vertical velocity or temperature profiles near the side walls [1, 43–45]. For this purpose we use the information from the numerical probes placed uniformly in the angular direction at $r/L = 0.45$ (see section 2) [46]. To make sure that the LSC orientation is properly identified one has to avoid a determinant influence of individual plumes. This need requires that the instantaneous data be pre-processed by means of short-time moving averages. The choice of a proper averaging time depends on an order-of-magnitude estimation of the LSC circulation time. Such an estimate can be found by dividing the length of the longest path around the cell, $2L + 2D = 4L$ for $\Gamma = 1$, by an estimate of the fluid velocity. An upper limit is the free-fall velocity, with which we find $4L/U = 4$ free-fall times. A more realistic estimate can be found by using the computed velocity which, for $Ra = 10^8$, is about $0.15\,U$ (see figure 5.11b) and somewhat smaller for $Ra = 10^9$. With

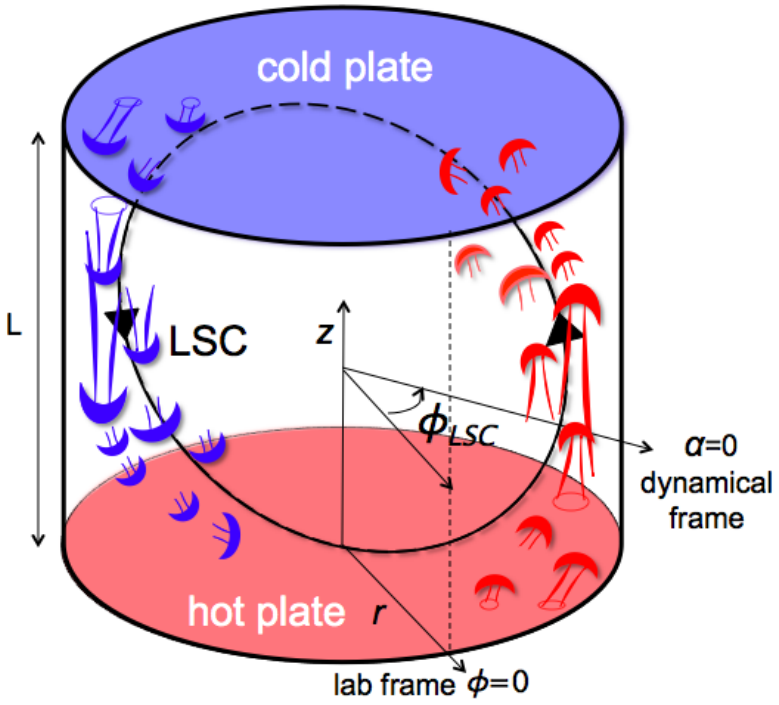

Figure 5.10: Sketch of the LSC in a cylindrical RB cell. The warm plumes go upwards on the right side, defined as $\alpha = 0$, and go downwards on the left side of the cell, defined as $\alpha = \pi$. Due to the shape of the LSC the warm uprising fluid (cold down flowing fluid) is close to the side wall at $z/L = 0.25$ and $z/L = 0.50$ ($z/L = 0.75$ and $z/L = 0.50$).

this estimate we find ≈ 27 free-fall times. On this basis we decided to use four different short-time averaging durations, namely 4, 10, 20 and 50 free-fall times. In this way we are more confident that the averaging time that we use covers the correct range.

We determine the LSC orientation by fitting the expression

$$(u_z)_i = (u_z)_m + A_u \cos(\phi_i + \phi_{LSC}), \tag{5.4}$$

to the time-averaged vertical velocity data. Here $(u_z)_i$ is the short-time moving-averaged vertical velocity provided by the i^{th} probe at the angular position ϕ_i, $(u_z)_m$ is the mean value, A_u is the amplitude and ϕ_{LSC} is the angular position of the LSC with respect to the reference frame of the computation.

Figure 5.11a shows an example of the azimuthal vertical velocity profile, and the corresponding cosine fit, using a short-time averaging window of 20 free-fall times

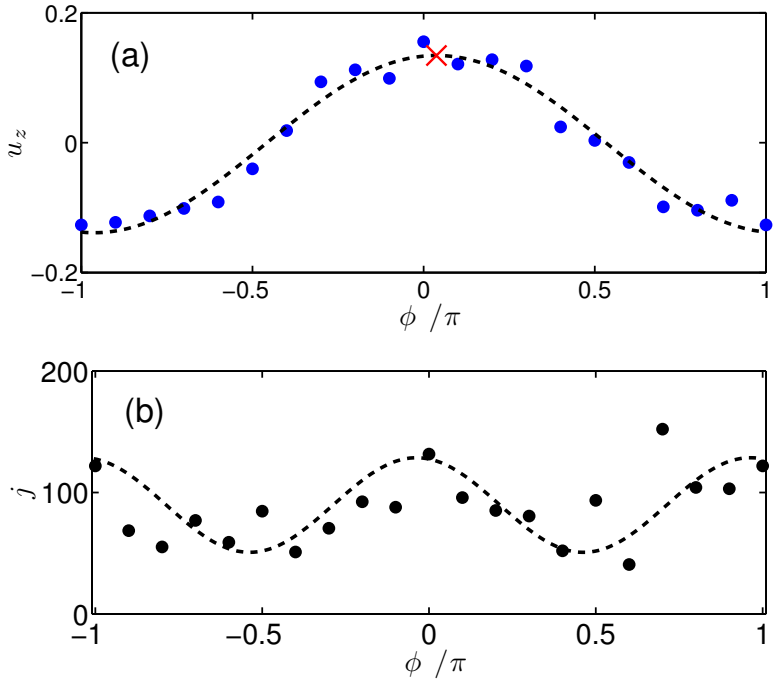

Figure 5.11: Angular dependencies of vertical velocity and heat flux on the mid-plane at $r/L = 0.45$ near the side wall for $Ra = 2 \times 10^8$: (a) vertical velocity (blue points) filtered by averaging of 20 free-fall times. The red cross indicates the maximum of the cosine fit, which we take as the LSC orientation. (b) Instantaneous local heat flux (black points). The black dash lines indicate the respective cosine fits to the data according to equations 5.4 and 5.5.

for $Ra = 2 \times 10^8$. The maximum of the curve is marked with a red cross and identifies the position of the LSC plane. Figure 5.11b is an example of instantaneous heat flux data fitted as in equation 4, but with twice the frequency (see below),

$$(j)_i = (j)_m + A_j \cos(2\phi_i + \phi_{LSC}). \tag{5.5}$$

Figure 5.12 shows ϕ_{LSC} vs. time as calculated using the four different averaging times and for four different Ra numbers. As expected, the fluctuations in the position of the LSC plane are somewhat greater when short averaging times are used. This figure clearly shows that the LSC orientation is different among simulations even though we used identical initial conditions for each simulation. We also note that the frequency of LSC reorientations observed in our simulations is roughly consistent with the experimental observations by Ref. [45]: These authors, for a somehow larger

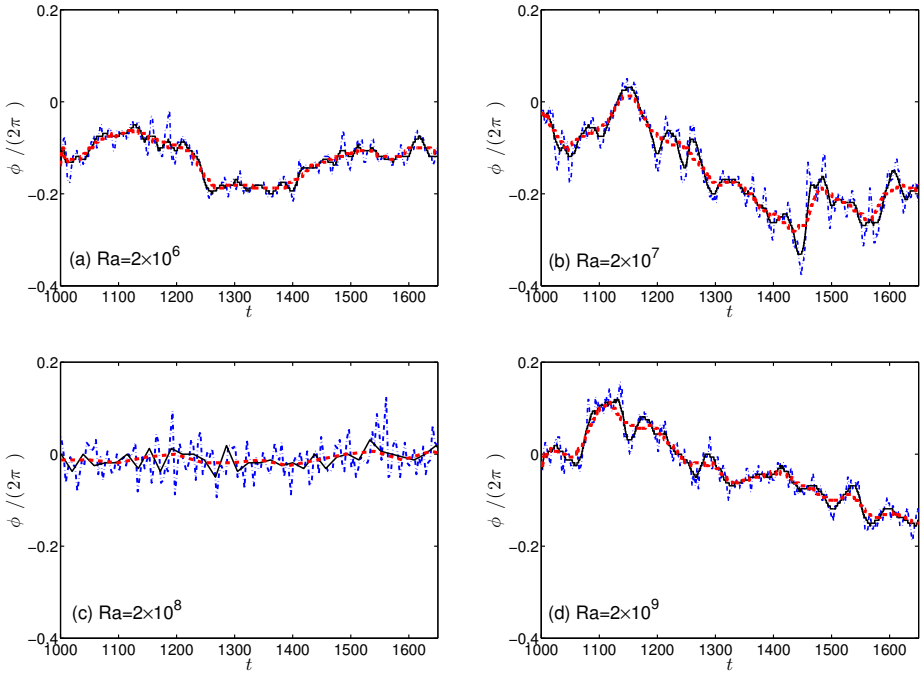

Figure 5.12: LSC orientation as function of time for different Ra. The time averaging used to determine the LSC orientation (see text) are 4, 20, and 50 free fall times. The time averaging that is applied to the signal before the analysis is 4 (blue dash-dotted line), 20 (black-solid) and 50 (red-dash) free-fall times.

$Ra = 1.1 \times 10^{10}$, find one reversal in 1200 seconds, see figure 2 of that paper. Our figure 12 shows a drift in the orientation of the LSC of up to about 1/4 over 600 free fall times, corresponding to 3000 seconds. We assume that for larger Ra as in experiment the LSC would become even more mobile.

Once the position of the LSC plane as a function of time has been determined, we can calculate the time-averaged vertical velocity $\overline{u}_z$ and heat flux $\overline{j}$ with respect to the LSC orientation. For this purpose we assign to the u_z and j instantaneously measured by the probe located at ϕ an angular position $\alpha = \phi - \phi_{LSC}$ with respect to the LSC. We repeat this step for all the probes. In this way all the data of the numerical probes are converted from the computational to the LSC frame of reference.

Time averages in the LSC reference frame for the vertical velocity and for the heat flux at $r/L = 0.45$ on the mid-plane are shown in Figure 5.13. A comparison of the two panels in this figure shows that the heat flux has double the periodicity of the velocity, because the heat flux is enhanced in correspondence of both the upward and

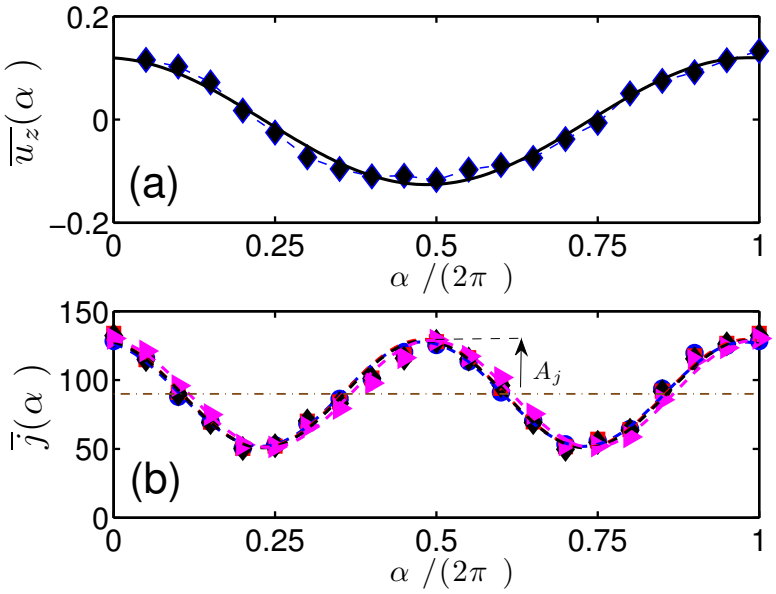

Figure 5.13: Time averaged quantities relative to the orientation of the LSC plane near the side walls (r/L = 0.45) at mid-height: (a) vertical velocity $\overline{u_z}(\alpha)$; (b) local heat flux $\overline{j}(\alpha)$. Here the circles (blue), squares (red), diamonds (black), triangles (magenta) correspond to time-averages over 4, 10, 20, and 50 free fall times, respectively. The black lines show the cosine fits according to equations 5.4 and 5.5. The mean heat flux (thin-dash dot) and the amplitude of variation (A_j) are also shown.

downward moving streams of the LSC. The local convective heat flux is lower near $\alpha = \pi/2$ and $3\pi/2$ where very few warm plumes ascend or cold plumes descend.

The four averaging times used to define ϕ_{LSC} result, in principle, in four different values of α attributed to each probe reading. Therefore, for the α dependence of, for example, the average heat flux $\overline{j}(\alpha)$, one can draw four different curves. These four results are shown together by four sets of different symbols in the lower panel of Figure 5.13 depicting the heat flux. Differences among these results are barely noticeable. This feature derives from the fact that each value of $j(\alpha)$ measured by each probe was assigned to one of 20 equal intervals in which the range of α was divided. Thus, values falling within each 5% of the circle are attributed to the same value of α. As can be seen in Figure 5.12, most of the fluctuations of the LSC angular position fall within such a range irrespective of the averaging time. Figure 5.13 would not greatly change even if the angular intervals were, for example, halved. Now the values originally in one bin would be distributed between two adjacent smaller bins.

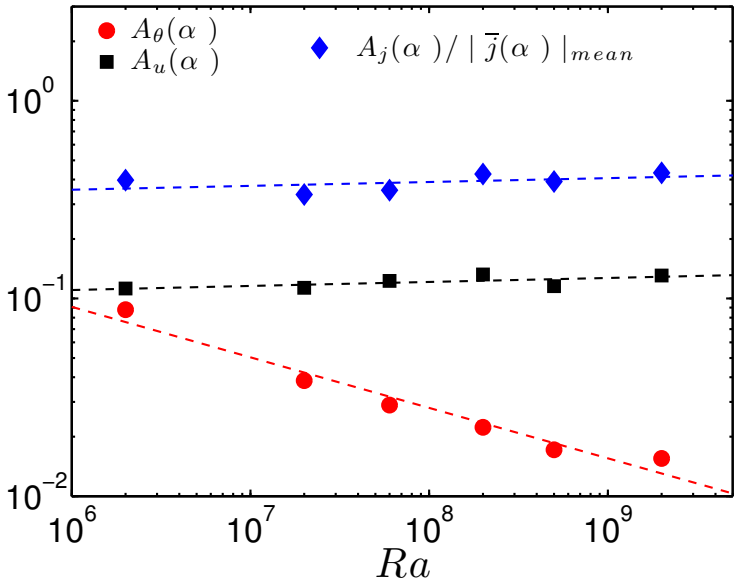

Figure 5.14: The amplitude variation as function of Ra of cosine fits near the side walls, $r/L = 0.45$, at the mid-height as function of Ra. The data are shown for temperature (circle-red), axial velocity (square-black) and normalized heat flux (diamond-blue). Here $\mid\bar{j}(\alpha)\mid_{mean}$ is the arithmetic mean heat flux in the azimuthal direction for a given Ra. The dashed lines indicates the power law fits for the data.

However, by continuity, the resulting difference would not be large. This conclusion should be corrected if large fluctuations were frequent, which is by far not the case as Figure 5.12 shows. Indeed, as seen in the figure, the short-time averages fluctuate very close to the long-time ones.

In Figure 5.14 the amplitudes of the cosine fits for the axial velocity A_u, temperature A_θ and normalized heat flux A_j (all defined by fits of Eq. 5.4 and Eq. 5.5), are shown as functions of Ra at mid-height near the side wall, $r/L = 0.45$. Interestingly, these amplitudes have a power-law dependency on Ra, with scaling exponents 0.020 ± 0.005, -0.250 ± 0.010 and 0.019 ± 0.005 for axial velocity, temperature and local heat flux, respectively.

Figure 5.15a shows the time-averaged local heat flux as a function of Ra at different α at mid-height near the side wall. From the figure it is clear that this quantity has a power law dependence on Ra. In agreement with the data in Figure 5.14, we find that the local heat flux in the LSC plane increases faster than in the regions where few warm plumes rise and cold ones fall. This is also revealed when the local heat

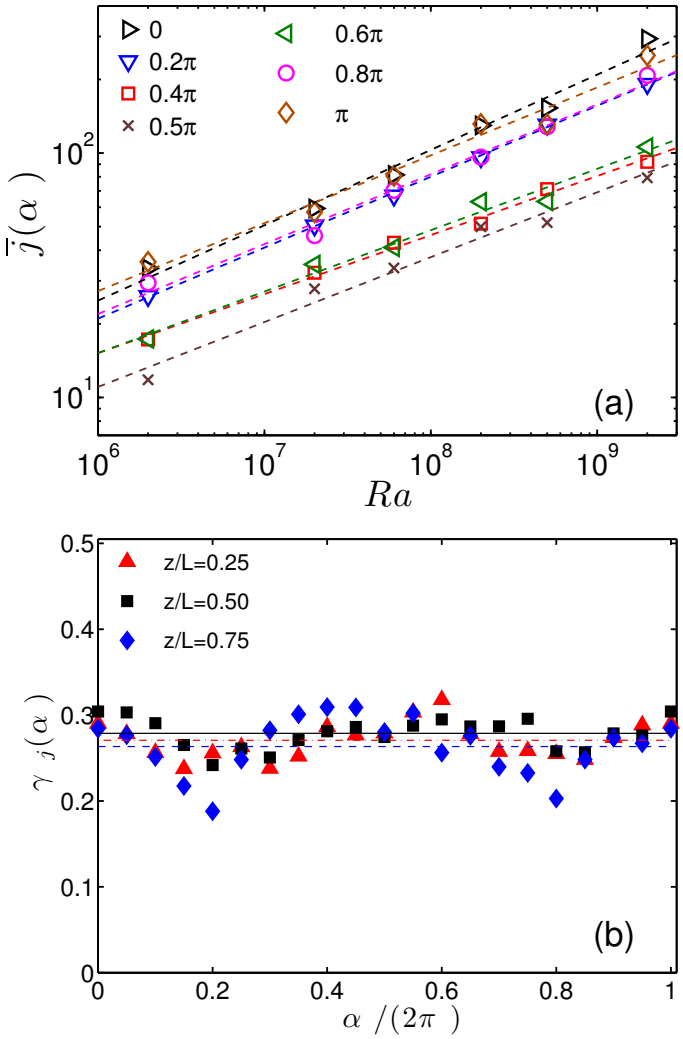

Figure 5.15: (a): Scaling of the time averaged local heat flux with Ra near the side walls, $r/L = 0.45$, at mid-height. The symbols indicate measurements taken at different α. The dashed lines are the power law fits to the data. (b) : Scaling exponent for the heat flux $\gamma_j(\alpha)$ relative to the LSC plane near the side wall at $z/L = 0.25$ (triangles-red), $z/L = 0.50$ (square-black), and $z/L = 0.75$ (diamond-blue). The straight lines indicate the arithmetic mean values of the scaling exponents.

flux scaling exponent as function of α, see Figure 5.15b, is considered.

Figure 5.16 shows the variation of the time-averaged local heat flux with α at

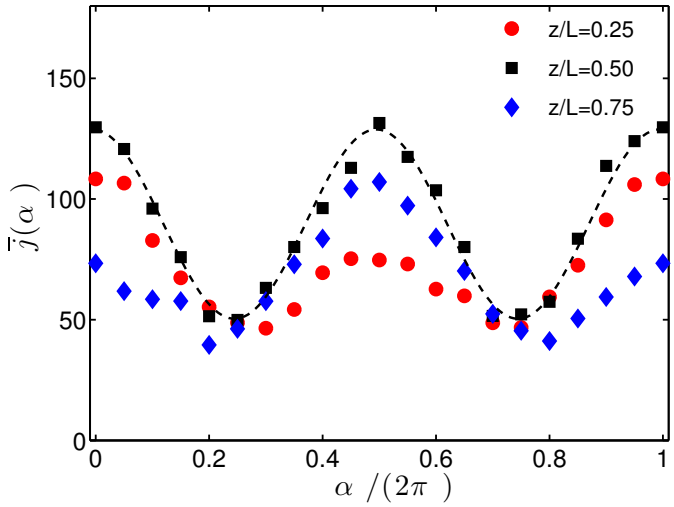

Figure 5.16: Time averaged local heat flux with respect to the LSC orientation for $Ra = 2 \times 10^8$ at different axial positions for $r/L = 0.45$. The data are at the quarter height plane $z/L = 0.25$ (circle-red), at mid-height $z/L = 0.50$ (square-black), and at the three-quarters height $z/L = 0.75$ (diamond-blue). Moving averages are taken over 20 free-fall times.

three different heights. For $z/L = 0.25$ larger values of j occur near $\alpha = 0$, and lower values near $\alpha = \pi$. A similar picture shifted by π is found for $z/L = 0.75$, with higher values near $\alpha = \pi$ and lower values near $\alpha = 0$. At $z/L = 0.50$, on the other hand, the levels at $\alpha = 0$ and $\alpha = \pi$ are comparable. These results suggest that the plane of the LSC is somewhat tilted with respect to the vertical.

5.6 Summary and Conclusions

To summarize, we investigated numerically the scaling of the local heat flux in Rayleigh-Bénard convection of a fluid with $Pr = 5.2$ (appropriate for water at 32 °C) for $2 \times 10^6 \leq Ra \leq 2 \times 10^9$ in an unit aspect ratio cylinder. In this Ra number regime the local heat flux is larger close to the side wall than on the axis. The local heat flux $u_z(T - T_0)$ is a positive quantity both when fluid warmer than the average temperature T_0 rises and fluid colder than T_0 sinks. The PDFs of the local heat flux have a positive skewness due to the dominance of plume transport in this Ra range. On the mid-plane, the scaling exponents of the local heat flux with Ra near the axis and close to the side wall agree well with the measurements of Shang et al. [16] and the predictions

of Grossmann and Lohse [11]. Here we have shown that these scaling exponents decrease monotonically with position r from 0.43 near the axis to 0.29 close to the side wall. The scaling exponent for the Reynolds number based on the rms velocity depends on the radial position as well, with a value of 0.44 near the axis and 0.49 close to the side wall. For the scaling exponents of the temperature fluctuations we find -0.18 and -0.20 respectively. We showed the marked effect of the LSC which causes local heat fluxes more than twice as large in its plane than at 90^o from it. This effect becomes stronger for high *Ra*.

References

[1] G. Ahlers, S. Grossmann, and D. Lohse, "Heat transfer and large scale dynamics in turbulent Rayleigh-Bénard convection", Rev. Mod. Phys. **81**, 503 (2009).

[2] D. Lohse and K. Q. Xia, "Small-scale properties of turbulent Rayleigh-Bénard convection", Ann. Rev. Fluid Mech. **42**, 335 (2010).

[3] E. D. Siggia, "High Rayleigh Number convection", Annu. Rev. Fluid Mech. **26**, 137 (1994).

[4] S. Grossmann and D. Lohse, *Scaling in thermal convection: A unifying view*, J. Fluid. Mech. **407**, 27 (2000).

[5] K. Q. Xia, S. Lam, and S. Q. Zhou, *Heat flux measurement in high Prandtl number turbulent Rayleigh-Bénard convection*, Phys. Rev. Lett **88**, 064501 (2002).

[6] A. Nikolaenko, E. Brown, D. Funfschilling, and G. Ahlers, *Heat transport by turbulent Rayleigh-Bénard convection in cylindrical cells with aspect ratio one and less*, J. Fluid Mech. **523**, 251 (2005).

[7] D. Funfschilling, E. Brown, A. Nikolaenko, and G. Ahlers, *Heat transport by turbulent Rayleigh-Bénard convection in cylindrical samples with aspect ratio one and larger*, J. Fluid Mech. **536**, 145 (2005).

[8] C. Sun, L. Y. Ren, H. Song, and K. Q. Xia, *Heat transport by turbulent Rayleigh-Bénard convection in 1 m diameter cylindrical cells of widely varying aspect ratio*, J. Fluid Mech. **542**, 165 (2005).

[9] S. Grossmann and D. Lohse, *Thermal convection for large Prandtl number*, Phys. Rev. Lett. **86**, 3316 (2001).

[10] S. Grossmann and D. Lohse, *Prandtl and Rayleigh number dependence of the*

Reynolds number in turbulent thermal convection, Phys. Rev. E **66**, 016305 (2002).

[11] S. Grossmann and D. Lohse, *Fluctuations in turbulent Rayleigh-Bénard convection: The role of plumes*, Phys. Fluids **16**, 4462 (2004).

[12] X. D. Shang, X. L. Qiu, P. Tong, and K. Q. Xia, *Measured local heat transport in turbulent Rayleigh-Bénard convection*, Phys. Rev. Lett. **90**, 074501 (2003).

[13] Y. Gasteuil, W. L. Shew, M. Gibert, F. Chillá, B. Castaing, and J. Pinton, *Lagrangian temperature, velocity, and local heat flux measurement in Rayleigh-Bénard convection*, Phys. Rev. Lett. **99**, 234302 (2007).

[14] J. Schumacher, *Lagrangian dispersion and heat transport in convective turbulence*, Phys. Rev. Lett. **100**, 134502 (2007).

[15] X. D. Shang, X. L. Qiu, P. Tong, and K. Q. Xia, *Measurements of the local convective heat flux in turbulent Rayleigh-Bénard convection*, Phys. Rev. E **70**, 026308 (2004).

[16] X. D. Shang, P. Tong, and K. Q. Xia, *Scaling of the local convective heat flux in turbulent Rayleigh-Bénard convection*, Phys. Rev. Lett. **100**, 244503 (2008).

[17] The diffusive heat flux $-\kappa\overline{\partial_z T(r,t)}/(\kappa\Delta/L)$ is less than 1% of the convective one, for all r and Ra, due to the tiny temperature gradient at mid height.

[18] E. S. C. Ching, H. Guo, X. D. Shang, P. Tong, and K. Q. Xia, *Extraction of plumes in turbulent thermal convection*, Phys. Rev. Lett. **93**, 124501 (2004).

[19] D. Lohse and F. Toschi, *The ultimate state of thermal convection*, Phys. Rev. Lett. **90**, 034502 (2003).

[20] R. Verzicco and R. Camussi, *Numerical experiments on strongly turbulent thermal convection in a slender cylindrical cell*, J. Fluid Mech. **477**, 19 (2003).

[21] P. Orlandi, *Fluid flow phenomena: A numerical tool kit* (Kluwer academic publishers, Dordrecht, The Netherlands, 2001).

[22] R. Verzicco and P. Orlandi, *A finite-difference scheme for three-dimensional incompressible flows in cylindrical coordinates*, J. Comp. Phys. **123**, 402 (1996).

[23] R. Verzicco and R. Camussi, *Transitional regimes of lowPrandtl number thermal convection in a cylindrical cell*, Phys. Fluids 1287 (1997).

[24] R. J. A. M. Stevens, R. Verzicco, and D. Lohse, *Radial boundary layer structure and Nusselt number in Rayleigh-Bénard convection*, J. Fluid Mech. **643**, 495 (2010).

[25] R. J. A. M. Stevens, H. J. H. Clercx, and D. Lohse, *Breakdown of the large-scale wind in aspect ratio* $\Gamma = 1/2$ *rotating Rayleigh-Bénard flow*, Submitted to Phys. Rev. E, see also arXiv:1112.0411

[26] B. I. Shraiman and E. D. Siggia, *Heat transport in high Rayleigh number convection*, Physical Review A **42-6**, 3650 (1990).

[27] F. Belin, P. Tabeling, and H. Willaime, *Exponents of the structure functions in a low temperature helium experiment*, Physica D, Nonlinear Phenomena **93(1-2)**, 5263 (1996).

[28] X. L. Qiu and K. Q. Xia, *Viscous boundary layers at the side wall of a convection cell*, Phys. Rev. E **58**, 486 (1998).

[29] X. He, Funfschilling, E. Nobach, E. Bodenschatz, and G. Ahlers, *Transition to the ultimate state of turbulent Rayleigh-Bénard convection*, Phys. Rev. Lett. **108**, 024502 (2012).

[30] B. Castaing, Gunaratne, G. Heslot, L. F. Kadanoff, A. Libchaber, A. S. Thomae, X. Z. Wu, S. Zaleski, and G. Zanetti, *Scaling of hard thermal turbulence in Rayleigh-Bénard convection*, J. Fluid Mech. **204**, 1 (1989).

[31] M. Sano, X.-Z. Wu, and A. Libchaber, *Turbulence in helium-gas free convection*, Phys. Rev. A **40**, 6421 (1989).

[32] T. Takeshita, T. Segawa, J. Glazier, and M. Sano, *Thermal turbulence in Mercury*, Phys. Rev. Lett. **76**, 1465 (1996).

[33] S. Ashkenazi and V. Steinberg, *Spectra and statistics of velocity and temperature fluctuations in turbulent convection*, Phys. Rev. Lett. **83**, 4760 (1999).

[34] S. Ashkenazi and V. Steinberg, *High Rayleigh number turbulent convection in a gas near the gas-liquid critical point*, Phys. Rev. Lett. **83**, 3641 (1999).

[35] X. Chavanne, F. Chilla, B. Chabaud, B. Castaing, and B. Hebral, *Turbulent Rayleigh-Bénard convection in gaseous and liquid He*, Phys. Fluids **13**, 1300 (2001).

[36] Z. A. Daya and R. E. Ecke, *Does turbulent convection feel the shape of the container?*, Phys. Rev. Lett. **87**, 184501 (2001).

[37] J. Niemela, L. Skrbek, K. R. Sreenivasan, and R. J. Donnelly, *The wind in confined thermal turbulence*, J. Fluid Mech. **449**, 169 (2001).

[38] X. L. Qiu and P. Tong, *Temperature oscillations in turbulent Rayleigh-Bénard convection*, Phys. Rev. E **66**, 026308 (2002).

[39] X. L. Qiu, X.-L. Shang, P. Tong, and K. Q. Xia, *Velocity oscillations in turbulent Rayleigh-Bénard convection*, Phys. Fluids **16**, 412 (2004).

[40] S. Lam, X. D. Shang, S. Q. Zhou, and K. Xia, *Prandtl-number dependence of the viscous boundary layer and the Reynolds number in Rayleigh-Bénard convection*, Phys. Rev. E **65**, 066306 (2002).

[41] R. Krishnamurti and L. Howard, *Large scale flow generation in turbulent convection*, Proc. Nat. Acad. Sci. USA **78(4)**, 1981 (1981).

[42] K. Q. Xia, C. Sun, and S. Q. Zhou, *Particle image velocimetry measurement of the velocity field in turbulent thermal convection*, Phys. Rev. E **68**, 066303 (2003).

[43] E. Brown and G. Ahlers, *The origin of oscillations of the large-scale circulation of turbulent Rayleigh-Bénard convection*, J. Fluid Mech **638**, 383 (2009).

[44] E. Brown, A. Nikolaenko, and G. Ahlers, *Reorientation of the large scale circulation in turbulent Rayleigh-Bénard convection*, Phys. Rev. Lett. **95**, 084503 (2005).

[45] E. Brown, and G. Ahlers, *Rotations and cessations of the large scale circulation in turbulent Rayleigh-Bénard convection*, J. Fluid Mech. **568**, 351 (2006).

[46] R. J. A. M. Stevens, H. J. H. Clercx, and D. Lohse, *Effect of plumes on measuring the large scale circulation in turbulent Rayleigh-Bénard convection*, Phys. Fluids **23**, 095110 (2011).

6

SUMMARY

A fundamental understanding of liquid-vapor phase transitions, mainly boiling phenomenon, is essential due to its omnipresence in science and technology. In industries, many empirical correlations exist on the heat transport to get an optimized and efficient thermal design of the boiling equipment. But nevertheless, a physical understanding of these phenomena remains inconclusive. This is because of the complexity present in the problem due to interconnections between mass, momentum and thermal energy of solid, liquid, and vapor phases. How to understand the observed heat transport and the flow dynamics based on a suitable model with the proper physics of boiling? The research presented in this work emphasizes the importance of the nucleated vapor bubbles on the local and the global properties of the flow (e.g., energy dissipation rates, rms velocity, rms temperature, heat flux etc.) in a boiling convective environment. We have studied boiling phenomenon in a Rayleigh-Bénard (RB) cell [*], with the liquid (water) mean temperature at 100 ^{o}C under normal pressures by injecting micron-sized saturated vapor bubbles on the hot plate. Vapor bubbles absorb heat from the hot plate (and also from surrounding liquid), grow in size and rise in the flow due to enhanced buoyancy. While in motion, they condense by releasing heat when they encounter a cooler liquid or by reaching the cold plate. Their complex interactions with the liquid significantly change the

[*]This system is favorable and is chosen due to existence of global energy relations between the applied heat flux, energy dissipation, and the heat transport.

mentioned local and global properties of the flow. While this study therefore does not address the real phenomenon of boiling, but it is useful to illuminate the relative importance of enhanced convection due to the increased buoyancy of vapor bubbles and their motion relative to the liquid in both the laminar and the turbulent states. In our study, the system parameters, namely the Rayleigh number (Ra)- the ratio of buoyancy force to viscous force, the Prandtl number (Pr)- the ratio of viscous diffusion to thermal diffusion, the aspect ratio (Γ)- the ratio of lateral size to height of the cell, the Jakob number (Ja)- the ratio of sensible heat to latent heat, and the number of vapor bubbles (N_b) are varied to see their effect on the flow dynamics and the heat transport.

The salient features of the numerical method of the boiling convection are as follows: Direct numerical simulations are performed on liquid water in a cylinder by solving the Navier-Stokes equations under Boussinesq approximations augmented by additional forces due to point-like two-way coupled saturated vapor bubbles. Each vapor bubble is tracked on a Lagrangian framework separately, by solving the instantaneous force balance between buoyancy, drag, inertia, lift and added mass terms. The radial dynamics (or change in size) of a saturated vapor bubble is incorporated in the simulations by considering the heat exchange with the surrounding liquid. The point-bubble model which is used here is justified because the volume fraction that they occupy is small and the bubble size is smaller than the relevant flow scales, inparticular the Kolmogorov scale.

In Chapter 2, the effect of vapor bubbles on kinetic and thermal energy dissipation rates in a $\Gamma = 1/2$ aspect ratio RB cell is reported for a relatively small Rayleigh number Ra$= 2 \times 10^5$ and for $N_b = 10000$ vapor bubbles. We observed that the vapor bubbles have a two-fold effect on the flow: on one hand, they exchange heat to the surrounding liquid, thus tending to decrease the temperature differences responsible for the convective motion but, on the other hand, the absorbed heat causes the bubbles to grow, thus increase in buoyancy and enhance the turbulence by increasing the velocity fluctuations. The enhancement in buoyancy can be seen as an increase in anisotropic vertical momentum of the flow. The competition between enhanced buoyancy and smoothened temperature differences depends on the Jakob number (Ja), and a quantification based on it has been done. For very small Ja, the bubble volume change is small and the absorption or release of heat dominate over the buoyancy effect. The outcome is a reduction of the driving force of the circulation with a corresponding attenuation of the kinetic energy dissipation. The added buoyancy however starts to become dominant at small Ja with a strong enhancement of the kinetic and thermal energy dissipations and hence the increase in the intensity of turbulence in the system. Further, the dynamics of the bubble-liquid interactions

based on the bubble probability density functions (in the bubble size vs. relative velocity plane) are discussed. As the bubble growth is restricted (by making Ja=0), the bubble velocity relative to the liquid velocity reaches the 'terminal velocity' of a single bubble rising in a quiescent liquid. As the bubble growth is allowed, the relative velocity spreads away from the terminal velocity and this indicates the importance of additional forces including buoyancy and drag.

In Chapter 3, we have demonstrated an effective way of transporting heat from a hot surface to a liquid is by the boiling process itself rather than by natural convection. Though the enhancement in the heat transport in boiling is due to several complex mechanisms, an important component is the buoyancy of the bubbles which compounds with that of the liquid to give rise to the enhanced transport. In this chapter, for the same geometry with a different aspect ratio $\Gamma = 1$, the range between Ra$= 2 \times 10^6$ and 5×10^9 is considered. The chosen conditions are such that the initial flow configuration itself is in a turbulent state and is not in a laminar state as mentioned in Chapter 2. We studied the heat transport and its dependence on the bubble number (N_b), the degree of superheat of the hot bottom surface (ξ) and the Rayleigh number (Ra) in a turbulent state. Bubbles always have a beneficial effect on the total heat transport in the system. The *relative* enhancement of the heat transport is a decreasing function of Ra due to stronger levels of turbulence. In-order to reflect a physical reality of a boiling situation, we have changed the number of bubbles from 10000 to 150000, in addition to a change in ξ from 0 to 0.5, and found an increase in heat transport. For small ξ the enhancement in heat transport is small because the bubbles mostly encounter colder liquid, condense and add very little buoyancy to the system. As ξ increases, the enhancement becomes stronger due to larger bubble growth. The number of bubbles N_b is also an important parameter in terms of creating a larger circulation and the effective removal of latent heat from the cell. The up-down symmetry of the boundary layers is broken due to bubble growth and condensation. We observe intense fluctuations in velocity and temperature in the cell. The plume detachment rate from the hot surface increases due to the strengthened circulation and hence the increase in the heat transport. The effect of vapor bubbles on the classical scaling laws of heat transport are discussed. Finally, an equation for the enhanced buoyancy is given in terms of the degree of super heat and the Rayleigh number.

In chapter 4, temperature fluctuations in a boiling turbulent convection for water boiling at 100 ^{o}C at normal pressures in a unit aspect ratio cylinder with Ra$= 2 \times 10^8$ is considered. In the simulations, we have injected bubbles in number 10000, 50000 and 150000 with a fixed surface temperature maintained at the mean fluid temperature, and found that the well known front-like structures in the flow are smoothened

by the rising vapor bubbles. We further found that the coherence between the velocity and the temperature fields were lost. To better describe this the small-scale motions and their higher-order structure functions are discussed in this chapter. At very small scales, i.e., in the dissipative range, the thermal energy content in the boiling and in classical convection are comparable. But at the large scales due to the effect of bubbles, the thermal energy is smaller in the case of boiling convection. As we move away from the small scales towards the integral (large) scales the second-order structure functions show a passive scalar (similar to like Obukhov-Corrsin scaling) behavior for the temperature field in both the boiling and classical convection. In contrast, the kinetic energy at any scale (small to large) is increased by several orders-of magnitude due to the bubble swarming in the flow. The velocity structure functions show a classical K41 behavior in this regard. From the probability density functions, we inferred that the temperature field intermittency is smaller for boiling convection than for the classical convection. Further, we systematically analyzed the higher-order structure functions of the temperature field and quantified the intermittency.

In chapter 5, the radial dependence of the velocity, temperature fluctuations and of the time-averaged heat flux in classical RB convection are investigated for Rayleigh numbers (Ra) in the range between 2×10^6 and 2×10^9 in a unit aspect ratio cylinder. In this *Ra* number range the local heat flux is larger close to the sidewall than on the axis. The local heat flux $u_z(T - T_0)$ is a positive quantity both when fluid warmer than the average temperature T_0 rises and fluid colder than T_0 sinks. The probability density functions of the local heat flux have a positive skewness due to the dominance of plume transport in this *Ra* range. On the mid-plane, the scaling exponents of the local heat flux as function of Ra near the axis and close to the side wall agree well with the experiments and the theoretical predictions. The scaling exponents decrease monotonically with position from 0.43 near the axis to 0.29 close to the side wall. The scaling exponent for the Reynolds number (as function of Ra) based on the rms velocity depends on the radial position as well, with a value of 0.44 near the axis and 0.49 close to the side wall. For the scaling exponents of the temperature fluctuations we find -0.18 and -0.20, respectively. We have further investigated the dynamics of large scale circulation (LSC) and showed its effect on the local heat flux.

To conclude, this work is a preliminary step to better understand boiling thermal convection.

SAMENVATTING

Een fundamenteel begrip van vloeistof-gas fase-overgangen, vooral de eigenschappen van kokende vloeistoffen, zijn van essentieel belang: het is alom vertegenwoordigd in de wetenschap en technologie. In de industrie bestaan er veel empirische correlaties op het gebied van warmtetransport en stromingsdynamica, die resulteren in een optimaal en efficiënt thermisch ontwerp van de apparatuur. Echter, het fysisch begrip van deze verschijnselen is onvolledig, door de interconnecties van massa, impuls en thermische energie van vaste fasen, vloeibare fasen en dampfasen. Hoe kan men de waargenomen warmtetransport en de stromingsdynamica op basis van een geschikt model met de juiste fysica begrijpen? Het onderzoek dat in dit werk gepresenteerd wordt laat het belang zien van de genucleëerde dampbellen voor zowel de lokale als de globale eigenschappen van de stroming (bijvoorbeeld energiedissipatiesnelheden, rms snelheden en rms temperaturen) in een kookconvectieve omgeving. We hebben verschijnselen van kokende vloeistoffen bestudeerd in een Rayleigh-Bénard (RB) cel, door middel van het injecteren van microscopisch kleine verzadigde dampbellen op de hete plaat, in water met een gemiddelde temperatuur van 100 ^{o}C onder standaarddruk. Dampbellen absorberen warmte van de hete plaat en van de omgevingsvloeistof, groeien, en stijgen op, samen met de stroming. Terwijl de bellen zich omhoog verplaatsen, condenseren deze als gevolg van het vrijgeven van latente warmte wanneer ze in een koelere vloeistof terechtkomen, of door het naderen van de koude plaat. De interacties van de bellen met de vloeistof verandert de lokale en globale eigenschappen van de stroming significant. Dit werk is belangrijk voor het begrijpen van het belang van toegenomen convectie, als gevolg van het verhoogde drijfvermogen van dampbellen en de beweging van de bellen ten opzichte van de vloeistof in zowel de laminaire als de turbulente toestand. De systeemparameters, te weten het Rayleigh getal (Ra), de verhouding van het drijfvermogen en de visceuze kracht, het Prandtl nummer (Pr), de significantie van de visceuze diffusie ten opzichte van thermische diffusie, de hoogte-breedteverhouding van de cilinder (Γ), de verhouding van de laterale grootte en de hoogte van de cel, het Jakob nummer (Ja), de verhouding van 'voelbare' warmte en de latente warmte, en het aantal dampbellen (N_b), worden gevarieerd om het effect op de stromingsdynamica en op het warmtetransport te onderzoeken.

Directe numerieke simulaties worden uitgevoerd op vloeistof in een cilinder door het oplossen van de Navier-Stokes vergelijkingen onder aanname van de Boussinesq benaderingen, aangevuld met additionele krachten als output van puntsgewijze feedbackgekoppelde verzadigde dampbellen. Elke dampbel wordt afzonderlijk getraceerd op een Lagrangiaans coördinatenstelsel, door middel van het oplossen van de momentane krachtbalans tussen drijfvermogen, weerstand, traagheid, opduwing (lift) en 'added mass'-invloeden. De radiële dynamiek van een verzadigde dampbel wordt geïmplementeerd in de simulaties, als functie van de latente warmteuitwisseling met de omringende vloeistof.

In hoofdstuk 2 wordt het effect van dampbellen op kinetische en thermische energiedissipatie voor een $\Gamma = 1/2$ RB cel gerapporteerd, voor $\mathrm{Ra} = 2 \times 10^5$, en voor $N_b = 10000$. Dampbellen oefenen twee effecten uit op de stroming: enerzijds wisselen zij warmte uit aan de omringende vloeistof, waardoor de temperatuurverschillen die aan de grond liggen van de convectieve beweging verkleinen; anderzijds veroorzaakt de opgenomen warmte een groei van de bellen, waardoor verhoogd drijfvermogen en toename van de turbulentie (als gevolg van het verhogen van de snelheidsfluctuaties) veroorzaakt wordt. De toename van het drijfvermogen kan worden gezien als een toename van de anisotrope verticale dynamiek van de stroming. De balans tussen het toegenomen drijfvermogen en de verkleinde temperatuurverschillen, is afhankelijk van het Jacob getal. Deze balans wordt in dit hoofdstuk gekwantificeerd. Voor zeer kleine Ja is de verandering van het belvolume klein en overheerst de absorptie van warmte het effect op drijfvermogen. Het resultaat is een reductie van de circulatie met daarmee een vermindering van de kinetische energiedissipatie. Voor grotere, maar nog steeds kleine Ja wordt het toegevoegde drijfvermogen echter dominant, wat een sterke toename betekent van de kinetische en thermische energiedissipatie, wat resulteert in toename van de turbulentie in het systeem.

In hoofdstuk 3 wordt warmtetransport in kookconvectie beschreven. Hoewel de toename in de transport van warmte in kokende vloeistof wordt veroorzaakt door verscheidene mechanismen, is het drijfvermogen van de dampbellen één van de meest belangrijke componenten. Het warmtetransport en de afhankelijkheid van het aantal bellen, de mate van oververhitting van het onderoppervlak, en het Rayleigh getal worden onderzocht. Bellen verhogen doorgaans de warmtetransport in het systeem. De relatieve toename van het warmtetransport is een afnemende functie van Ra als gevolg van een sterkere mate van turbulentie. Het aantal bellen en de mate van oververhitting zijn tevens belangrijke parameters, omdat de circulatie versterkt wordt, en er dus warmte wordt onttrokken aan het systeem.

In hoofdstuk 4 worden de intermitterende correcties in het thermisch veld voor

kookconvectie behandeld. De structuren in de stroom worden afgevlakt door de opstijgende dampbellen. Verdere beschrijving van de bewegingen op kleine schaal, in termen van hogere orde structuurfuncties, laten een aanzienlijk effect zien van thermische afvlakking als gevolg van de bellen. Op zeer kleine schaal, dat wil zeggen op dissipatieve schaal, zijn de thermische energie van het koken en de energie van de klassieke convectie van vergelijkbare significantie. Echter, op grote schaal is de thermische energie kleiner in verhouding tot de klassieke convectie, als gevolg van de bellen. Als we de inertiële schaal beschouwen, laten tweede orde structuurfuncties een passief scalarveld zien (vergelijkbaar met de Obukhov-Corrsin schaling) in zowel kookgedrag als RB convectie. De kinetische energie op elke schaal (klein tot groot) wordt vergroot, als gevolg van de beldynamica in de stroming. De snelheidstructuurfuncties vertonen een klassiek K41 gedrag. Van de kansdichtheidsfuncties leiden we af dat de onregelmatigheden in het temparatuurveld kleiner zijn voor de kookconvectie dan voor de klassieke convectie.

In hoofdstuk 5 worden ruimtelijke afhankelijkheden van de snelheid, temperatuurschommelingen en de tijdgemiddelde warmtestroom in klassieke RB convectie onderzocht voor Rayleigh getallen die binnen het bereik 2×10^6 - 2×10^9 liggen, in een $\Gamma = 1$ cilinder. Voor deze Rayleigh getallen is de lokale warmteflux groter in de buurt van de zijwand dan op de symmetrie-as. De lokale warmteflux $u_z(T - T_0)$ is een positieve grootheid, zowel voor gedeelten van de stroming waar de vloeistof verder opwarmt dan de gemiddelde temperatuur T_0, als in gedeelten van de stroming waar de vloeistof kouder wordt dan T_0. De kansdichtheidsfuncties van de lokale warmtestroom hebben een asymmetrie, als gevolg van de dominantie van het 'warmtepluim'-transport in dit Ra bereik. Op het middenvlak komen de schalingsexponenten van de lokale warmteflux bij de symmetrie-as en dichtbij de zijwand goed overeen met de experimenten en de theoretische voorspellingen. De schalingsexponenten nemen monotoon af van 0.43 bij de as, naar 0.29 in de buurt van de zijwand. De schalingsexponent voor het Reynolds-getal gebaseerd op de rms snelheid is mede afhankelijk van de radiële positie, met een waarde van 0.44 bij de as en 0.49 in de buurt van de zijwand. Voor de schalingsexponenten van de temperatuurschommelingen vinden we -0.18 en -0.20, respectievelijk. We hebben de dynamica van grootschalige circulatie (LSC) nader onderzocht, en het effect op de lokale warmteflux getoond.

Samengevat is dit werk een eerste stap richting het beter begrijpen van de kookthermische convectie in het perspectief van stromingsleer en warmte-overdracht.

Acknowledgements

First and foremost, I would like to thank my promoter and guide Prof. Detlef Lohse for giving me this wonderful opportunity to work with him. His passion for science, guidance and teachings were really great and taught me interesting lessons on both the subject and in general. I always enjoyed discussions and conversations with him. His way of writing a scientific paper is remarkable and I really appreciate the way he takes out time from his busy schedules to guide students. I want to thank him from the core of my heart for his constant support and guidance.

'Distance is immaterial when it comes to knowledge transfer'. I understood this after I met Prof. Andrea Prosperetti. My sincere gratitude to him for his generous support and valuable advice. Just as Sun's warmth can be felt irrespective of its distance, he was always available for me to help. His keen eye in striking on a problem from all directions, his careful listening, perfect explanation and logical connection on the subject has taught me a lot. I still remember the day, when he was on his way back to Schipol airport and made necessary corrections on one of our joint papers and informed me over phone. I also remember the late evenings we spent in finishing up the work on a short paper at Drinerburght hotel. His short visits to UT were always productive to me. I am really fortunate to get him as one of my supervisors.

This work was sponsored by Foundations for Fundamental Research on matter (FOM), The Netherlands in joint collaboration with Akzo Nobel, DSM, Shell and Tata steel as a research programme on Industrial partnership programme (IPP) on Fundamentals of Heterogenous Bubbly Flows (FHBF). My thanks to Albert Bokkers, Bert Vreeman, Dirk van der Plas, Maurice Veenman, Peter Veenstra, Joop Baltussen, Martin van Sint Annaland, Niels Deen and Pieter de Witte and others. The computations are carried out on Huygens, the SARA and my thanks to NWO. I would also like to thank Wim Rijks for his valuable help.

Now, I would like to thank all the other people who were significant in helping me either in academics or in personal life.

My past years in Meander were really wonderful. I was initially new to the place but with time, I started liking my office room, my work, and my late night stay backs to finish work. I actually loved my place not just because of the work, but also because of the people around me. I would like to take this chance to thank my

officemates Bram, Ceyda, and Ivo. Bram's punctuality, time management, charming smiles; Ivo's generous help, explanations on science and wonderful car trips; Ceyda's courage, everlasting enthusiasm on Physics, debates, discussions, and other useful helps makes me nostalgic. There was always some thing new to learn from these guys. Thank you very much and I will miss you guys. Also, I would like to thank other friends like Vivek, Erwin, Laura Schmidt, Laura Stricker, Sanders, Siddartha, Paolo, Richard, Tak, Julian, Ivo Roghair, Yuk Man, Yoshi, Koen, Pascal, Alex, Denis van Gills, Oscar, Kristijan, Alvaro, Sylvian, Edip, Hanneke, Stefan, Joost, Tuan, Christos, Wim, Francois, Class, Fede, and Arjan for their help, for the nice discussions and for the wonderful times spent with them. Other friends in POF are also acknowledged. A special thanks to Wilco for his writeup and for the other discussions.

I would like to thank Prof. Roberto Verzicco and Prof. Federico Toschi for their friendliness, for their help on computational methods and for their suggestions on my manuscripts. Their help was valuable and always benefitted me.

My sincere thanks to Prof. Siegfried Grossman, for his help on convection problem. It was my pleasure to read his papers on convection and turbulence and taught me a lot. Dr. Chao Sun is an experimentalist and remarkable genius with lot of enthusiasm to do science. His help and discussions always motivated me and my sincere thanks to him.

I would like to thank Dr. Devaraj van deer Meer and Dr. Jacco Snoeijer for their discussions and explanations on science, which were pleasure to listen and helped me to learn other areas of Physics. My many thanks to Prof. Leen van Wijngaarden for his help in explaining about the 'Pseudo Turbulence'. It was an awesome lecture from him and I really got benefitted by that.

My sincere thanks to Prof. Meheboob Alam (JNCASR) for his help, motivation, and for being in the part of my thesis committee. A very special thanks to Prof. Hans Kuipers (TUE), and also to Prof. Rob Hagmeijer (UT).

I would like to thank two other remarkable people whom I asked help more than any other in these four years. Mrs. Joanita Leferink, you are fantastic. Without your help, I could not have handled works like taking appointments with professors, reimbursing bills, buying flight tickets, visa issues and many other administrative tasks. My warm hugs and a big thanks to you. Computational guys (like me) also need a computer expert for help. It is Mr. Bas Benschop, POF system administrator who helped me on a countably infinite times in dealing with computer related problems. His command on computer architecture is extraordinary. His smiling face which says 'I am here you do not fear' makes any one cheerful. My sincere thanks to him and to his *magic hands*.

I would also like to thank some of my other friends Aditya, Tam Raja, Chaki, Raghav, Vishnu, Jitu, Chandra, Koti, Hrudya, Varsha, Giri, Jyothi, Kranthi, Hema, Kishore, Anoop, Gayathri, Sri Krishna, Antina, Vijay, Abhi, Beate, Priyanka, Anna, and Prof. Vinod Subramaniam in some parts or in great influenced my life and made my life happier and easier.

I would like to thank my parents, siblings, cousins, aunts, uncles and my beloved late grandma for their valuable advices and moral support.

My special gratitude to Lakshmi Sharmila, who is my soul. Without her constant support, help and understanding I might not have reached this stage. Our phone calls, messages, and adventures on Indian roads finally tied us to a strong bond which will remain forever in my life. She is always there and offered me her hand when I was in trouble. What a wonderful lady she is. Thank you ma'am for all your affection, love and friendship.

Finally, I acknowledge every one by repeating it 'Endaroo mahanubhavulu andariki vandanamulu'.

Rajaram Lakkaraju,
Enschede,
11th November 2012.

About the author

Rajaram Lakkaraju was born in Malakpet, Hyderabad, India. His primary and secondary education was mainly in and around a city named Vijayawada. He was brought up by his grand mother and his close bond with her always made him happy and joyful by listening to Indian fairy tales and mythological stories. Her upbringing was fine that there were no complaints either from school or friends. At early ages itself, he cultivated the hobby of playing chess and soon he got addicted to its beauty.

After finishing secondary education and clearing engineering entrance examinations he finally joined RVR&JC college to pursue a degree in mechanical engineering. Life was tough there, every day he had to travel long distances from his home to college and back. But his perseverance and enthusiasm never went down. After successfully graduating, he spent nearly five months in Kanpur and worked on developing a strain-gauze balance in a wind tunnel facility. He was moved by the work and power of computational techniques and this triggered his inclination for a degree in computational fluid mechanics.

Eventually, he joined JNCASR, Bangalore for doing his M.S. (Engg.) in fluid mechanics. There he got fascinated by the work on thermal convection and was motivated by the fluid dynamicists and the physicists around him. He spent long hours reading books, journals and his constant battle with mathematical equations and developing computational codes in granular lab made him workaholic and fetched him a masters degree. After that he spent twelve or more months working on cloud convection in Bangalore and his passion on the subject increased many folds. He started looking around the world for elite experts on convection from whom he could learn more. Soon, he came across Prof. Detlef Lohse in The Netherlands as the right person and the authority on convection and joined him for a Ph.D degree.

The Netherlands was a completely new world to him, everything around him seemed different. It took quite some time for him to learn and get acclimatized to the new place. During the course of time, he was introduced to another excellent teacher Prof. Andrea Prosperetti. His association with these two great men made him strong on the subject with an everlasting impression on life.